



UNIVERSITÀ
DEGLI STUDI
DI PADOVA

Sede Amministrativa: Università degli Studi di Padova

Dipartimento di Ingegneria dell'Informazione

CORSO DI DOTTORATO DI RICERCA IN: Ingegneria dell'Informazione

CURRICOLO: Scienza e Tecnologia dell'Informazione

CICLO: XXXIV

Extreme-Ultraviolet Instrumentation for Polarimetry and Spectroscopy

Coordinatore: Ch.mo Prof. Andrea Neviani

Supervisore: Dr. Luca Poletto

Co-Supervisore: Dr. Fabio Frassetto

Dottorando: Fabio Samparisi

UNIVERSITY OF PADOVA

PH.D. SCHOOL IN INFORMATION ENGINEERING
XXXIV CLASS

DOCTORAL THESIS

**Extreme-Ultraviolet Instrumentation
for Polarimetry and Spectroscopy**

Author:
Fabio Samparisi

Supervisor:
Dr. Luca Poletto

Co-supervisor:
Dr. Fabio Frassetto

Ph.D. School Director:
Prof. Andrea Neviani

*A thesis submitted in fulfillment of the requirements
for the degree in Doctor of Philosophy*

in the

DEPARTMENT OF INFORMATION ENGINEERING

SEPTEMBER 2021

Abstract

With the increasing availability and performance of laser-driven high harmonic sources operating in the extreme ultraviolet (XUV) spectral range, there is an ever-increasing demand of optical technologies suitable for the photon handling and conditioning of this radiation sources. For this reason, this thesis describes the activities carried out for the design, realization, and characterization of different optical instruments for the conditioning of XUV and soft x-ray sources.

Polarized radiation in the XUV spectral range is a powerful tool for many experiments and investigations of light-matter interaction. Therefore, it is of great importance to analyze the polarization of light before and after interaction with the sample under investigation. The ellipticity of visible and near ultraviolet radiation can easily be determined with transmission polarizers and phase shifters, for example $\lambda/4$ plates. In the extreme ultraviolet spectral region a lack of transmitting materials complicates this task. In order to produce polarized light or to analyze the polarization of light in this spectral region a different approach based on changes in the amplitudes and phases of light upon reflection must be used. The first contribution reports the activity carried out for the design and the development of a reflection polarimeter, using gold and ruthenium optics. An extensive and systematic set of measurements of the Stokes parameters has been performed on a synchrotron beamline, with a wide range of photon energies. The results indicate the capability of the proposed reflection polarimeter to effectively analyze the polarization state of the incoming radiation and to enable ellipsometric measurements on thin films.

The second contribution consists of the design and the development of a low-cost deformable grating system to be installed as part of a monochromator for the spectral selection of ultrafast XUV pulses in a High-Harmonic Generation (HHG) beamline. We demonstrate the effectiveness and the good performance of the system, while keeping it a cheap solution for many laboratories on tight budgets. The third activity regards the upgrade of a time-delay compensated monochromator installed in a HHG beamline in Milan. The instrument has been characterized in terms of its efficiency (throughput) and its temporal performance, demonstrating the ability to handle ultrashort (femtosecond regime) XUV pulses with a good photon flux for subsequent experiments.

Sommario

La disponibilità sempre maggiore di sorgenti ottiche nel range spettrale dell' estremo ultravioletto (XUV) e dei raggi X soffici richiede lo sviluppo di tecnologie e strumentazione ottica per il condizionamento di questo tipo di radiazione. Questa tesi tratta dello studio, la realizzazione, e la caratterizzazione di diversi strumenti ottici per la manipolazione della radiazione XUV e dei raggi X soffici.

La radiazione polarizzata nell'estremo ultravioletto costituisce uno strumento eccezionale per una grande varietà di esperimenti, per questo motivo è di fondamentale importanza essere in grado di analizzare lo stato di polarizzazione della luce prima e dopo l'interazione con il campione in analisi. L'analisi della polarizzazione nel range del visibile e dell'UV vicino è facilmente realizzabile con polarizzatori in trasmissione come, ad esempio, le lamine a $\lambda/4$. Nell'estremo ultravioletto l'assenza di materiali trasmissivi complica questo processo. Per manipolare e misurare la polarizzazione della luce in questo range spettrale, è richiesto un approccio diverso, basato sul cambio di ampiezza e fase della luce a seguito di una riflessione. La prima attività di questa tesi tratta dello sviluppo e la realizzazione di un polarimetro a riflessione con ottiche di oro e rutenio. Una serie di esperimenti con radiazione di sincrotrone ha permesso una sistematica analisi dei parametri di Stokes della radiazione, in un ampio range di energie. I risultati ottenuti dimostrano che il polarimetro sviluppato costituisce un ottimo strumento per l'analisi dello stato di polarizzazione della luce e permette, inoltre, di eseguire misure ellissometriche su film sottili.

La seconda attività consiste nello sviluppo e la realizzazione di un sistema a basso costo per reticoli di diffrazione deformabili, pensato per essere installato in un monocromatore per la selezione spettrale di impulsi XUV ultrabrevi all'interno di una linea di luce per la generazione di armoniche superiori (HHG). Una serie di misure ci ha permesso di concludere che il sistema proposto è una soluzione valida ed efficace, oltre che a basso costo, risultando molto vantaggioso soprattutto per laboratori con budget limitati.

La terza attività riguarda l'aggiornamento e il potenziamento di un monocromatore compensato nel tempo installato in una linea di luce HHG a Milano. Lo strumento è stato caratterizzato dal punto di vista dell'efficienza e della risposta temporale, dimostrando che il sistema è adatto per il condizionamento di impulsi XUV ultrabrevi (nel range dei femtosecondi), presentando inoltre un buon flusso di fotoni per esperimenti a valle del sistema.

Acknowledgements

Over the course of my research activity and throughout the writing of this dissertation I have received a great deal of support and assistance.

First and foremost I am extremely grateful to my supervisor, Dr. Luca Poletto, for the continuous support and patience during my PhD study. Your expertise was invaluable in formulating the right research questions and your insightful feedback pushed me to sharpen my thinking and brought my work to a higher level.

I would like to acknowledge my colleagues Fabio Frassetto and Paola Zuppella for their wonderful collaboration and for their valuable guidance throughout my research activity. You provided me with the tools and the advice that I needed to shape my experimental methods and successfully complete my studies. Thanks to all the people I have met at CNR-IFN, especially Nicola Fabris, Fabio Melison, Lorenzo Cocola and Stefano Bonora, for all the suggestions and the valuable discussions we had in these years.

I would also like to thank the people working with me on the CiPo beamline at Elettra Synchrotron Trieste, Fabio Zuccaro, Stefano Turchini and Nicola Zema, for their insightful comments and suggestions and for their assistance at every stage of the polarimetry research project.

I would like to extend my thanks to Fabio Medeghini and Matteo Lucchini, who worked together with me in Milan, and whose collaboration and consistent support throughout the upgrade of the monochromator was priceless.

Finally, I would like to express my gratitude to my parents and my friends, Arianna, Ambra, Dario, Rachele, Francesca, and Giovanni. Without your unconditional support and encouragement in the past few years, it would have been impossible for me to complete my study.

Contents

Abstract	iii
Acknowledgements	vii
1 Introduction	1
1.1 Topics covered in this thesis	1
2 Basic properties of the electromagnetic field	3
2.1 Maxwell's equations	4
2.2 Material equations	5
2.3 The wave equation	6
2.4 Scalar waves	7
2.4.1 Plane waves	7
2.5 Vector waves	8
2.5.1 The general electromagnetic plane wave	8
2.5.2 The harmonic electromagnetic plane wave	9
2.6 Stokes parameters	14
2.7 Alternative explanation	16
2.8 Mueller calculus	18
3 Polarimetry	21
3.1 Polarization in the visible spectral range	21
3.1.1 Double refraction	22
3.1.2 Polarizers and analyzers	24
3.1.3 The Quarter-Wave Plate	25
3.2 Polarimetry in the XUV spectral range	26
3.2.1 XUV refractive index	27
3.2.2 Absorption, Reflection, and Refraction of XUV Radiation	27
3.2.3 Grazing Incidence Optics	32
3.3 Reflection polarimeter	34
3.3.1 Mirrors	35
3.3.2 First polarimeter design	37
3.3.3 Rotation stage	38
3.3.4 Photodiode	40
3.3.5 Reference signal	41
3.3.6 Control software	42
3.3.7 New polarimeter design	43
3.4 CiPo beamline	45
3.4.1 CiPo source optimization	48

3.5	Fitting Stokes parameters	49
3.6	Results	55
3.6.1	Polarimetric measurements of gold	55
3.6.2	Polarimetric measurements of ruthenium	65
3.6.3	Polarimetric measurements of thin films	72
3.7	Conclusions	78
4	Design and development of a deformable diffraction grating	81
4.1	Introduction	81
4.2	Experimental setup	82
4.3	Diffraction efficiency of replica gratings	83
4.4	FEA of the bending process	85
4.5	Manual bending tests	86
4.6	Focusing properties with zero-order light	87
4.7	Focusing properties in the XUV	88
4.8	AFM analysis	93
4.9	Aberration analysis with wavefront sensor	95
4.9.1	Wavefront measurement	96
4.9.2	Experimental setup	97
4.9.3	Results	98
4.10	Conclusions	100
5	Upgrade of a time-delay compensated monochromator	103
5.1	High-harmonic generation in gases	104
5.2	Femtosecond XUV beamline	105
5.3	Upgrade of the monochromator	107
5.4	Control software	109
5.5	Efficiency characterization	110
5.6	Temporal characterization	116
5.7	Conclusions	118
6	Conclusions	121
7	Publications	125
	Appendix	127
	Bibliography	129

Chapter 1

Introduction

1.1 Topics covered in this thesis

In this thesis a description of the activities related to the development, test, and characterization of instrumentation dedicated to the photon handling of extreme ultraviolet and soft X-ray radiation is presented. Specifically, I have been involved in three different projects:

1. Design and development of a reflection polarimeter for the extreme ultraviolet (XUV) and soft X-ray spectral range;
2. Design and development of a low-cost deformable grating system for the spectral selection of ultrashort XUV pulses;
3. Upgrade of a time-delay compensated monochromator installed on an existing beamline in Milan.

In Chapter 2 some background concepts are treated, namely the Maxwell equations, electromagnetic waves, the polarization of plane waves, and the mathematical tools used to describe the polarization state of light and the effects of various optical devices. These are considered basic concepts in the field of classical electromagnetic theory and constitute essential knowledge to fully understand the topics covered in this thesis, especially in the chapter about polarimetry.

Chapter 3 describes the activity carried out in the field of XUV polarimetry, from the mechanical and optical design of a reflection polarimeter, to the test and characterization process performed at Elettra Synchrotron Trieste. Generally speaking, polarimetry is the study of the polarization state of electromagnetic radiation. Knowing and controlling the polarization state of a XUV source is of fundamental importance in many fields, such as ellipsometry, ultrafast electron dynamics, time-resolved tomography of atomic or molecular wavefunctions, ultrafast circular dichroism of molecules and magnetic materials, non-collinear high harmonic generation, as well as astronomical science, weather science, and remote sensing. Correspondingly, there has been an increasing demand for systems to measure and control polarization in the extreme ultraviolet and soft X-ray spectral regions.

In Chapter 4 the activity concerning the design and development of a deformable diffraction grating is described. The proposed system has been designed

to be used in a High-Harmonic (HH) beamline, in order to select a specific wavelength in the XUV spectral region, and, at the same time, to focus the radiation on the desired image point, usually where the sample has been placed. The system employs a replica diffraction grating, which can be purchased for a significantly lower price with respect to master (ruled) gratings. This is especially useful for many laboratories working on a tight budget, which could benefit from the remarkable performance of the proposed system.

Chapter 5 describes the project carried out at the Polytechnic University of Milan involving the upgrade of a time-delay compensated monochromator employed in a High-order Harmonic Generation (HHG) beamline. The aim of the laboratory in Milan is the experimental investigation, with femtosecond temporal resolution, of ultrafast processes in atoms and molecules excited by pulses in extreme ultraviolet spectral range generated through the HHG process. A single harmonic is selected with a monochromator compensated in time (that allows for preserving the temporal duration of the given harmonic) characterized by a high photon flux and good spectral tunability. Such pulses are used to study ultrafast processes in atoms and molecules with pump-probe techniques. The upgrade process is described, together with the subsequent characterization of the instrument, both in terms of efficiency (throughput) and temporal performance.

Chapter 2

Basic properties of the electromagnetic field

In this chapter I will introduce some basic concepts about the classical electromagnetic theory, electromagnetic waves and their polarization, which is considered essential knowledge to fully understand the topics covered in this thesis, especially in the chapter about polarimetry.

Scientific understanding of the electromagnetic phenomena grew throughout the eighteenth and nineteenth centuries through the work of researchers such as Coulomb, Ampère, Faraday and Maxwell. Originally, electricity and magnetism were considered to be two separate forces. This view changed with the publication of James Clerk Maxwell's *A Treatise on Electricity and Magnetism* (1873) in which it was shown that electricity and magnetism were related, and their theories were unified: wherever charges are in motion electric current results, and magnetism is due to electric current. The source for electric field is electric charge, whereas that for magnetic field is electric current (charges in motion). This unification is one of the key accomplishments of 19th-century mathematical physics. It has had far-reaching consequences, one of which was the understanding of the nature of light.

In classical electromagnetism, the behavior of the electromagnetic field is described by a set of equations known as Maxwell's equations. These equations are a set of coupled partial differential equations that, together with the Lorentz force law, form the foundation of classical electromagnetism, classical optics, and electric circuits. They describe how electric and magnetic fields are generated by charges, currents, and changes of the fields. An important consequence of Maxwell's equations is that they demonstrate how fluctuating electric and magnetic fields propagate at a constant speed (the speed of light) in vacuum. Known as electromagnetic radiation, these waves may occur at various wavelengths to produce a spectrum of light from radio waves to gamma rays.

In the following section we are going to introduce the Maxwell's equations in the so-called *microscopic* version (or vacuum version), in which the electric and the magnetic fields are expressed in terms of the (possibly atomic-level) charges and currents present. This is sometimes called the *general* form, although an equally general version of the Maxwell's equations exist, the *macroscopic* formulation, which employs integral equations. The equivalence of the differential and integral formulations are a consequence of the Gauss divergence theorem and the Kelvin-

Stokes theorem [1].

2.1 Maxwell's equations

The state of excitation which is established in space by the presence of accelerating electric charges is said to constitute an *electromagnetic field*. It is represented by two vectors, \mathbf{E} and \mathbf{B} , called the *electric vector* and the *magnetic induction*, respectively.

To describe the effect of the field on material objects, it is necessary to introduce a second set of vectors: the *electric current density* \mathbf{J} , the *electric displacement* \mathbf{D} , and the *magnetic vector* \mathbf{H} .

The space and time derivatives of the five vectors are related by *Maxwell's equations*, which hold at every point in whose neighborhood the physical properties of the medium are continuous [2]:

$$\nabla \times \mathbf{E} + \frac{\partial \mathbf{B}}{\partial t} = 0 \quad (2.1)$$

$$\nabla \times \mathbf{H} - \frac{\partial \mathbf{D}}{\partial t} = \mathbf{J} \quad (2.2)$$

They are supplemented by two scalar relations:

$$\nabla \cdot \mathbf{D} = \rho \quad (2.3)$$

$$\nabla \cdot \mathbf{B} = 0 \quad (2.4)$$

Eq. (2.3) may be regarded as a defining equation for the electric charge density ρ and (2.4) may be said to imply that no free magnetic poles exist.

By applying the divergence operator to (2.2) it follows that

$$\nabla \cdot \mathbf{J} + \frac{\partial \rho}{\partial t} = 0 \quad (2.5)$$

Equation (2.5) is called the *equation of continuity*. It expresses the fact that the charge is conserved in the neighborhood of any point. If one integrates (2.5) over any region of space, one obtains, with the help of Gauss' theorem,

$$\frac{d}{dt} \int \rho \, dV + \int \mathbf{J} \cdot \mathbf{n} \, dS = 0, \quad (2.6)$$

the second integral being taken over the surface bounding the region and the first throughout the volume, \mathbf{n} denoting the unit outward normal. This equation implies that the total charge

$$q = \int \rho \, dV \quad (2.7)$$

contained within the domain can only increase on account of the flow of electric current

$$J = \int \mathbf{J} \cdot \mathbf{n} \, dS. \quad (2.8)$$

If all the field quantities are independent of time, and if, moreover, there are no currents ($\mathbf{J} = 0$), the field is said to be *static*. If all the field quantities are time independent, but currents are present ($\mathbf{J} \neq 0$), one speaks of a *stationary field*.

2.2 Material equations

The Maxwell equations (2.1) - (2.4) connect the five basic quantities \mathbf{E} , \mathbf{H} , \mathbf{D} , \mathbf{B} and \mathbf{J} . To allow a unique determination of the field vectors from a given distribution of currents and charges, these equations must be supplemented by relations which describe the behaviour of substances under the influence of the field. These relations are known as *material equations*, or *constitutive relations* [3]. If the field is time-harmonic and if the bodies are at rest, or in very slow motion relative to each other, and if the material is *isotropic* (its physical properties at each point are independent of direction), they take the relative simple form

$$\mathbf{J} = \sigma \mathbf{E}, \quad (2.9)$$

$$\mathbf{D} = \varepsilon \mathbf{E}, \quad (2.10)$$

$$\mathbf{B} = \mu \mathbf{H}. \quad (2.11)$$

Here σ is called the *specific conductivity*, ε is known as the *dielectric constant* (or *permittivity*) and μ is called the *magnetic permeability*. Eq. (2.9) is the differential form of Ohm's law. Substances for which $\sigma \neq 0$ are called *conductors*. Substances for which σ is negligibly small are called *insulators* or *dielectrics*. Their electric and magnetic properties are then completely determined by ε and μ . For most substances the magnetic permeability μ is practically unity. If this is not the case we say that the substance is *magnetic*. In particular, if $\mu > 1$, the substance is said to be *paramagnetic* (e.g. platinum, oxygen, nitrogen dioxide), while if $\mu < 1$ it is said to be *diamagnetic* (e.g. bismuth, copper, hydrogen, water).

There are cases in which the behaviour of the material cannot be described in such a simple way. For example, in so-called *ferromagnetic* materials (substances which are highly magnetic, e.g. iron, cobalt and nickel) the value of the magnetic induction \mathbf{B} is determined by the past history of the field \mathbf{H} rather than by its instantaneous value. The substance is then said to exhibit *hysteresis*.

In general, \mathbf{H} and \mathbf{B} differ in how they account for magnetization. In vacuum the two fields are related through the vacuum permeability, $\mathbf{B} = \mu_0 \mathbf{H}$, but in a magnetized material, the terms differ by the material's magnetization at each point. Magnetization is the vector field (\mathbf{M}) that expresses the density of permanent or induced magnetic dipole moments in a magnetic material. The origin of the magnetic moments responsible for magnetization can be either microscopic electric currents resulting from the motion of electrons in atoms, or the spin of the electrons or the nuclei. Net magnetization results from the response of a material to an external magnetic field. Eq. (2.11) can be rewritten as:

$$\mathbf{B} = \mu_0 (\mathbf{H} + \mathbf{M}) . \quad (2.12)$$

Something similar happens in electrostatics, where we introduce the *electric polarization*, which is the measure of the response of a material to an electric field. More specifically, the electric polarization is the vector field (\mathbf{P}) that expresses the density of permanent or induced electric dipole moments in a dielectric material. The constitutive relation for the electric field becomes

$$\mathbf{D} = \varepsilon_0 \mathbf{E} + \mathbf{P} . \quad (2.13)$$

2.3 The wave equation

Maxwell's equations relate the field vectors by means of simultaneous differential equations. On elimination we obtain differential equations which each of the vectors must separately satisfy. We shall confine our attention to that part of the field which contains no charges or currents, i.e. where $\mathbf{J} = 0$ and $\rho = 0$.

We substitute for \mathbf{B} from the material equation (2.11) into the first Maxwell equation (2.1), divide both sides by μ and apply the curl operator. This gives

$$\frac{1}{\mu} (\nabla \times \nabla \times \mathbf{E}) + \nabla \times \frac{\partial \mathbf{H}}{\partial t} = 0 \quad (2.14)$$

Next we differentiate the second Maxwell equation (2.2) with respect to time, use the material equation (2.10) for \mathbf{D} , and eliminate $\nabla \times (\partial \mathbf{H} / \partial t)$ between the resulting equation and (2.14); this gives

$$\frac{1}{\mu} (\nabla \times \nabla \times \mathbf{E}) + \varepsilon \frac{\partial^2 \mathbf{E}}{\partial t^2} = 0 \quad (2.15)$$

If we use the identity $\nabla \times \nabla \times \mathbf{V} = \nabla (\nabla \cdot \mathbf{V}) - \nabla^2 \mathbf{V}$, where \mathbf{V} is any vector function of space, (2.15) becomes

$$\frac{1}{\mu} \nabla (\nabla \cdot \mathbf{E}) - \frac{1}{\mu} \nabla^2 \mathbf{E} + \varepsilon \frac{\partial^2 \mathbf{E}}{\partial t^2} = 0 \quad (2.16)$$

We can substitute for \mathbf{D} from the material equation (2.10) into the scalar Maxwell equation (2.3) and since there are no charges we have

$$\nabla \cdot \mathbf{E} = 0 \quad (2.17)$$

Eq. (2.16) reduces to

$$\nabla^2 \mathbf{E} - \mu \varepsilon \frac{\partial^2 \mathbf{E}}{\partial t^2} = 0 \quad (2.18)$$

In a similar way we obtain an equation for \mathbf{H} alone:

$$\nabla^2 \mathbf{H} - \mu \varepsilon \frac{\partial^2 \mathbf{H}}{\partial t^2} = 0 \quad (2.19)$$

Equations (2.18) and (2.19) are standard equations of wave motion and suggest the existence of electromagnetic waves propagated with a velocity

$$v = 1/\sqrt{\mu \varepsilon} \quad (2.20)$$

In vacuum we have $\mu = \mu_0$ and $\varepsilon = \varepsilon_0$ thus the velocity at which a wave is travelling is exactly the speed of light, c :

$$c = 1/\sqrt{\mu_0 \varepsilon_0} \quad (2.21)$$

In general, the permittivity and the permeability can be written as the product of two terms:

$$\mu = \mu_0 \mu_r, \quad \varepsilon = \varepsilon_0 \varepsilon_r \quad (2.22)$$

where μ_r and ε_r are the material's relative permeability and relative permittivity, respectively. Thus, the speed of electromagnetic waves inside a material can be written as:

$$v = \frac{1}{\sqrt{\mu\varepsilon}} = \frac{1}{\sqrt{\mu_0\varepsilon_0}} \frac{1}{\sqrt{\mu_r\varepsilon_r}} = \frac{c}{\sqrt{\mu_r\varepsilon_r}} = \frac{c}{n} \quad (2.23)$$

where n is the refractive index of the material.

2.4 Scalar waves

In a homogeneous medium in regions free of currents and charges, each rectangular component $V(\mathbf{r}, t)$ of the field vectors satisfies, according to (2.18) and (2.19), the homogeneous wave equation [4]

$$\nabla^2 V - \frac{1}{v^2} \frac{\partial^2 V}{\partial t^2} = 0 \quad (2.24)$$

Some simple solutions of this equation are now going to be examined.

2.4.1 Plane waves

Let $\mathbf{r}(x, y, z)$ be a position vector of a point P in space and $\mathbf{s}(s_x, s_y, s_z)$ a unit vector in a fixed direction. Any solution of (2.24) of the form

$$V = V(\mathbf{r} \cdot \mathbf{s}, t) \quad (2.25)$$

is said to represent a *plane wave*, since at each instant of time V is constant over each of the planes

$$\mathbf{r} \cdot \mathbf{s} = \text{constant}$$

which are perpendicular to the unit vector \mathbf{s} .

It will be convenient to choose a new set of Cartesian axes $O\xi, O\eta, O\zeta$ with $O\zeta$ in the direction of \mathbf{s} . Then

$$\mathbf{r} \cdot \mathbf{s} = \zeta \quad (2.26)$$

and one has

$$\frac{\partial}{\partial x} = s_x \frac{\partial}{\partial \zeta}, \quad \frac{\partial}{\partial y} = s_y \frac{\partial}{\partial \zeta}, \quad \frac{\partial}{\partial z} = s_z \frac{\partial}{\partial \zeta}.$$

From these relations one easily finds that

$$\nabla^2 V = \frac{\partial^2 V}{\partial \zeta^2}, \quad (2.27)$$

so that (2.24) becomes

$$\frac{\partial^2 V}{\partial \zeta^2} - \frac{1}{v^2} \frac{\partial^2 V}{\partial t^2} = 0. \quad (2.28)$$

If we set

$$\zeta - vt = p, \quad \zeta + vt = q, \quad (2.29)$$

(2.28) takes the form

$$\frac{\partial^2 V}{\partial p \partial q} = 0. \quad (2.30)$$

The general solution of this equation is

$$\begin{aligned} V &= V_1(p) + V_2(q) \\ &= V_1(\mathbf{r} \cdot \mathbf{s} - vt) + V_2(\mathbf{r} \cdot \mathbf{s} + vt), \end{aligned} \quad (2.31)$$

where V_1 and V_2 are arbitrary functions.

We see that the argument of V_1 is unchanged when (ζ, t) is replaced by $(\zeta + v\tau, t + \tau)$, where τ is arbitrary. Hence V_1 represents a disturbance which is propagated with velocity v in the positive ζ direction. Similarly $V_2(\zeta + vt)$ represents a disturbance which is propagated with velocity v in the negative ζ direction.

2.5 Vector waves

2.5.1 The general electromagnetic plane wave

The simplest electromagnetic field is that of a plane wave; then each Cartesian component of the field vectors and consequently \mathbf{E} and \mathbf{H} are, according to the previous section, functions of the variable $u = \mathbf{r} \cdot \mathbf{s} - vt$ only:

$$\mathbf{E} = \mathbf{E}(\mathbf{r} \cdot \mathbf{s} - vt), \quad \mathbf{H} = \mathbf{H}(\mathbf{r} \cdot \mathbf{s} - vt), \quad (2.32)$$

\mathbf{s} denoting as before a unit vector in the direction of propagation. Denoting by a dot differentiation with respect to t , and by a prime differentiation with respect to the variable u , we have

$$\begin{cases} \dot{\mathbf{E}} = -v\mathbf{E}' \\ (\nabla \times \mathbf{E})_x = \frac{\partial E_z}{\partial y} - \frac{\partial E_y}{\partial z} = E'_z s_y - E'_y s_z = (\mathbf{s} \times \mathbf{E}')_x. \end{cases} \quad (2.33)$$

Substituting these expressions into Maxwell's equations (2.1), (2.2) with $\mathbf{j} = 0$, and using the material equations (2.10), (2.11) we obtain

$$\begin{cases} \mathbf{s} \times \mathbf{H}' + \varepsilon v \mathbf{E}' = 0 \\ \mathbf{s} \times \mathbf{E}' - \mu v \mathbf{H}' = 0 \end{cases} \quad (2.34)$$

If we set the additive constants of integration equal to zero (i.e. neglect a field constant in space) and set $v = 1/\sqrt{\varepsilon\mu}$, (2.34) gives, on integration,

$$\begin{cases} \mathbf{E} = -\sqrt{\frac{\mu}{\varepsilon}} \mathbf{s} \times \mathbf{H}, \\ \mathbf{H} = \sqrt{\frac{\varepsilon}{\mu}} \mathbf{s} \times \mathbf{E}. \end{cases} \quad (2.35)$$

Scalar multiplication with \mathbf{s} gives

$$\mathbf{E} \cdot \mathbf{s} = \mathbf{H} \cdot \mathbf{s} = 0. \quad (2.36)$$

This relation expresses the *transversality* of the field, i.e. it shows that the electric and magnetic field vectors lie in planes normal to the direction of propagation. From (2.35) and (2.36) it is seen that \mathbf{E} , \mathbf{H} and \mathbf{s} form a right-handed orthogonal triad of vectors. We also have from (2.35) that

$$\sqrt{\mu}H = \sqrt{\varepsilon}E, \quad (2.37)$$

where $E = |\mathbf{E}|$, $H = |\mathbf{H}|$.

2.5.2 The harmonic electromagnetic plane wave

Of particular interest is the case when the plane wave is time-harmonic, i.e. when each Cartesian component of \mathbf{E} and \mathbf{H} is of the form

$$a \cos(\tau + \delta) = \mathcal{R} \left\{ a e^{-i(\tau + \delta)} \right\} \quad (a > 0). \quad (2.38)$$

Here τ denotes the variable part of the phase factor, i.e.

$$\tau = \omega \left(t - \frac{\mathbf{r} \cdot \mathbf{s}}{v} \right) = \omega t - \mathbf{k} \cdot \mathbf{r}. \quad (2.39)$$

We choose the z-axis in the \mathbf{s} direction. Then, since according to (2.36) the field is transversal, only the x - and y -components of \mathbf{E} and \mathbf{H} are different from zero. We shall now consider the nature of the curve which the end point of the electric vector describes at a typical point in space; this curve is the locus of the points whose coordinates (E_x, E_y) are

$$\begin{cases} E_x = a_1 \cos(\tau + \delta_1), \\ E_y = a_2 \cos(\tau + \delta_2). \end{cases} \quad (2.40)$$

Elliptic polarization

In order to eliminate τ between the first two equations of (2.40), we re-write them in the form

$$\begin{cases} \frac{E_x}{a_1} = \cos \tau \cos \delta_1 - \sin \tau \sin \delta_1, \\ \frac{E_y}{a_2} = \cos \tau \cos \delta_2 - \sin \tau \sin \delta_2. \end{cases} \quad (2.41)$$

Hence

$$\begin{cases} \frac{E_x}{a_1} \sin \delta_2 - \frac{E_y}{a_2} \sin \delta_1 = \cos \tau \sin(\delta_2 - \delta_1), \\ \frac{E_x}{a_1} \cos \delta_2 - \frac{E_y}{a_2} \cos \delta_1 = \sin \tau \sin(\delta_2 - \delta_1). \end{cases} \quad (2.42)$$

Squaring and adding gives

$$\left(\frac{E_x}{a_1} \right)^2 + \left(\frac{E_y}{a_2} \right)^2 - 2 \frac{E_x E_y}{a_1 a_2} \cos \delta = \sin^2 \delta, \quad (2.43)$$

where

$$\delta = \delta_2 - \delta_1. \quad (2.44)$$

Eq. (2.43) is the equation of a conic. It is an ellipse, since the associated determinant is not negative:

$$\begin{vmatrix} \frac{1}{a_1^2} & -\frac{\cos \delta}{a_1 a_2} \\ -\frac{\cos \delta}{a_1 a_2} & \frac{1}{a_2^2} \end{vmatrix} = \frac{1}{a_1^2 a_2^2} (1 - \cos^2 \delta) = \frac{\sin^2 \delta}{a_1^2 a_2^2} \geq 0. \quad (2.45)$$

The ellipse is inscribed in a rectangle whose sides are parallel to the coordinate axes and whose lengths are $2a_1$ and $2a_2$ (Fig. 2.1). The ellipse touches the sides at the point $(\pm a_1, \pm a_2 \cos \delta)$ and $(\pm a_1 \cos \delta, \pm a_2)$.

The wave (2.40) is then said to be *elliptically polarized*. It is easily seen that the wave associated with the magnetic vector is also elliptically polarized. From (2.35) and (2.40)

$$\begin{cases} H_x = -\sqrt{\frac{\varepsilon}{\mu}} E_y = -\sqrt{\frac{\varepsilon}{\mu}} a_2 \cos(\tau + \delta_2), \\ H_y = \sqrt{\frac{\varepsilon}{\mu}} E_x = \sqrt{\frac{\varepsilon}{\mu}} a_1 \cos(\tau + \delta_1). \end{cases} \quad (2.46)$$

The end point of the magnetic vector therefore describes an ellipse which is inscribed into a rectangle whose sides are parallel to the x and y directions and whose lengths are $2\sqrt{\varepsilon/\mu} a_2, 2\sqrt{\varepsilon/\mu} a_1$.

In general the axes of the ellipse are not in the Ox and Oy directions. Let $O\xi, O\eta$ be a new set of axes along the axes of the ellipse and let ψ ($0 \leq \psi < \pi$) be the angle between Ox and the direction $O\xi$ of the major axis (Fig. 2.1). Then the components E_ξ and E_η are related to E_x and E_y by

$$\begin{cases} E_\xi = E_x \cos \psi + E_y \sin \psi, \\ E_\eta = -E_x \sin \psi + E_y \cos \psi. \end{cases} \quad (2.47)$$

If $2a$ and $2b$ ($a \geq b$) are the lengths of the axes of the ellipse, the equation of the ellipse referred to $O\xi, O\eta$ is:

$$\begin{cases} E_\xi = a \cos(\tau + \delta_0), \\ E_\eta = \pm b \sin(\tau + \delta_0). \end{cases} \quad (2.48)$$

The two signs distinguish the two possible senses in which the end point of the electric vector may describe the ellipse [5, 6].

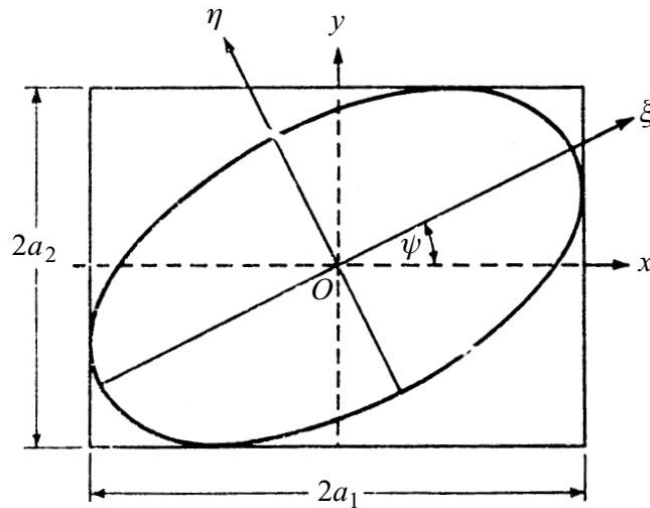


Figure 2.1: Elliptically polarized wave. The vibrational ellipse for the electric vector.

To determine a and b we compare (2.47) and (2.48) and use (2.41):

$$\begin{aligned}
a(\cos \tau \cos \delta_0 - \sin \tau \sin \delta_0) &= a_1(\cos \tau \cos \delta_1 - \sin \tau \sin \delta_1) \cos \psi \\
&\quad + a_2(\cos \tau \cos \delta_2 - \sin \tau \sin \delta_2) \sin \psi; \\
\pm b(\sin \tau \cos \delta_0 - \cos \tau \sin \delta_0) &= -a_1(\cos \tau \cos \delta_1 - \sin \tau \sin \delta_1) \sin \psi \\
&\quad + a_2(\cos \tau \cos \delta_2 - \sin \tau \sin \delta_2) \cos \psi.
\end{aligned}$$

Next we equate the coefficients of $\cos \tau$ and $\sin \tau$:

$$a \cos \delta_0 = a_1 \cos \delta_1 \cos \psi + a_2 \cos \delta_2 \sin \psi, \quad (2.49a)$$

$$a \sin \delta_0 = a_1 \sin \delta_1 \cos \psi + a_2 \sin \delta_2 \sin \psi, \quad (2.49b)$$

$$\pm b \cos \delta_0 = a_1 \sin \delta_1 \sin \psi - a_2 \sin \delta_2 \cos \psi, \quad (2.49c)$$

$$\pm b \sin \delta_0 = -a_1 \cos \delta_1 \sin \psi + a_2 \cos \delta_2 \cos \psi. \quad (2.49d)$$

On squaring and adding (2.49a) and (2.49b) and using (2.44) we obtain

$$a^2 = a_1^2 \cos^2 \psi + a_2^2 \sin^2 \psi + 2a_1 a_2 \cos \psi \sin \psi \cos \delta,$$

and similarly from (2.49c) and (2.49d)

$$b^2 = a_1^2 \sin^2 \psi + a_2^2 \cos^2 \psi - 2a_1 a_2 \cos \psi \sin \psi \cos \delta.$$

Hence

$$a^2 + b^2 = a_1^2 + a_2^2. \quad (2.50)$$

Next we multiply (2.49a) by (2.49c), (2.49b) by (2.49d) and add. This gives

$$\mp ab = a_1 a_2 \sin \delta. \quad (2.51)$$

Further on dividing (2.49c) by (2.49a) and (2.49d) by (2.49b) we obtain

$$\pm \frac{b}{a} = \frac{a_1 \sin \delta_1 \sin \psi - a_2 \sin \delta_2 \cos \psi}{a_1 \cos \delta_1 \cos \psi + a_2 \cos \delta_2 \sin \psi} = \frac{-a_1 \cos \delta_1 \sin \psi + a_2 \cos \delta_2 \cos \psi}{a_1 \sin \delta_1 \cos \psi + a_2 \sin \delta_2 \sin \psi},$$

and these relations give the following equation for ψ :

$$(a_1^2 - a_2^2) \sin 2\psi = 2a_1 a_2 \cos \delta \cos 2\psi.$$

It will be convenient to introduce an auxiliary angle α ($0 \leq \alpha \leq \pi/2$), such that

$$\frac{a_2}{a_1} = \tan \alpha. \quad (2.52)$$

The preceding equation then becomes

$$\tan 2\psi = \frac{2a_1 a_2}{a_1^2 - a_2^2} \cos \delta = \frac{2 \tan \alpha}{1 - \tan^2 \alpha} \cos \delta,$$

i.e.

$$\tan 2\psi = \tan(2\alpha) \cos \delta. \quad (2.53)$$

Now from (2.50) and (2.51) we also have

$$\mp \frac{2ab}{a^2 + b^2} = \frac{2a_1 a_2}{a_1^2 + a_2^2} \sin \delta = \sin(2\alpha) \sin \delta. \quad (2.54)$$

Let χ ($-\pi/4 \leq \chi \leq \pi/4$) be another auxiliary angle, such that

$$\mp \frac{b}{a} = \tan \chi. \quad (2.55)$$

The numerical value of $\tan \chi$ represents the ratio of the axes of the ellipse and the sign of χ distinguishes the two senses in which the ellipse may be described. Eq. (2.54) may be written in the form

$$\sin 2\chi = \sin(2\alpha) \sin \delta. \quad (2.56)$$

It will be useful to summarize the results. If a_1, a_2 and the phase difference δ are given, referred to an arbitrary set of axes, and if α ($0 \leq \alpha \leq \pi/2$) denotes an angle such that

$$\tan \alpha = \frac{a_2}{a_1}, \quad (2.57)$$

then the principal semiaxes a and b of the ellipse and the angle ψ ($0 \leq \psi < \pi$) which the major axis makes with Ox are specified with the formulae

$$a^2 + b^2 = a_1^2 + a_2^2, \quad (2.58a)$$

$$\tan 2\psi = \tan(2\alpha) \cos \delta, \quad (2.58b)$$

$$\sin 2\chi = \sin(2\alpha) \sin \delta, \quad (2.58c)$$

where χ ($-\pi/4 < \chi \leq \pi/4$) is an auxiliary angle which specifies the shape and orientation of the vibrational ellipse:

$$\tan \chi = \mp b/a. \quad (2.59)$$

Conversely, if the lengths a and b of the axes and the orientation of the ellipse are known (i.e. a, b and ψ given) these formulae enable the determination of the amplitudes a_1, a_2 and the phase difference δ .

Before discussing some important special cases, we must say a few words about the terminology. We distinguish two cases of polarization, according to the sense in which the end point of the electric vector describes the ellipse. It seems natural to call the polarization right-handed or left-handed according to whether the rotation of \mathbf{E} and the direction of propagation form a right-handed or left-handed screw. But the traditional terminology is just the opposite, being based on the apparent behaviour of \mathbf{E} when 'viewed' face on by the observer. We say that the polarization is *right-handed* when to an observer looking in the direction from which the light is coming, the end point of the electric vector would appear to describe the ellipse in the clockwise sense. If we consider the values of (2.40) for two time instants separated by a quarter of a period, we see that in this case $\sin \delta > 0$, or by (2.56), $0 < \chi \leq \pi/4$. For *left-handed* polarization the opposite is the case, i.e. to an observer looking in the direction from which the light is propagated, the electric vector would appear to describe the ellipse anti-clockwise; in this case $\sin \delta < 0$, so that $-\pi/4 \leq \chi < 0$.

Linear and circular polarization

Two special cases are of particular importance, namely when the polarization ellipse degenerates into a straight line or a circle.

According to (2.40) the ellipse will reduce to a straight line when

$$\delta = \delta_2 - \delta_1 = m\pi \quad (m = 0, \pm 1, \pm 2, \dots). \quad (2.60)$$

Then

$$\frac{E_y}{E_x} = (-1)^m \frac{a_2}{a_1}, \quad (2.61)$$

and we say that \mathbf{E} is *linearly polarized*. One of the coordinate axes, x say, may be chosen along this line. Then only one component (E_x) remains. Moreover, since the electric and magnetic vectors are orthogonal and lie in the plane perpendicular to the z direction, the component H_x then vanishes, so that \mathbf{H} is linearly polarized in the y direction.

The other special case of importance is that of a *circularly polarized* wave, the ellipse then degenerating into a circle. Clearly a necessary condition for this is that the circumscribed rectangle shall become a square:

$$a_1 = a_2 = a. \quad (2.62)$$

Also, one of the \mathbf{E} components must be zero when the other has an extreme value; this demands that

$$\delta = \delta_2 - \delta_1 = m\pi/2 \quad (m = \pm 1, \pm 3, \pm 5, \dots), \quad (2.63)$$

and (2.43) then reduces to the equation of the circle

$$E_x^2 + E_y^2 = a^2. \quad (2.64)$$

When the polarization is *right-handed* $\sin \delta > 0$, so that

$$\delta = \frac{\pi}{2} + 2m\pi \quad (m = 0, \pm 1, \pm 2, \dots), \quad (2.65)$$

$$\begin{cases} E_x = a \cos(\tau + \delta_1), \\ E_y = a \cos(\tau + \delta_1 + \pi/2) = -a \sin(\tau + \delta_1). \end{cases} \quad (2.66)$$

For *left-handed* polarization $\sin \delta < 0$, so that

$$\delta = -\frac{\pi}{2} + 2m\pi \quad (m = 0, \pm 1, \pm 2, \dots), \quad (2.67)$$

$$\begin{cases} E_x = a \cos(\tau + \delta_1), \\ E_y = a \cos(\tau + \delta_1 - \pi/2) = a \sin(\tau + \delta_1). \end{cases} \quad (2.68)$$

If, instead of the real representation, the complex one is used (i.e. if the exponential instead of the cosine function is written in (2.40)), then

$$\frac{E_y}{E_x} = \frac{a_2}{a_1} e^{i(\delta_1 - \delta_2)} = \frac{a_2}{a_1} e^{-i\delta}, \quad (2.69)$$

and one can immediately determine from the value of this ratio the nature of the polarization. One has for

(i) *Linearly polarized electric wave* ($\delta = m\pi, m = 0, \pm 1, \pm 2, \dots$):

$$E_y/E_x = (-1)^m \frac{a_2}{a_1}.$$

(ii) *Right-handed circularly polarized electric wave* ($a_1 = a_2, \delta = \pi/2$):

$$E_y/E_x = e^{-i\pi/2} = -i.$$

(iii) *Left-handed circularly polarized electric wave* ($a_1 = a_2, \delta = -\pi/2$):

$$E_y/E_x = e^{i\pi/2} = i.$$

More generally it may be shown that for right-handed elliptical polarization, the ratio E_y/E_x has a negative imaginary part, whereas for left-handed elliptical polarization the imaginary part is positive.

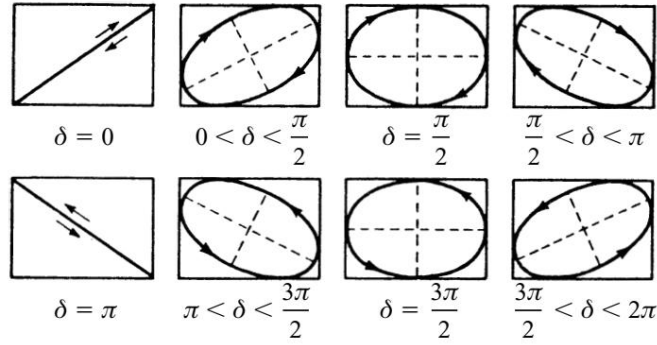


Figure 2.2: Elliptical polarization with various values of the phase difference δ .

Fig. 2.2 illustrates how the polarization ellipse changes with varying δ .

2.6 Stokes parameters

To characterize the polarization ellipse, three independent quantities are needed, e.g. the amplitudes a_1 and a_2 and the phase difference δ , or the major and minor axes, a, b and the angle χ which specifies the orientation of the ellipse. For practical purposes it is convenient to characterize the state of polarization by certain parameters which are all of the same physical dimensions, and which are easily determined with a set of 4 intensity measurements. The so-called *Stokes parameters* were introduced by G. G. Stokes in 1852, in his investigations relating to partially polarized light [7]. The Stokes parameters of a plane monochromatic wave are the four quantities

$$\begin{cases} S_0 = a_1^2 + a_2^2, \\ S_1 = a_1^2 - a_2^2, \\ S_2 = 2a_1a_2 \cos \delta, \\ S_3 = 2a_1a_2 \sin \delta. \end{cases} \quad (2.70)$$

Only three of them are independent since they are related by the identity

$$S_0^2 = S_1^2 + S_2^2 + S_3^2. \quad (2.71)$$

The parameter S_0 is evidently proportional to the intensity of the wave. The parameters S_1, S_2 and S_3 are related in a simple way to the angle ψ ($0 \leq \psi <$

π) which specifies the orientation of the ellipse and the angle χ ($-\pi/4 \leq \chi \leq \pi/4$) which characterizes the ellipticity and the sense in which the ellipse is being described. In fact the following relations hold:

$$S_1 = S_0 \cos 2\chi \cos 2\psi, \quad (2.72a)$$

$$S_2 = S_0 \cos 2\chi \sin 2\psi, \quad (2.72b)$$

$$S_3 = S_0 \sin 2\chi. \quad (2.72c)$$

The relation (2.72c) follows from (2.52) and (2.56). To derive the other two relations we note that according to the equation preceding (2.53),

$$S_2 = S_1 \tan 2\psi. \quad (2.73)$$

The relation (2.72a) follows on substitution from (2.73) and from (2.72c) into (2.71). Finally, (2.72b) is obtained on substitution from (2.72a) into (2.73).

The relations (2.72) indicate a simple geometrical representation of all the different states of polarization: S_1 , S_2 and S_3 may be regarded as the Cartesian coordinates of a point P on a sphere Σ of radius S_0 , such that 2χ and 2ψ are the spherical angular coordinates of this point (see Fig. 2.3). Thus to every possible state of polarization of a plane monochromatic wave of a given intensity ($S_0 = \text{constant}$), there corresponds one point on Σ and vice versa. Since χ is positive or negative according as the polarization is right-handed or left-handed, it follows from (2.72c) that right-handed polarization is represented by points on Σ which lie above the equatorial plane (xy -plane), and left-handed polarization by points on Σ which lie below this plane. Further, for linearly polarized light the phase difference δ is zero or an integral multiple of π ; according to (2.70) the Stokes parameter S_3 is then zero, so that linear polarization is represented by points in the equatorial plane. For circular polarization $a_1 = a_2$ and $\delta = \pi/2$ or $-\pi/2$ according as the polarization is right- or left-handed; hence right-handed circular polarization is represented by the north pole ($S_1 = S_2 = 0, S_3 = S_0$) and left-handed circular polarization by the south pole ($S_1 = S_2 = 0, S_3 = -S_0$). This geometrical representation of different states of polarization by points on a sphere is due to Poincaré, and the sphere Σ is called the *Poincaré sphere*.

The four Stokes parameters associated with a beam can be regarded as the elements of a 4×1 matrix, which we shall call the Stokes column of the beam, representing it by a bold symbol \mathbf{S} :

$$\mathbf{S} = \begin{bmatrix} S_0 \\ S_1 \\ S_2 \\ S_3 \end{bmatrix} \quad (2.74)$$

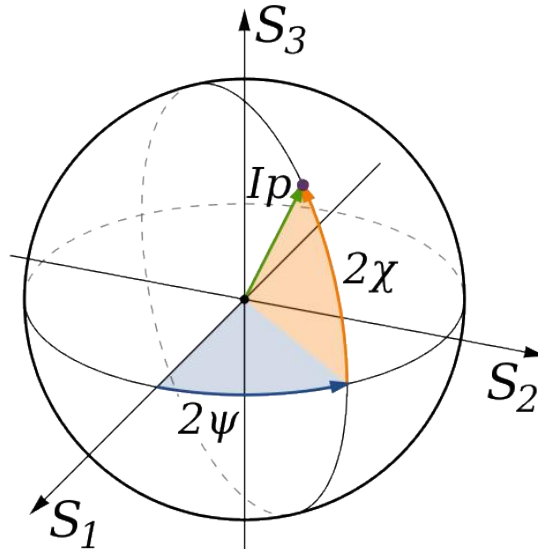


Figure 2.3: Poincaré's representation of the state of polarization of a monochromatic wave.

2.7 Alternative explanation

All possible states of polarization, including partial polarization, can be represented by a set of three real numbers. They can be conveniently complemented by the light intensity, giving the total of four real, experimentally accessible quantities, called Stokes parameters.

The Stokes parameters are defined using a fixed x - y coordinate system in the plane of polarization. Each of the parameters has the dimension of intensity, and a fairly simple interpretation in experimental measurements.

Let us denote by I_0 the total intensity of an analyzed beam. Further, let I_x , I_y , $I_{\pi/4}$, and $I_{-\pi/4}$ denote the intensities passed through an ideal linear polarizer aligned at the angles of 0 , $\pi/2$, $\pi/4$, and $-\pi/4$, respectively. Finally, let I_R and I_L be the intensities transmitted by ideal right- and left-circular polarizers, respectively. The four Stokes parameters, grouped in the column vector \mathbf{S} , can be defined as

$$\mathbf{S} = \begin{bmatrix} S_0 \\ S_1 \\ S_2 \\ S_3 \end{bmatrix} = \begin{bmatrix} I_0 \\ I_x - I_y \\ I_{\pi/4} - I_{-\pi/4} \\ I_R - I_L \end{bmatrix} \quad (2.75)$$

Note that $I_0 = I_x + I_y = I_{\pi/4} + I_{-\pi/4} = I_R + I_L$.

This definition provides an alternative description of the polarization state which is experimentally convenient because each parameter corresponds to a sum or difference of measurable intensities.

For unpolarized light all three differences of intensities in Eq. (2.75) vanish, and the (row) Stokes vector is $S_{unpol} = [I_0, 0, 0, 0]$.

On the other hand, a totally elliptically polarized beam, characterized by the

azimuth and ellipticity angles (ψ, χ) , has the Stokes vector

$$\mathbf{S}_\chi = S_0 \begin{bmatrix} 1 \\ \cos 2\chi \cos 2\psi \\ \cos 2\chi \sin 2\psi \\ \sin 2\chi \end{bmatrix} \quad (2.76)$$

This result is obtained by substitutions of the intensities for corresponding azimuths into the definition (2.75) of the Stokes vector. For the elliptical polarization orthogonal to that of Eq. (2.76), the Stokes vector changes sign of the S_1 , S_2 , and S_3 components:

$$\mathbf{S}_{-1/\chi^*} = S_0 \begin{bmatrix} 1 \\ -\cos 2\chi \cos 2\psi \\ -\cos 2\chi \sin 2\psi \\ -\sin 2\chi \end{bmatrix} \quad (2.77)$$

this is easily seen from the orthogonality of the azimuths, and the change of sign of the ellipticity angle. Note that the Stokes vectors of the orthogonal polarization states are orthogonal in the usual sense, i.e. their scalar (inner) product vanishes,

$$\mathbf{S}_\chi^T \mathbf{S}_{-1/\chi^*} = S_0^2 \left[1 - \cos^2 2\chi (\cos^2 2\psi + \sin^2 2\psi) - \sin^2 2\chi \right] = 0. \quad (2.78)$$

The Stokes vectors of linear and circular polarizations are

$$\mathbf{S}_{lin} = S_0 \begin{bmatrix} 1 \\ \cos 2\psi \\ \sin 2\psi \\ 0 \end{bmatrix}, \quad \mathbf{S}_{circ} = S_0 \begin{bmatrix} 1 \\ 0 \\ 0 \\ \pm 1 \end{bmatrix}, \quad (2.79)$$

where ψ is the azimuth of the linear polarization, and the plus and minus signs in \mathbf{S}_{circ} represent the right- and left-circular polarizations, respectively.

Only two real parameters describing the state of polarization are involved in the Stokes vector \mathbf{S}_χ (2.76), due to the independence of the intensity S_0 . For totally polarized light we have

$$S_0^2 = S_1^2 + S_2^2 + S_3^2 \quad \text{or} \quad (S_3/S_0)^2 = 1 - (S_1/S_0)^2 - (S_2/S_0)^2 \quad (2.80)$$

resulting from Eq. (2.76), demonstrating the interdependence of the three *relative* intensities.

The general case of a partially polarized beam is more complex. We assume each of the incoming photons to be in the same mixed state; we only have the probability w_χ of being passed through the corresponding aligned elliptic polarizer, or the probability $1 - w_\chi$ of being stopped by it. The latter occurs whenever the incoming photon happens to be in the orthogonal polarization state $-1/\chi^*$. Thus, the measured signals are composed of two contributions, \mathbf{S}_χ and \mathbf{S}_{-1/χ^*} , weighted by the probabilities w_χ and $1 - w_\chi$. Using Eqs. (2.76) and (2.77), the resulting Stokes vector can be put in the form

$$\begin{aligned} \mathbf{S}_{\chi,part} &= w_\chi \mathbf{S}_\chi + (1 - w_\chi) \mathbf{S}_{-1/\chi^*} \\ &= S_0 (2w_\chi - 1) \begin{bmatrix} 1 \\ \cos 2\chi \cos 2\psi \\ \cos 2\chi \sin 2\psi \\ \sin 2\chi \end{bmatrix} + S_0 2(1 - w_\chi) \begin{bmatrix} 1 \\ 0 \\ 0 \\ 0 \end{bmatrix} \quad \text{for } w_\chi \in \left[\frac{1}{2}, 1 \right]. \end{aligned} \quad (2.81)$$

We have limited the range of probabilities in order to obtain the simple form of the result. The probabilities w_χ from zero to $1/2$ are actually included in Eq. (2.81) when used for the orthogonal polarization, $-1/\chi^*$. The statistical mixture of the two orthogonal polarization states behaves as the incoherent addition of the fully polarized and unpolarized waves. Inserting $w_\chi = 1/2$ into Eq. (2.81), we obtain the Stokes vector of unpolarized light; it should be noted that this result is independent of the basis used to define the unique mixed state of maximum entropy. Observable results are the same for equal mixtures of any pair of orthogonal polarizations.

The state of partial polarization described by the Stokes vector of Eq. (2.81) is defined by three real numbers. The real quantity to be added to the two real characteristics of the limiting elliptic polarization can be the *degree of polarization*. It is defined as the ratio of the intensity of the polarized part to the total intensity,

$$P_\chi = \frac{\sqrt{S_1^2 + S_2^2 + S_3^2}}{S_0} = 2w_\chi - 1. \quad (2.82)$$

The degree of polarization varies from zero for $w_\chi = 1/2$ to unity for the totally polarized light of $w_\chi = 1$. In place of Eq. (2.80) the Stokes parameters satisfy in general the following inequality,

$$S_1^2 + S_2^2 + S_3^2 \leq S_0^2 \quad (2.83)$$

where the equality holds for the totally polarized light, $P_\chi = 1$. Using the degree of polarization, the Stokes vector of Eq. (2.81) can be written as

$$\mathbf{S}_{\chi,part} = S_0 [P_\chi \tilde{\mathbf{S}}_\chi + (1 - P_\chi) \tilde{\mathbf{S}}_{unpol}]. \quad (2.84)$$

Here S_0 is the total intensity and the vectors

$$\tilde{\mathbf{S}}_\chi = \begin{bmatrix} 1 \\ \cos 2\chi \cos 2\psi \\ \cos 2\chi \sin 2\psi \\ \sin 2\chi \end{bmatrix}, \quad \tilde{\mathbf{S}}_{unpol} = \begin{bmatrix} 1 \\ 0 \\ 0 \\ 0 \end{bmatrix} \quad (2.85)$$

represent the directions of the elliptically polarized and unpolarized light, in the four-dimensional space of Stokes vectors.

2.8 Mueller calculus

We shall show that for any type of device, that is for a polaroid sheet with its pass-plane at any angle with the axis, for a phase plate of any retardation and any orientation of the fast axis, and for a rotator which merely twists the plane of polarization like certain organic liquids, the Stokes parameters of the beam coming out of the device are linear functions of the four Stokes parameters of the input beam. Thus:

$$S_0^{\text{out}} = M_{11}S_0^{\text{in}} + M_{12}S_1^{\text{in}} + M_{13}S_2^{\text{in}} + M_{14}S_3^{\text{in}}$$

$$S_1^{\text{out}} = M_{21}S_0^{\text{in}} + M_{22}S_1^{\text{in}} + M_{23}S_2^{\text{in}} + M_{24}S_3^{\text{in}}$$

$$S_2^{\text{out}} = M_{31}S_0^{\text{in}} + M_{32}S_1^{\text{in}} + M_{33}S_2^{\text{in}} + M_{34}S_3^{\text{in}}$$

$$S_3^{\text{out}} = M_{41}S_0^{\text{in}} + M_{42}S_1^{\text{in}} + M_{43}S_2^{\text{in}} + M_{44}S_3^{\text{in}}$$

where S_i^{in} refers to the i -th Stokes parameter of the input beam, S_i^{out} is the Stokes parameter of the beam leaving the device, and the M_{ij} coefficients are characteristic only of the device and its orientation. We can write these equations in matrix form as

$$\begin{bmatrix} S_0^{\text{out}} \\ S_1^{\text{out}} \\ S_2^{\text{out}} \\ S_3^{\text{out}} \end{bmatrix} = \begin{bmatrix} M_{11} & M_{12} & M_{13} & M_{14} \\ M_{21} & M_{22} & M_{23} & M_{24} \\ M_{31} & M_{32} & M_{33} & M_{34} \\ M_{41} & M_{42} & M_{43} & M_{44} \end{bmatrix} \begin{bmatrix} S_0^{\text{in}} \\ S_1^{\text{in}} \\ S_2^{\text{in}} \\ S_3^{\text{in}} \end{bmatrix}$$

that is

$$\mathbf{S}^{\text{out}} = M\mathbf{S}^{\text{in}}$$

Here, \mathbf{S}^{in} is the Stokes column of the beam entering the device, \mathbf{S}^{out} is the Stokes column of the beam leaving the device and M is a 4×4 matrix which is characteristic of the device and its orientation and which is called, after its inventor, the Mueller matrix of the device.

The Mueller matrix scheme can handle propagation of partially polarized light through optical systems, including possible depolarizing elements. It transforms Stokes vectors by successive multiplications with 4×4 matrices belonging to individual optical elements. Thus, if a beam passes through a series of devices in succession, we can find the nature of the emerging beam, knowing only the nature of the original beam and the devices through which it passes. In particular, a cascade of polarizing elements transforms an input Stokes vector into the output vector

$$\mathbf{S}^{\text{out}} = M_n \cdots M_2 M_1 \mathbf{S}^{\text{in}}. \quad (2.86)$$

Since the Stokes vectors are defined with respect to a definite coordinate system within the plane of polarization, special Mueller matrices are needed to change the coordinate systems. A rotation by the angle α has a Mueller matrix given by

$$R(\alpha) = \begin{bmatrix} 1 & 0 & 0 & 0 \\ 0 & \cos 2\alpha & \sin 2\alpha & 0 \\ 0 & -\sin 2\alpha & \cos 2\alpha & 0 \\ 0 & 0 & 0 & 1 \end{bmatrix}. \quad (2.87)$$

Listed below are the Mueller matrices that describe the operation of various frequently employed devices [8].

Ideal linear polarizer at angle θ

$$\frac{1}{2} \begin{bmatrix} 1 & \cos 2\theta & \sin 2\theta & 0 \\ \cos 2\theta & \cos^2 2\theta & \cos 2\theta \sin 2\theta & 0 \\ \sin 2\theta & \cos 2\theta \sin 2\theta & \sin^2 2\theta & 0 \\ 0 & 0 & 0 & 0 \end{bmatrix}$$

Quarter-wave linear retarder with fast axis at angle θ

$$\begin{bmatrix} 1 & 0 & 0 & 0 \\ 0 & \cos^2 2\theta & \cos 2\theta \sin 2\theta & -\sin 2\theta \\ 0 & \cos 2\theta \sin 2\theta & \sin^2 2\theta & \cos 2\theta \\ 0 & \sin 2\theta & -\cos 2\theta & 0 \end{bmatrix}$$

Half-wave linear retarder with fast axis at angle θ

$$\begin{bmatrix} 1 & 0 & 0 & 0 \\ 0 & \cos 4\theta & \sin 4\theta & 0 \\ 0 & \sin 4\theta & -\cos 4\theta & 0 \\ 0 & 0 & 0 & -1 \end{bmatrix}$$

Chapter 3

Polarimetry

In this section I'm going to describe the work I did in the field of XUV polarimetry. The main goals of this work are:

- demonstrate the higher efficiency of ruthenium-coated optics with respect to standard gold-coated ones, in the 50 eV – 100 eV photon energy range;
- test the performance of the low-cost in-house developed solution;
- show the straightforward and fast alignment procedure of the proposed system;
- perform some ellipsometric measurements with thin film samples.

Polarimetry is the study of the polarization state of electromagnetic radiation. As seen in the previous section, the polarization state of an electromagnetic wave can be completely characterized by its Stokes vector. Therefore, by finding the Stokes parameter of a beam of light, we are completely describing the state of polarization of that beam, in a given moment of time. Knowing and controlling the polarization state of a XUV source is of fundamental importance in many fields, such as ellipsometry [9, 10], ultrafast electron dynamics [11–13], time-resolved tomography of atomic or molecular wavefunctions [14], ultrafast circular dichroism of molecules and magnetic materials [15, 16], non-collinear high harmonic generation [17, 18], as well as astronomical science, weather science, and remote sensing [19–21]. Correspondingly, there has been an increasing demand for systems to measure and control polarization in the extreme ultraviolet (XUV) and soft x-ray spectral regions.

3.1 Polarization in the visible spectral range

There are several methods of causing a light beam to be polarized. Perhaps the simplest method is by reflection. This was discovered by Malus in about 1808 [22] and fully explained by Brewster (circa 1830) [23].

Another method is by dichroism. In one manifestation, organic materials are embedded into a plastic sheet and then stretched. This is then dyed and the dye molecules selectively attach themselves to the aligned molecules. This causes the absorption of light to be high in one plane and low in another. This is the polarization mechanism of large-area sheet polarizers (Polaroid sheets). In another

manifestation, passing light through the crystal tourmaline was observed to give polarized light [24].

Yet another method is to fabricate a grid of conductive “wires”, which are spaced parallel to each other and separated by distances which are comparable to the wavelength of the light of interest. When the electric vector is waving in a direction parallel to the conductive “wires”, the electrons can follow the electric field and the electric field is attenuated and/or reflected. When the electric vector is waving in a direction perpendicular to the “wires”, the electrons cannot move out of the “wires” and hence the wave continues through the array. This type of polarizer is used frequently in infrared spectrometers.

The most common method of obtaining polarized light in the visible wavelength range is with birefringence, or double refraction. This method was first observed by Bartholinus, in 1670 and further developed by Huygens about 20 years later [25].

It was observed that when a pencil of light was made to fall onto a calcite crystal, two pencils of light emerged, one slightly offset from the other. It was discovered that each of these light beams had the special characteristics that was later described as being *polarized*, with the polarization directions being mutually perpendicular.

3.1.1 Double refraction

In an amorphous material or a symmetric crystal, light propagates at the same speed in all directions and the material is described as being isotropic. For crystals which are not symmetric in all three directions, the possibility exists that the speed of light is different in different directions. For a biaxial crystal, the speed of light (and hence the index of refraction) is different in three mutually perpendicular directions. For a uniaxial crystal, the speed is the same in two of the three directions (in the plane which contains these two axes), and different in the third direction. We will focus on uniaxial materials.

If unpolarized light is directed through an uniaxial crystal along the direction of the unique axis (called the optic axis), the light emerges unchanged. If the light is directed through the crystal in any other direction, the light is separated into two beams, the ordinary ray and the extraordinary ray, as shown in Fig. 3.1. This phenomenon is described as *double refraction* and occurs in many crystals which are not cubic.

Because of the anisotropic nature of the crystal, the index of refraction is different for light traveling along the unique axis compared to light traveling perpendicular to the unique axis. Calcite is a common material which is used in these applications, and the indices of refraction for the two different situations are shown in Fig. 3.2.

For calcite, light traveling along the optic axis has an index of refraction of n_o . Light traveling in the plane perpendicular to the optic axis with one specific polarization will have an index of refraction of n_e . Light traveling in any other direction will be separated into two beams. The ordinary ray will have an index of refraction n_o and the extraordinary ray will have an effective index of refraction which is intermediate between n_e and n_o . Accordingly, the index of refraction for the extraordinary ray is a function of angle or direction. The values shown for n_e

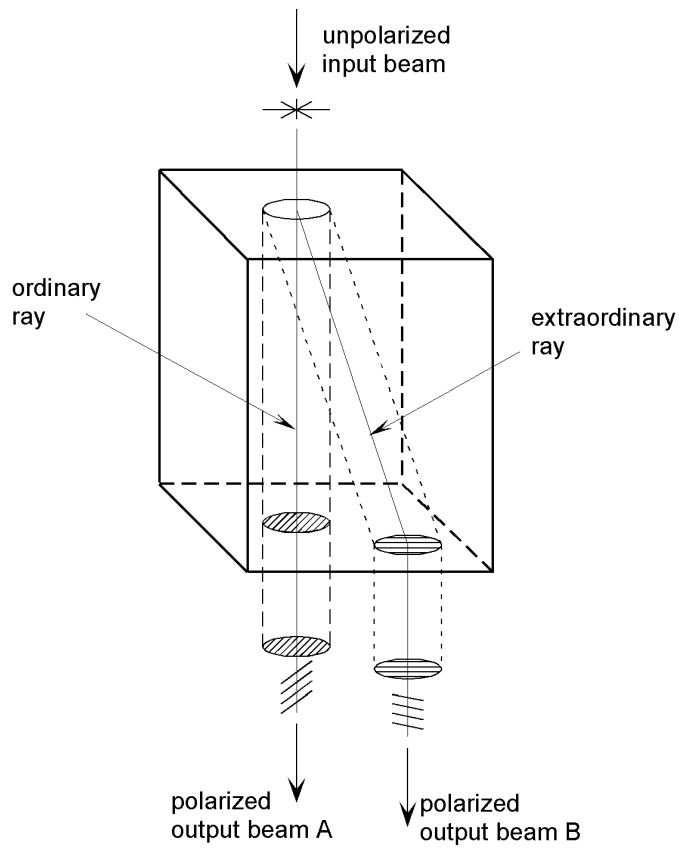


Figure 3.1: Double refraction, illustrated in a generic anisotropic material. Note that the sides of the material do not represent crystal planes.

in Fig. 3.2 are then the extreme values. The ordinary ray behaves according to the common version of Snell's law. The extraordinary ray requires a more general version of Snell's law.

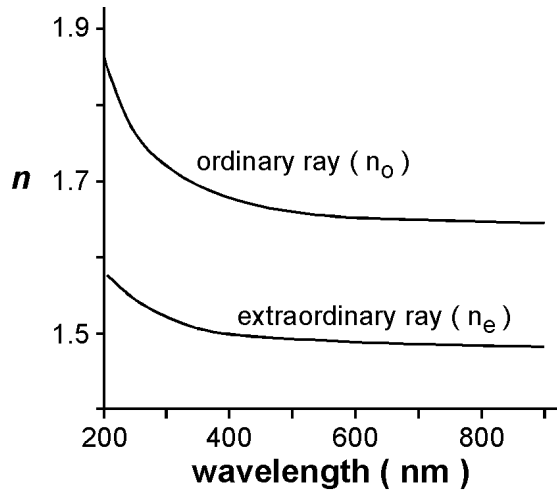


Figure 3.2: The index of refraction n for calcite in the direction of the optic axis (shown as the ordinary ray) and in the plane perpendicular to the optic axis (shown as the extraordinary ray).

3.1.2 Polarizers and analyzers

The terms “polarizer” and “analyzer” have been used in polarimetry for a very long time [24]. The device is often the same object for both cases, but in this context, the polarizer is the device which sets the state of polarization of a light beam and the analyzer is the device which determines the state of polarization of a beam after it has been altered in some way, e.g. by a reflection.

Although it was understood from the late 1600s that the calcite crystal separated light into two beams which had unique properties, it was not until 1828 that William Nicol devised the “Nicol prism” [26] and was able to remove one of the two beams from the axis of the optical instrument, thus giving a convenient polarizer.

In making the Nicol prism, the calcite crystal was polished to an appropriate shape. Note that the prism sides did not correspond to the natural crystal planes. The plane which contains the optic axis and the normal to one of the natural crystal planes is called a “principal section” and the light was made to pass through the prism in one of the principal sections.

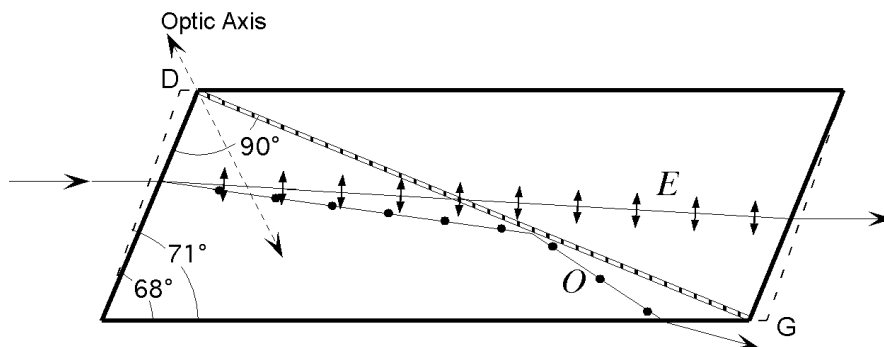


Figure 3.3: Schematic drawing of a Nicol prism, showing the principal section.

In Fig. 3.3 we show a principal section of a Nicol prism. After polishing to the appropriate shape, the crystal is then cut along the plane which is perpendicular

to the principal section and perpendicular to the ends of the crystal (now at 68° from the bottom). The two surfaces are ground and polished optically flat and then the two pieces are cemented together using Canada balsam. This material is a clear transparent substance with an index of refraction which is about midway between that of the O and E rays.

At the angles shown, the ordinary ray makes a total internal reflection at the calcite/Canada balsam interface. This beam is diverted out of the instrumental axis and is usually absorbed by the surrounding material. On the other hand, the extraordinary ray, with a lower index of refraction than the Canada balsam, does not suffer total internal reflection. It passes through the Canada balsam and into the other calcite part and subsequently out the other end of the Nicol prism. The exiting beam is polarized with the electric vector parallel to the principal section. Note that with a Nicol prism, there is a lateral displacement of the beam.

3.1.3 The Quarter-Wave Plate

Suppose we consider the incoming linearly polarized light beam to consist of two mutually perpendicular components which are in phase. It is sometimes desirable to shift the phase of the beam such that we have elliptically (or circularly) polarized light. We almost always obtain this result by passing the light through a birefringent crystal (sometimes called a “wave plate”) in such a way that the index of refraction for one component is slightly different than the index of refraction for the other component.

Suppose we have a plate where the thickness of the plate is d , and the thickness is such that an integral number of waves fits in the crystal (the wave coming out has the same phase as the wave going in). The wavelength of the light in vacuum is λ and the wavelength in the crystal is λ/n , where n is the appropriate index of refraction. Then the total number of waves in the plate is $d/(\lambda/n)$. If each of the mutually perpendicular components is controlled by a different index (e.g. n_i and n_j), then the phase difference upon emerging would be

$$\delta = 2\pi \frac{d(n_i - n_j)}{\lambda}. \quad (3.1)$$

We obtain this separation in several ways, but they all consist of arranging for the two mutually perpendicular components to pass through the wave-plate at different speeds, i.e. experiencing different values for the index of refraction.

Historically, for single-wavelength experiments, a quarter-wave plate was used. This optical element would transform linearly polarized light into elliptically or circularly polarized light, depending on the relative orientation of the quarter-wave plate to the plane of polarization of the light. Fig. 3.4 shows a simple plate retarder.

The crystal is cut such that the optical axis lies in the plane parallel to the face of the retarder plate. The light beam enters normal to the face and optic axis and hence is not deviated. In this example, the light is polarized such that the component parallel to the optic axis has the same amplitude as the component perpendicular to the optic axis. Because the ordinary and extraordinary rays travel at different speeds, the phase fronts become separated. The extraordinary ray travels faster than the ordinary ray (for a negative uniaxial crystal), hence

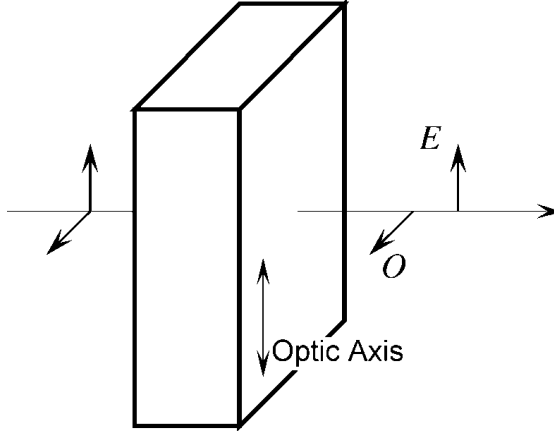


Figure 3.4: Simple retardation plate, made from a negative uniaxial material. The optic axis is shown. The crystal retards the ordinary ray O relative to the extraordinary ray E.

when the light beam emerges from the crystal, the two rays are not in phase. The phase retardation δ is given by

$$\delta = 2\pi N = \pm \frac{2\pi d(n_e - n_o)}{\lambda} \quad (3.2)$$

where d is the thickness of the plate and λ is the wavelength of the light. N is the retardation in fractions of a wavelength. If $N = 1/4$, we have a simple zero-order quarter-wave plate. If $N = 1\ 1/4, 2\ 1/4, \dots$ we have a multi-order quarter-wave plate. If $N = 1/2, 1\ 1/2, 2\ 1/2, \dots$ we have a half-wave plate.

With a quarter-wave plate, if the two components of the incoming beam are in phase, as suggested in Fig. 3.4, the emerging wave is $\pi/2$ or 90° out of phase. If the two components have equal amplitudes, the wave emerging from the wave plate will be circularly polarized. If the amplitudes of the two components are not equal, the resulting wave will be elliptically polarized. Note that if either of the components were zero, i.e. the linearly polarized wave were aligned to either the fast or slow axis, then the emerging wave would remain linearly polarized. With incident plane-polarized light, one can shift the ellipticity from linear to circularly polarized by simply changing the azimuthal orientation of the wave plate (rotation about the optical axis) relative to the orientation of the incident polarized light.

We should note that for this type of wave plate, the retardation is a function of not only the thickness, but the wavelength, hence a plate which is a quarter-wave plate for one wavelength will not be a quarter-wave plate for other wavelengths.

3.2 Polarimetry in the XUV spectral range

There are some peculiarities that made it difficult, in the past, to extend the visible and UV optical know-how to XUV wavelengths. XUV optical properties of condensed matter are to absorb most of the radiation along less than $\sim 1\ \mu\text{m}$ length and to offer an extremely poor reflectance ($\lesssim 10^{-4}$) at near normal incidence.

3.2.1 XUV refractive index

The global response of matter to the penetration of an electromagnetic field is summarized in its complex refractive index. From this index, refraction and reflection at the interfaces, as well as absorption within the medium, can be calculated. The refractive index can be deduced from the scattering of radiation by molecules, atoms, and electrons (see for instance [27–30]). As regards XUV radiation, a clear presentation of the subject can be found in Chapters 2 and 3 of [31].

The refractive index n of a material is usually defined as the square root of the dielectric constant, ε :

$$n = \sqrt{\varepsilon} \quad (3.3)$$

In the range of XUV frequencies, oscillations of bound electrons in the attractive field of atomic nuclei provide the main contribution to the dielectric constant of solid and gaseous materials. In hot dense plasmas this part is played by free-electron collective oscillations, due to the density-dependent restoring force which follows from electron density disturbances. In both cases the nuclei are too slow to significantly contribute to the material response.

The refractive index, which depends on the frequency of the incident electric field, is usually separated into real and imaginary parts (Chap. IX in [28]):

$$n(\omega) = 1 - \delta + i\beta \quad (3.4)$$

where δ and β are usually very small terms.

The behavior of δ and β near resonances is shown in Fig. 3.5.

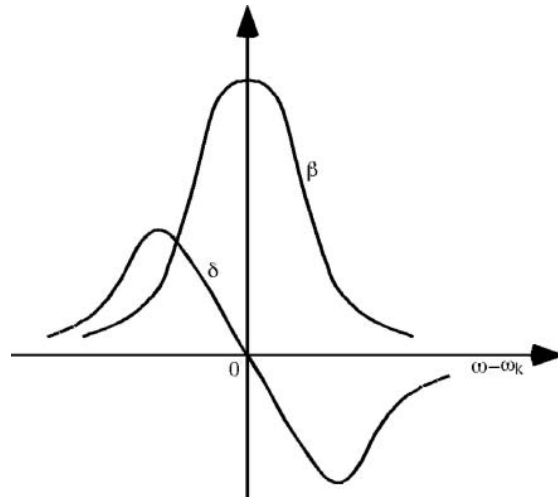


Figure 3.5: Variation of the real and imaginary parts of the refractive index, $n = 1 - \delta - i\beta$, near a resonance frequency ω_k .

3.2.2 Absorption, Reflection, and Refraction of XUV Radiation

Let us consider a scalar plane wave described by the relation

$$E = E_0 e^{-i(\omega t - kr)} \quad (3.5)$$

where $\omega = 2\pi\nu = 2\pi/T$ and $k = 2\pi/\lambda$, with ν and λ being, respectively, the frequency and the wavelength of the radiation.

In a medium of refractive index $n(\omega)$ the phase velocity dispersion of the wave reads

$$v_\phi = \frac{c}{n(\omega)} = \frac{\omega}{k} \quad (3.6)$$

Introducing $n(\omega)$ given by Eq. (3.4) in this equation gives

$$k = \frac{\omega}{c}(1 - \delta + i\beta) \quad (3.7)$$

We can then rewrite Eq. (3.5) in the form

$$E = E_0 e^{-(2\pi\beta/\lambda)r} e^{-i[\omega(t-r/c)+(2\pi\delta/\lambda)r]} \quad (3.8)$$

which shows the refraction index imaginary part, β , to introduce wave amplitude attenuation, while the real part, δ , introduces a phase shift in the wave propagation. By squaring the field amplitude (3.8) we obtain the intensity drop

$$I = I_0 e^{-(4\pi\beta/\lambda)r} \quad (3.9)$$

which shows that the usual linear absorption coefficient of the medium, μ_1 , may be deduced from β by the relation

$$\mu_1 = \frac{4\pi\beta}{\lambda} \quad (3.10)$$

To illustrate the role of this formula, let us consider silicon dioxide (SiO_2) at a photon energy of 100 eV (~ 12 nm wavelength). We have $\beta \simeq 10^{-2}$. Equation (3.10) tells us that radiation intensity is attenuated by a factor of $1/e$ for a covered distance of $1/\mu_1 \simeq 95$ nm, that is to say about 8 wavelengths.

The general properties of XUV reflection are determined by the fact that the refractive index of materials, n , is very close to but slightly less than unity. The small difference between n and 1 makes the reflectance at interfaces between vacuum and materials very small too.

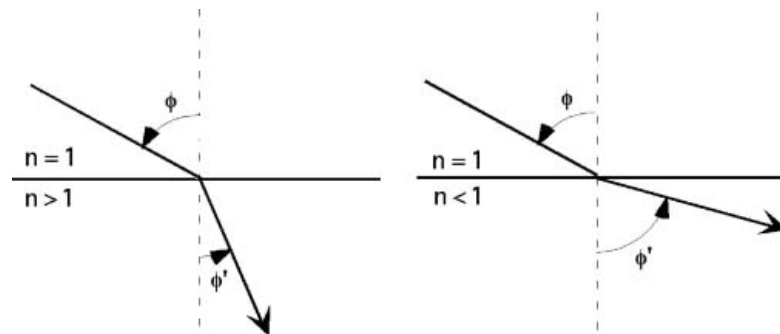


Figure 3.6: Refraction at interface between vacuum ($n = 1$) and material ($n > 1$ or < 1). For XUV radiation $n < 1$ implies $\phi' > \phi$. Thus total reflection occurs from vacuum to material, contrary to reflection of visible light.

At the same time, as illustrated by the sketches of Fig. 3.6, the fact that this difference is negative turns the refracted beam upwards, to separation surface,

instead of turning it downwards, to the normal to the separation surface, as usual in visible optics. The consequence is that an XUV beam flowing in vacuum may undergo total reflection at the vacuum-to-matter interface. In other words, total reflection is an “external” process in XUV region, whereas it is an “internal” process elsewhere. However, it requires a large incidence angle onto the surface, as we will see below. This is why XUV experimentation originated a special kind of optical devices that makes use of grazing incidence on reflecting surfaces.

The reflectance for perpendicular (“*s*” – *senkrecht*) and parallel (“*p*”) polarizations, given by Fresnel’s formula, and written here in terms of the glancing angles, $\theta = \pi/2 - \phi$ and $\theta' = \pi/2 - \phi'$ (see Fig. 3.7), instead of the incidence and reflection angles ϕ and ϕ' , are

$$R_s = \left(\frac{\sin \theta - n \sin \theta'}{\sin \theta + n \sin \theta'} \right)^2 \quad (3.11)$$

and

$$R_p = \left(\frac{n \sin \theta - \sin \theta'}{n \sin \theta + \sin \theta'} \right)^2 \quad (3.12)$$

with

$$\cos \theta = n \cos \theta' \quad (3.13)$$

R_s denotes the reflectance for an electric field vector perpendicular to the incidence plane, R_p denoting the same coefficient for field vectors parallel to the incidence plane.

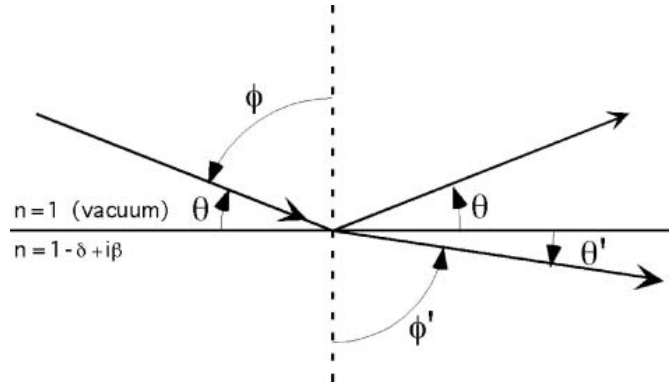


Figure 3.7: Glancing incidence angle (θ) and glancing refraction angle (θ').

External total reflection occurs when

$$\theta' = 0 \quad (3.14)$$

that is to say, from equations (3.13) and (3.4)

$$\cos \theta = 1 - \delta \quad (3.15)$$

where we temporarily assumed $\beta = 0$, as in a fully transparent medium. For small δ 's, the glancing angle at which total reflection will start, i.e. the “critical” angle denoted by θ_c , will be

$$\theta_c = \sqrt{2\delta} \quad (3.16)$$

Fig. 3.8 shows reflectivity versus glancing angle following Parrat’s calculation [32], for four values of β/δ . The upper dashed curve corresponds to $\beta = 0$, for

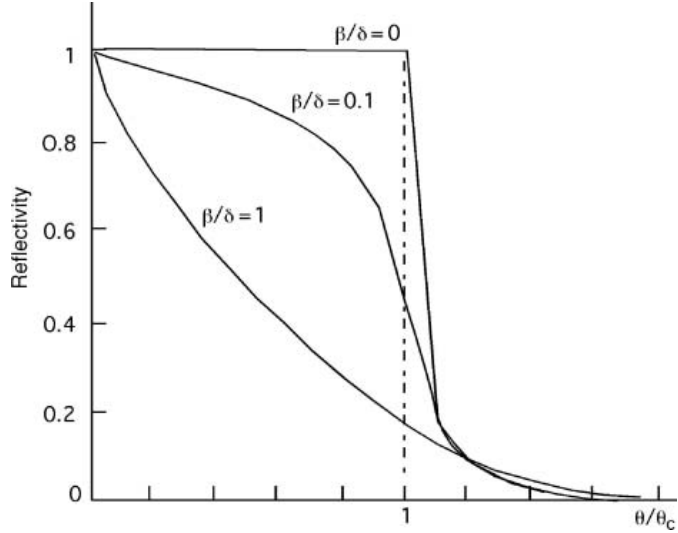


Figure 3.8: Reflectivity versus glancing incidence angle for various values of β/δ (data from Ref. [30]).

which total reflection is achieved for all $\theta < \theta_c$. One sees that for a lossy medium ($\beta = 0$) reflectance also strongly increases for small θ 's, but does not completely reach total reflection.

Detailed study of refracted wave propagation for $\theta < \theta_c$ in lossy media has been performed by Attwood [31] (Chapter 3). This study leads to equations giving the radiation penetration depth, z , into the lossy medium under conditions which would yield total reflection in a transparent medium. In particular

$$z_0 \simeq \frac{\lambda}{2\sqrt{2}}\pi\delta^{1/2} \quad (\theta \ll \theta_c) \quad (3.17)$$

and

$$z_c \simeq \frac{\lambda}{2\pi\beta^{1/2}} \quad (\theta = \theta_c) \quad (3.18)$$

These relations are of importance, not only for a full understanding of XUV reflection properties, but also for estimating the possible damages which may be caused to optical interfaces by intense XUV sources.

Table 3.1: Penetration depth z of 12.4 nm wavelength radiation in silicon dioxide and gold for normal, critical, and strongly sub-critical incidence.

θ	SiO ₂ ($\theta_c \simeq 10^\circ$)		Au ($\theta_c \simeq 23^\circ$)	
	z/λ	z	z/λ	z
$\pi/2$	8.84	109 nm	2.65	32.9 nm
θ_c	1.68	20.8 nm	0.92	11.4 nm
$\ll \theta_c$	0.13	1.6 nm	0.31	3.8 nm

To illustrate the scale of wave penetration under various conditions, Table 3.1 allows us to compare the penetration depths obtained for photons of 100 eV energy ($\lambda = 12.4$ nm) in silicon dioxide ($\delta = 0.014, \beta = 0.009$) and in gold ($\delta = 0.08, \beta = 0.03$) by using equations (3.10) (normal incidence), (3.18) (critical incidence), and (3.17) (extreme grazing incidence).

This comparison between silicon dioxide and gold, chosen for the well-separated positions of their components in the periodic table, as well as for their practical importance in XUV optics, may be extended to their reflectivities. Figures 3.9 and 3.10 display the spectral reflection curves from 30 eV to 500 eV, for $\theta = 5^\circ (< \theta_c)$ in Fig. 3.9 and for $\theta = \theta_c$ in Fig. 3.10. These curves are a good illustration of the behavior of XUV reflectivity discussed in the previous paragraph. In particular, in both cases one sees the reflectivity cutoff near 100 eV at the critical angle $\sim 10^\circ$ for silicon dioxide and $\sim 23^\circ$ for gold.

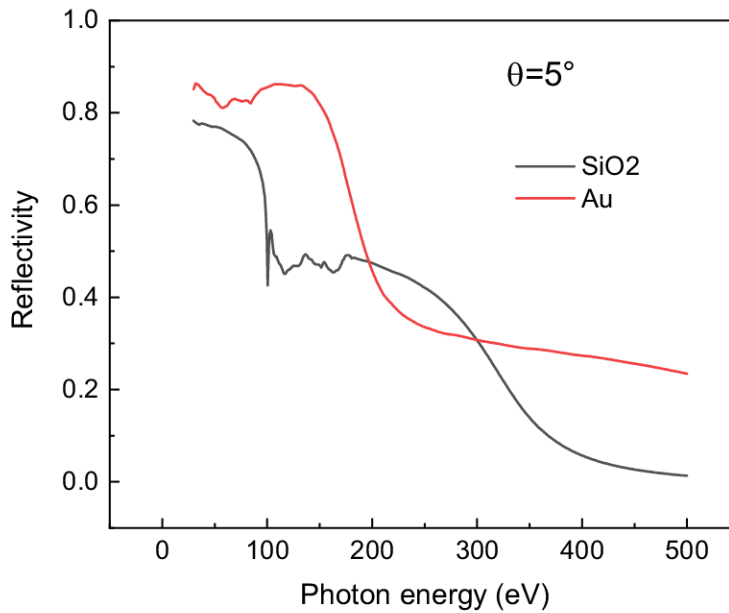


Figure 3.9: Reflectivity of silicon dioxide and gold versus photon energy for the same glancing angle, smaller, in both cases, than the critical angle.

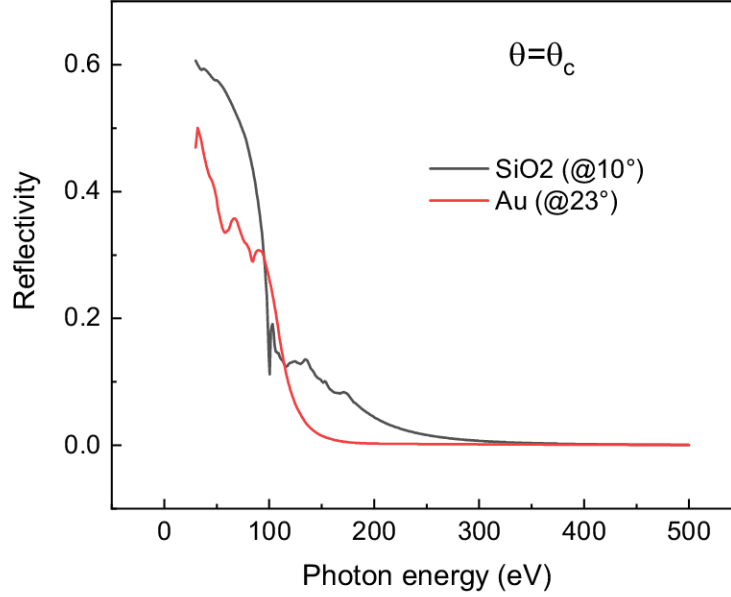


Figure 3.10: Reflectivity of silicon dioxide and gold versus photon energy for the critical incidence angle of each material.

3.2.3 Grazing Incidence Optics

For a long time, reflection under grazing incidence had been the only way to drive radiation propagation in XUV experimental devices. The advent of interferential multilayer mirrors deeply changed the capability, as well as the design, of XUV optical components. However, grazing incidence techniques retain an important part in contemporary experiments, especially as a large bandwidth can be investigated with one and the same device, whereas multilayer reflectors are narrow-band systems. In fact both types of components are used together in many sophisticated arrangements.

Grazing incidence reflection onto plane mirrors does not present any peculiarity except that the size of the mirror in the incidence direction has to be increased by a factor $\sim 1/\sin \theta$, as compared to normal reflection with identical cross-section. Near 10 nm wavelengths the glancing angle can be about 5° , which leads to a lengthening factor about 10. At shorter wavelengths, with glancing angles of 1° or less, the lengthening factor becomes larger than 50, which may lead to technical issues. Moreover mirror's polishing must be of especially high quality in order to reduce XUV radiation scattering on the surface ruggedness.

The peculiarity of grazing incidence optics mainly lies in the exceptionally strong astigmatism of spherical reflectors. This is schematically illustrated in Fig. 3.11, which represents a spherical mirror M of curvature center C , with the incident light coming from the source point A , under the glancing angle θ . As is well known, the beam will not converge toward some well-defined image point after reflection, but it rests on two “astigmatism focal lines”, S , in the incidence plane, and T perpendicular to this plane. Let us choose the origin of the distances at the mirror center, M , and call S (resp. T) the point of intersection of the focal line S (resp. T) and the central reflected ray. The positive direction being the direction of light, the positions of S and T are calculated from the next expressions

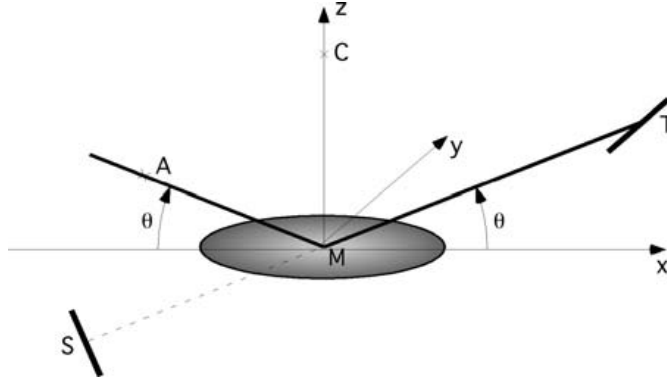


Figure 3.11: Grazing incidence astigmatism of a concave mirror. The reflected beam is supported by two small straight lines, one of them, S , being generally virtual as shown in the figure.

respectively:

$$\frac{1}{MS} = \frac{1}{MA} + \frac{2 \sin \theta}{R} \quad (3.19)$$

$$\frac{1}{MT} = \frac{1}{MA} + \frac{2}{R \sin \theta} \quad (3.20)$$

where R is the radius of the mirror. The conditions for the focal lines to be real, namely to lie in the image space, are $MS > 0$ and $MT > 0$. From equations (3.19) and (3.20) one can see that S is real if

$$|MA| > \frac{R}{2 \sin \theta} \quad (3.21)$$

and T is real if

$$|MA| > \frac{R \sin \theta}{2} \quad (3.22)$$

Since θ is a small angle, the first of these two conditions is fulfilled only for remote sources. Therefore, for grazing incidence experimental arrangements, one generally gets to use the tangential focal line T to yield radiation concentration into a “focal” spot.

To achieve better focalization, one may replace the spherical mirror by a toroidal one, so as to adjust MS and MT by using two different curvature radii in equations (3.19) and (3.20) [33]. One immediately see that the points S and T will merge when the ratio of radii takes the value $\sin^2 \theta$. However, it is clear that this is practicable only if the glancing angle is not too small.

In many applications of XUV optics, it is found convenient that A , the point source, and its “image” T be symmetrical with respect to the normal to the mirror, in order to minimize aberrations. If we substitute $MT = -MA$ in Eq. (3.20), we obtain $|MA| = R \sin \theta$. This means that the required symmetry does exist for a set of points A , which forms a circle of radius $R/2$, tangent at M to the mirror. This circle, represented in Fig. 3.12, is known as the Rowland circle of the spherical mirror. The image of a source located at the curvature center of the mirror (point C in Fig. 3.12) is perfectly stigmatic.

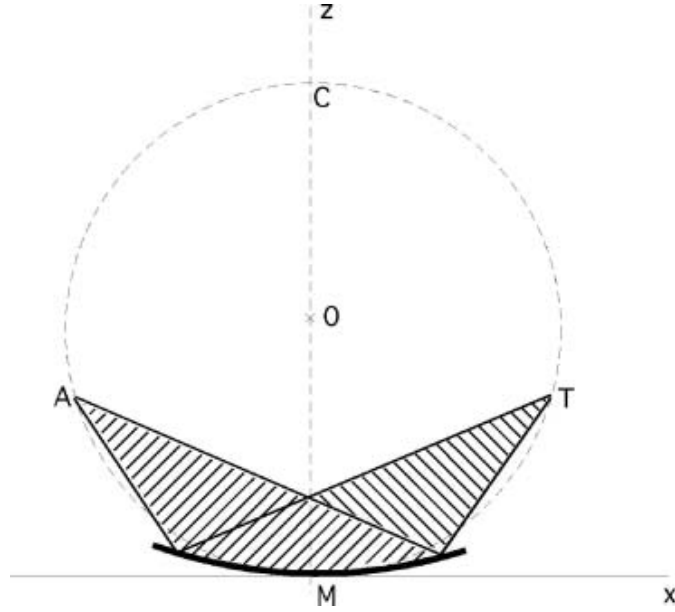


Figure 3.12: Rowland circle of a concave mirror. C is the curvature center of the mirror. The diameter of the Rowland circle equals the radius of the mirror.

When working in grazing incidence, the Rowland circle remains the location of source points which minimizes optical aberrations. This property and the practical advantages of a simple geometry explain why the Rowland circle mountings have been largely used in XUV spectroscopic devices.

3.3 Reflection polarimeter

The main activity carried on during my three-year Ph.D. has been the design and the development of a reflection polarimeter/polarizer to be used in the XUV spectral range.

The aim was to develop a device which can be used either to polarize incoming light or to measure the polarization state of the radiation. It should be possible to insert and remove the device into/from the beam without affecting the direction of the rays [34–36].

The idea is to exploit the polarization change that incoming radiation undergoes after reflection off a metallic surface. In particular, the difference between the parallel (R_p) and the perpendicular (R_s) reflectance is what causes the light to modify its polarization state [37].

With only one reflection we get a change in polarization with the disadvantage of deviating the beam from its original path. Instead, by employing 3 consecutive reflections we enhance the polarizing effect and, at the same time, we are able to align the output beam with the optical axis, leaving the overall direction unaltered. The proposed design is represented in Fig. 3.13. As can be seen, this geometry requires that the glancing angle of the central mirror be twice that of the outer mirrors. An angle of 10° has been chosen for the outer mirrors, leading to 20° for the glancing angle of the central one. These angles represent the best compromise between throughput of the device and contrast; the former being the fraction of the incoming light that exits the device, while the latter is a measure of the difference

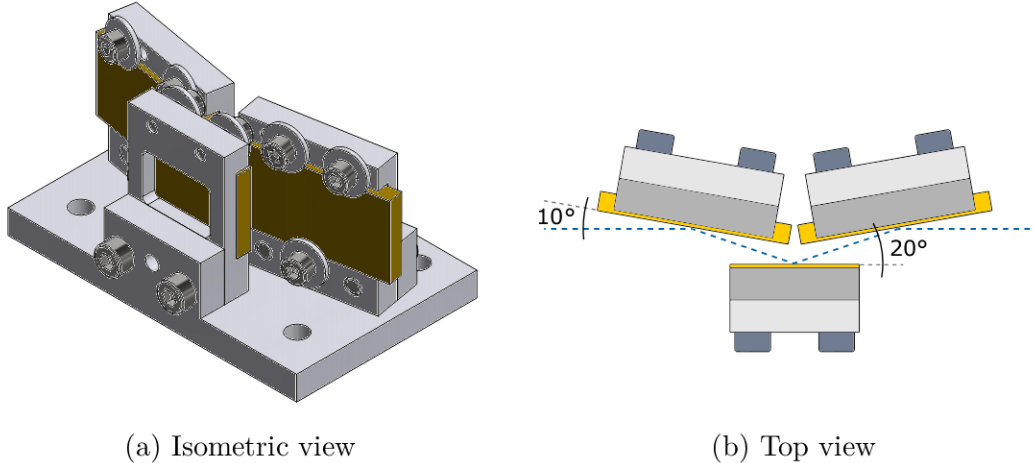


Figure 3.13: CAD model of the 3-mirror reflection polarizer.

between the two involved reflectances. It is defined as

$$C = \frac{R_s - R_p}{R_s + R_p} \quad (3.23)$$

where R_s is the reflectance (ratio of outgoing and incoming light intensities) for the electric field perpendicular to the incidence plane, while R_p is the reflectance for the parallel one. From Fresnel's equations (see Section 3.6.2) we get that $R_s \geq R_p$. They coincide only in two cases: for an incidence angle of 0° (normal incidence), in which the propagation plane is parallel to the reflecting surface and thus distinguishing between s and p makes no sense (for an isotropic material), or 90° (extreme grazing incidence), where they both tend to unity.

By choosing very grazing (small) working angles we increase the overall reflectivity and therefore the throughput of the device, with the downside of reducing the difference between R_s and R_p , thus lowering the contrast. A high contrast is typically needed in a polarimeter in order to maximise the response to polarized light and to effectively characterize the polarization state. If, on the other hand, higher grazing angles are chosen, the contrast is enhanced at the expense of low reflectivities and thus a small throughput of the overall system.

3.3.1 Mirrors

In the XUV spectral range, and especially at grazing working angles, the radiation interacts only with a very thin superficial layer of the material, before being completely absorbed. For this reason, typical XUV optics is made of a bulk substrate, like glass, on top of which there is a thin coating of a specific material of choice, which depends on the required functionality. Some applications require low reflection (anti-reflective coatings), some want the opposite, and others need only a narrow bandwidth response.

We chose to order from a silicon wafer producer some rectangular silicon plates, which would act as the substrate for a subsequent metallic-coating deposition. The central mirror would have a dimension of (20×15) mm while the outer ones would be (30×15) mm. This is because of the fact that the central mirror works at a

higher glancing angle than the outer ones, meaning that the illuminated area on the mirror surface is smaller.

In the first version of the polarimeter we ordered rectangular plates with a thickness of 3 mm, made of poly-crystalline silicon, polished on one side. We soon realized that the poly-crystalline nature of the silicon was visible with the naked eye, in the form of many different domains, or *grains*, bounded by the so-called *grain boundaries*, which are the interfaces where crystals of different orientations meet. This macroscopic structure would have had effect on the subsequent coating deposition and for this reason we chose not to proceed and to switch to mono-crystalline silicon.

Grain-boundaries were no more visible with the mono-Si plates and therefore we ordered the deposition of a 50 nm-thick layer of gold. One of the first measures that was conducted was an AFM (Atomic Force Microscopy) analysis, which is useful to evaluate the surface quality of a sample. It turned out that the surface roughness of the gold-coated mono-Si plates was in the order of ~ 2 nm, which is relatively high for a XUV application. The same analysis was performed on the uncoated mono-Si samples and the same surface roughness was found. The problem was soon identified by the silicon manufacturer: the 3 mm thickness we ordered was not a “standard” product, therefore it could not guarantee the same smoothness of the thinner, more standard, wafers.

In the end, we opted for mono-crystalline silicon plates cut out from a standard 0.7 mm-thick wafer, polished on one side. The measured roughness in this case was ~ 0.2 nm, which is sufficiently low to avoid surface scattering. We thus proceeded with the deposition of Au and Ru.

With the reduced thickness of the substrate, the mirror holders had to be redesigned. In the first design, a single mirror was held in position by inserting it into a 3 mm notch, with the non-polished side down. Nylon washers were gently pushing the front-side, keeping the mirror in place. By using the very same setup for the thinner mirrors, it was noticed that a light beam travelling through the device would experience a focusing effect on the tangential plane, at a distance of several meters after the last mirror. The cause for this effect were the washers. With a mirror thickness of only 0.7 mm, even the moderate, but localized, pressure applied by the washers was sufficient to deform the mirrors, inducing a concave shape which, in turn, causes light to be focused.

For this reason, a new design for the mirror holders was needed. The notch depth was reduced to 0.7 mm, in order to accommodate the mirror. On the front-side a thin PTFE (Teflon) stripe pushes against the reflecting surface. By using a long stripe, the load is distributed and deformation of the surface are prevented. Teflon is a thermoplastic polymer, which is flexible and does not scratch the delicate reflecting surface. Moreover, it is highly hydrophobic: neither water nor water-containing substances wet PTFE, making it an ideal insulating and structural material in high-vacuum environments. In Fig. 3.14 the first and the new design are shown.

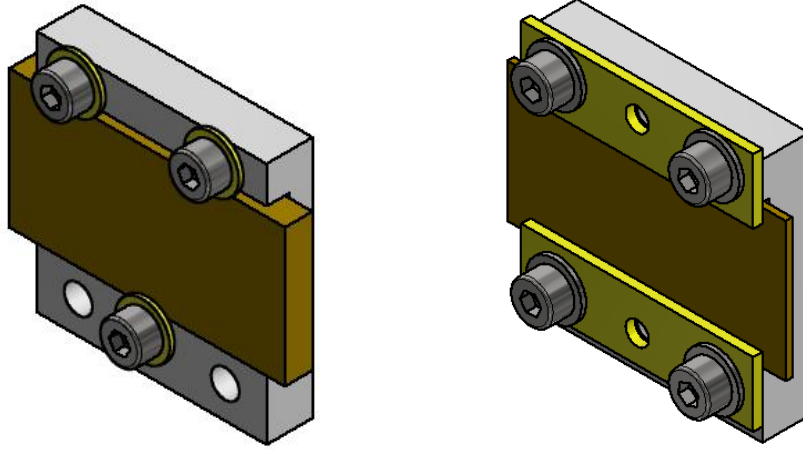


Figure 3.14: (Left) First design of the mirror holder; the three washers (in yellow) are visible. (Right) Improved design; two long Teflon stripes are holding the thin mirror.

3.3.2 First polarimeter design

In order to analyze the polarization state of the incoming light, the polarimeter (the 3-mirror device described above) needs to be rotated about the optical axis, which has to coincide with the beam path. Indeed, when the device is perfectly aligned, the light ray reflected by the last mirror lies exactly on top of the axis defined by the input beam, and it should be possible to rotate the 3 mirrors about the beam-axis without seeing any displacement on the output.

In order to rotate the polarimeter we employed a rotation stage, which is typically made of a stepper motor that, through a gear reduction mechanism, drives a rotating platform. The platform should have a through-hole, so that it can be inserted into the beam. The rotation stage should be mounted and aligned so that the rotation axis of the platform coincides with the beam-axis. Moreover, the polarimeter device has to be fixed onto the platform in a way that the light passes through the platform hole and hits the center of the first mirror. If all the axes (3-mirror device, rotating platform, and beam) are made to be coincident, the rotation of the stage should not cause any visible displacement of the spot on the image plane.

The fine alignment needed between the polarimeter and the rotation stage suggested us the use of a 4-axis tilt-aligner, which is a kinematic device that offers a base with 4 degrees of freedom, 2 linear and 2 angular ones. The device is provided by Newport. It is mounted on top of a bracket which, in turn, is fixed onto the rotating platform. On top of the tilt-aligner we mounted the mirror-stage. In Fig. 3.15 a schematic 3D model of the whole system is presented. The radiation is identified by the positive z -direction, and it is coincident with the blue dashed line, which is observed to pass through the rotation stage, hit the first mirror (at 10° glancing angle), then the second (at 20°), and leave the device after the third reflection. The Newport tilt-aligner provides all the necessary degrees of freedom to align the mirror-stage with the rotation stage: X, Y (linear motion along x and y , respectively) and θ_x, θ_y (rotation about x and y , respectively).

In the next section I will discuss about the setup that is needed to perform the

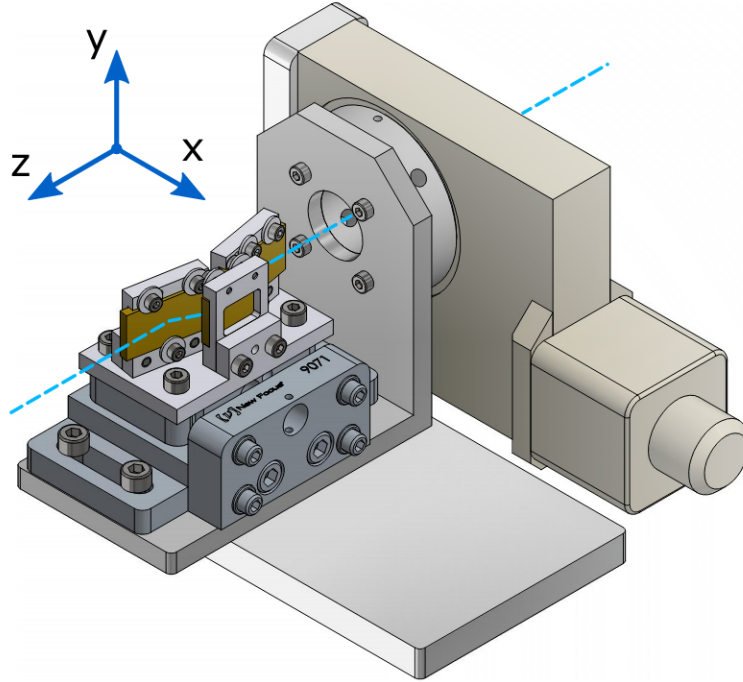


Figure 3.15: CAD model of the first design of the polarimeter stage. The optical axis is represented by the blue dashed line.

experiment, including the electronic equipment and the control software that has been developed.

3.3.3 Rotation stage

As explained briefly before, the rotation stage is driven by a stepper motor which, by rotating in fixed increments (or steps), enables a precise rotation of the platform.

Stepper motors effectively have multiple “toothed” electromagnets arranged as a stator around a central rotor, a gear-shaped piece of iron. The electromagnets are energized by an external driver circuit or a microcontroller. To make the motor shaft turn, first, one electromagnet is given power, which magnetically attracts the gear’s teeth. When the gear’s teeth are aligned to the first electromagnet, they are slightly offset from the next electromagnet. This means that when the next electromagnet is turned on and the first is turned off, the gear rotates slightly to align with the next one. From there the process is repeated. Each of those rotations is called a *step*, with an integer number of steps making a full rotation. In that way, the motor can be turned by a precise angle.

In particular, our rotation stage is equipped with a bipolar (one single winding per phase) 4-wire stepper motor. This means there are two windings, or phases, and the current in a winding needs to be reversed in order to reverse a magnetic pole. A schematic representation of a two-phase bipolar stepper motor is pictured in Fig. 3.16.

A typical driving pattern for a two coil bipolar stepper motor would be: A , B , \bar{A} , \bar{B} , meaning: drive coil A with positive current, then remove current from coil A ; then drive coil B with positive current, then remove current from coil B ;

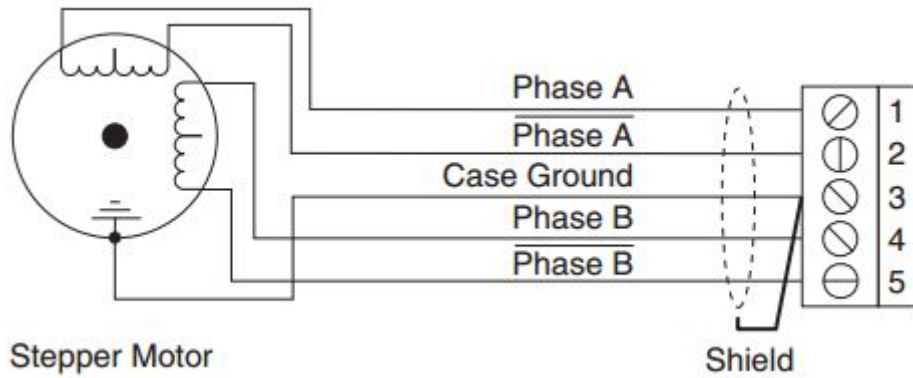


Figure 3.16: 4-wire stepper motor showing the 2 windings and the phase outputs.

then drive coil A with negative current (flipping polarity by switching the wires e.g. with an H-bridge), then remove current from coil A ; then drive coil B with negative current (again flipping polarity same as coil A); the cycle is complete and can be repeated again.

Our stepper motor has a pitch (angular movement corresponding to one step) of 1.8° , meaning that it needs $360^\circ/1.8^\circ = 200$ steps to complete one full turn. The rotating platform is driven via a worm drive with a gear reduction of 360, therefore $200 \times 360 = 72\,000$ steps are needed to rotate the platform by a full turn. Accordingly, the angular resolution of the rotation platform is $360^\circ/72\,000 = 0.005^\circ$, that is the angle by which the platform is rotated after one step of the motor.

Instead of driving the single coils and taking care of flipping the polarity, we opted for a stepper motor driver: the Texas Instruments' DRV8825 board. It provides an integrated and cheap solution, offering two H-bridge drivers and a micro-stepping indexer, and is intended to drive a bipolar stepper motor. The output driver block consists of N-channel power MOSFETs configured as full H-bridges to drive the motor windings.

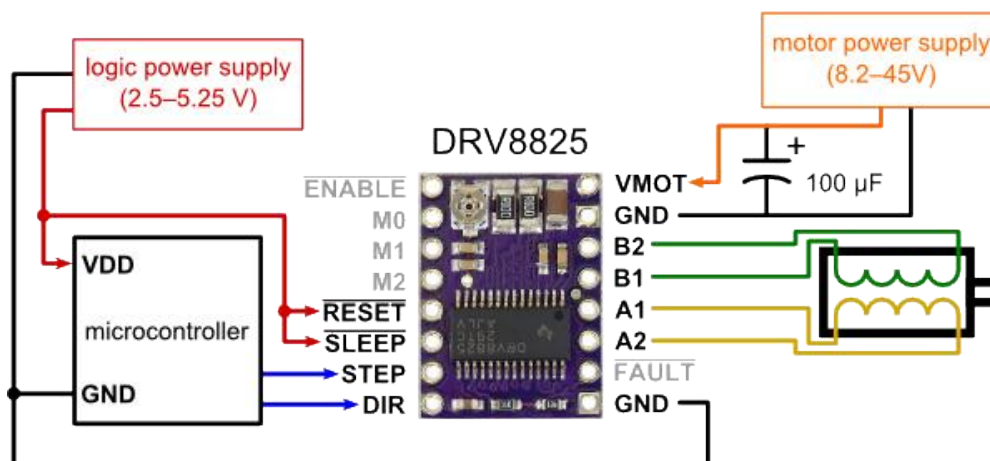


Figure 3.17: Wiring diagram for connecting the stepper motor driver to a microcontroller.

The driver is connected to a microcontroller by means of the “STEP” and the

“DIR” pins. Each pulse to the STEP input corresponds to one step of the stepper motor in the direction selected by the DIR pin.

In order to develop a cost-efficient solution, we decided to control the stepper-motor driver with an Arduino Nano, a small, complete, and breadboard-friendly board based on the ATmega328, a single-chip microcontroller created by Atmel. The Arduino acts as the interface between the driver and the user interface, i.e. the software with which the user can interact and that is used to send the appropriate commands to the microcontroller. More generally, the software is used to control the whole experimental setup, from moving the rotation stage to record and save polarimetric data, and it will be described more in detail in a later section.

Two digital outputs of the Arduino are connected to the STEP/DIR pins, which enable the step-wise rotation of the motor. In order to rotate the motor by a certain angle, the microcontroller sends a train of n pulses to the STEP pin, where the number of pulses determines the number of steps (n), and the time interval between a pulse and the next one defines the speed of rotation. By knowing the step/angle conversion ratio (1 step = 0.005° , or $1^\circ = 200$ steps), the Arduino firmware is able to convert an angle, input by the user, to an appropriate train of pulses. The speed of the motor, namely the time period between two consecutive pulses, can be changed with the control software.

On the rotation stage there is a limit-switch which is activated by a dowel pin on the rotation platform. This mechanism is used to “home” the motor, i.e. to set a reference point, also called the *zero* position of the rotation stage. The two leads of the limit-switch are therefore wired to the digital input pins of the microcontroller.

The Arduino board is connected to a PC through a USB cable, and thereby all communications between the microcontroller and the control software happen by means of a serial transmission protocol.

3.3.4 Photodiode

The whole polarimeter stage, as depicted in Fig. 3.15, is positioned inside an experimental vacuum chamber, where the XUV radiation can propagate without being absorbed by air. After passing through the mirror-stage, the radiation has to be detected by an appropriate sensor, which is placed immediately after the mirrors.

The sensor that was chosen is a XUV silicon photodiode, namely the AXUV100 manufactured and provided by Opto Diode. It features a large, square detection area of 100 mm^2 . A photodiode is a semiconductor p-n junction device that converts light into an electrical current, which is generated when photons are absorbed in the photodiode. When these diodes are exposed to photons of energy greater than 1.12 eV (wavelength less than 1100 nm) electron-hole pairs (carriers) are created. These photogenerated carriers are separated by the p-n junction electric field and a current proportional to the number of electron-hole pairs created flows through an external circuit.

A silicon XUV photodiode has several advantages over the classical tube-type XUV detectors. A photodiode exhibits very low noise, does not need external voltages for its operation, is insensitive to magnetic fields, costs less to fabricate, has low mass, has a large collection area to size ratio, and is more (spatially)

uniform.

A coaxial cable connects the sensor to an external picoammeter, which is able to read the photogenerated current both in low-light or room-light conditions. In the latter case, our photodiode produces an output current of tens to hundreds of microampere depending on the light intensity. In Fig. 3.18 the response curve of the sensor in the UV/XUV spectral region is shown.

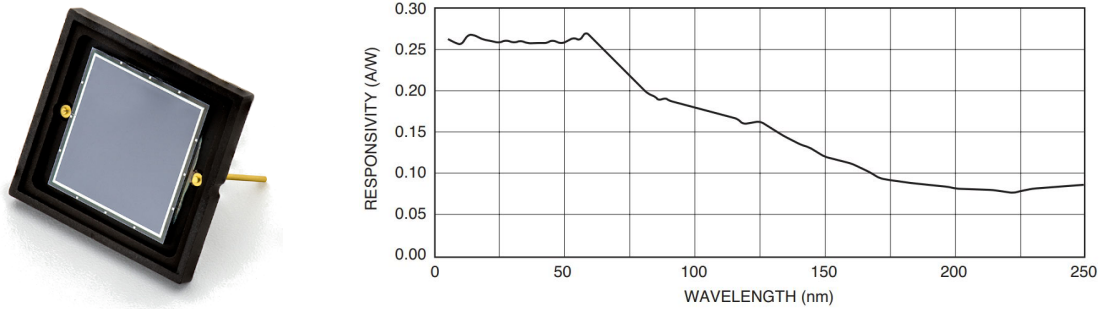


Figure 3.18: (Left) Front view of the AXUV100 photodiode. (Right) UV/XUV photon response of the sensor, from 5 nm to 250 nm wavelength.

The sensor is fixed onto an aluminum holder, clamped on the four sides by Teflon strips. The holder, in turn, is mounted on a push-pull linear translation stage which travels perpendicular to the beam axis and thus enables the insertion/removal of the photodiode into/from the beam.

3.3.5 Reference signal

During a polarimetric/ellipsometric experiment, the light intensity after the mirror stage is typically recorded as a function of the rotation angle of the polarimeter. If a 360° rotation is required, there is a certain time delay between the first and the last acquired intensity measurements. If, during that time interval, the radiation source is not constant, i.e. its intensity fluctuates and/or drifts, the acquired signal is affected too, meaning that possible variations seen in the acquired signal cannot be entirely ascribed to the physical property under investigation, e.g. the polarization of the source or the ellipsometric response of a sample. For this reason, a signal that tracks the source intensity is needed.

Most of the experiments conducted with the polarimeter stage have been performed at the synchrotron facility “Elettra”, in Trieste, in particular on the “CiPo” (Circular Polarization) beamline. More details about the unique properties of synchrotron radiation and the features of CiPo will be given in Section 3.4.

On a synchrotron beamline we typically have access to a signal coming from the last refocusing optical element, which is a mirror that takes the radiation coming from the monochromator and focuses it onto the sample point in the experimental chamber. The signal is generated by exploiting the photoelectric effect that happens when photons hit the metallic coating of the mirror and electrons, now called *photoelectrons*, are emitted. These electrons are collected by a metallic grid applied on the mirror and therefore an electric current can be measured. For a given photon energy, this signal is proportional to the flux of photons hitting the mirror and thus it can be used as a reference signal in order to normalize the experimental data measurements. In particular, in the post-processing phase

the detected light intensity is divided by the reference current, compensating for fluctuations and drifts of the synchrotron source.

3.3.6 Control software

The software for controlling the experimental setup has been developed in LabVIEW, a graphical programming platform typically employed in data acquisition, instrument control, and industrial automation systems. LabVIEW integrates the creation of user interfaces (termed front panels) into the development cycle. The graphical approach allows to build programs by dragging and dropping virtual representations of lab equipment, sub-routines, functions and so-called *nodes*.

The software has been designed with the intention of controlling the whole instrumental setup and, more importantly, to enable automatic polarimetric experiments.

The front panel, i.e. the user interface, is divided in two different tabs. The first one provides all the commands and controls to *manually* interact with the rotation stage and the two picoammeters (one reads the current from the XUV photodiode, the other reads the reference signal coming from the refocusing mirror). The panel allows the user to send commands to the Arduino, which, in turn, sends the appropriate signals to the board that drives the stepper-motor of the rotation stage. It is possible to move the motor by an incremental angle or move it to an absolute position, the motor can also be “homed”, meaning that it rotates until the limit switch is found, or it can be “zeroed”, i.e. the current position is taken as the new zero.

On the same tab, there are two waveform panels, one for each picoammeter. From here it is possible to change the scale range and to activate a moving-average filter, for each instrument. Moreover, a real-time acquisition can be started, meaning that the electric current signals from the picoammeters are plotted in real-time on the waveform panels.

The second tab is dedicated to the automatic polarimetric measurements. During an automatic experiment the mirror-stage rotates about the optical axis while the XUV intensity and the reference signal are recorded, as a function of the polarimeter angle. From the front panel it is possible to set a starting angle, a final angle and the angle step by which the rotation stage should be moved. In addition, the number of measurements per angle can be set, that is, for each angular position of the stage, a certain number of measurements are recorded and saved. This is done to ensure repeatability of the measurements and later, in the post-processing phase, these data points can be averaged in order to obtain a single intensity value per angle.

Applications in LabVIEW are usually designed using well-known architectures, known as design patterns. I decided to employ the so-called “queued message handler” (QMH), a design pattern with the aim of producing a highly responsive user interface for multithreaded applications.

The QMH template facilitates multiple sections of code running in parallel and sending data between them. Each section of code represents a task (e.g. acquiring data, logging data, user events) and is designed similarly to a state machine. Because of this design, it is possible to divide each task into states. This design pattern is geared towards enhanced data sharing between multiple loops running

at different rates. Its parallel loops are broken down into two categories: those that produce data, and those that consume the data produced. The interaction between the loops happens through queues, or buffers. When there are multiple processes running at different speeds, buffered communication between processes is extremely effective. With a large enough buffer, the producer loop can run at much higher speeds than the consumer loop without data loss. An example of a queued message handler, which is based on the simpler Producer-Consumer design pattern, is shown in Fig. 3.19.

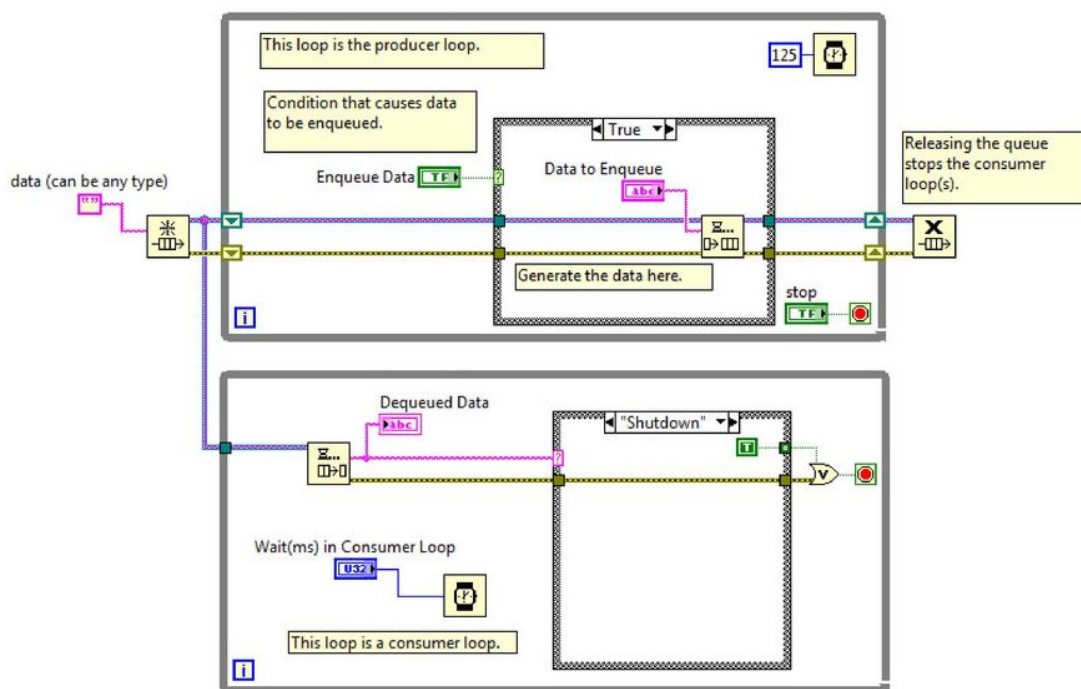


Figure 3.19: Block diagram (graphical source code) of a typical queued message handler.

In our case, the *producer* is the loop that takes care of receiving both the messages coming from the microcontroller and the user inputs coming from the front panel. These messages are promptly interpreted and inserted into the communication buffer (a LabVIEW *queue*). A second, parallel, loop dequeues (extracts) the messages from the buffer and performs the appropriate action. A third loop is used to handle the real-time acquisition from the two picoammeters.

3.3.7 New polarimeter design

During the course of several beamtimes on the synchrotron in Trieste, we realized that the design of the polarimeter assembly was not ideal for an efficient alignment. The lack of fine regulations on the base support of the polarimeter stage proved to be very disadvantageous, as the whole alignment process had to be carried out by hand, moving the whole structure. Something similar to the 4-axis tilt-aligner was needed also for the adjustment of the whole mechanical structure.

For this reason, several modifications and improvements have been implemented in the mechanical structure of the polarimeter. A more compact rotation stage has been adopted, and a kinematic alignment platform has been mounted

at the base of the polarimeter, in order to provide a fine alignment of the system. Considering the high surface roughness of the 3 mm-thick silicon substrates as seen in the previous beamtime, we switched to 0.7 mm thin mirrors, which guarantee sub-nanometer surface roughness. In addition, we added a tip-tilt manual aligner on the last mirror, which proved essential for the precise alignment of the polarimeter stage. The new design of the system is depicted in Fig. 3.20, where the polarimeter is shown in two different positions, at 0° and at 60° rotation.

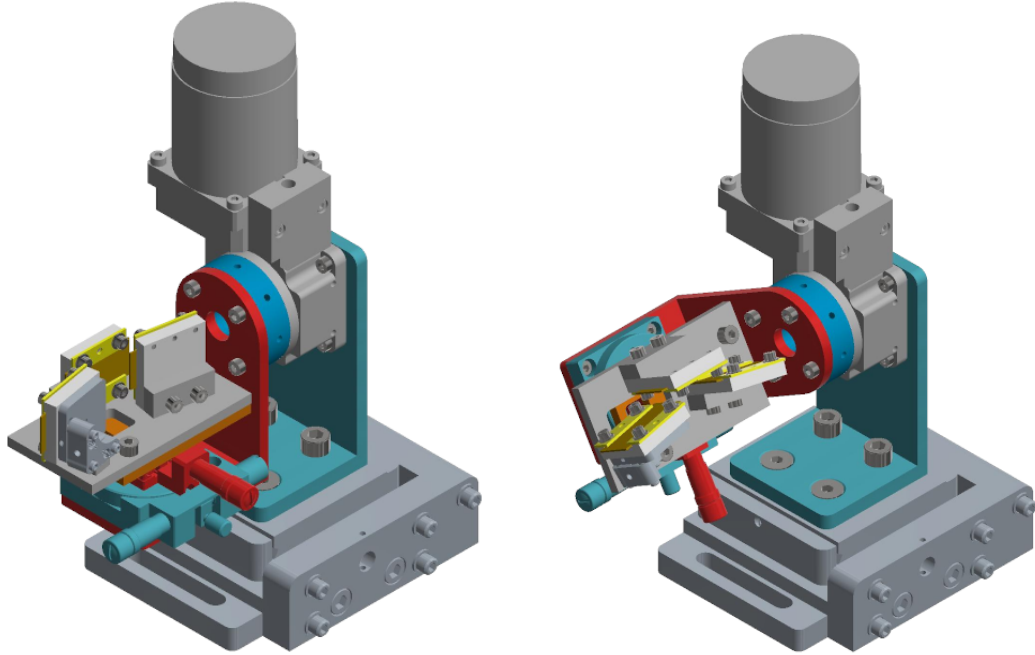


Figure 3.20: CAD model of the improved design of the polarimeter assembly, shown at two different angles: $\alpha = 0^\circ$ (left) and $\alpha = 60^\circ$ (right).

The new design allowed for a precise (manual) alignment of the system, though a perfect alignment of the mirror-stage was very difficult to achieve. This is ascribed to the slight misalignment of the visible (zero-order) radiation of the source with respect to the XUV beam. With the manual stage, one has to work in “air”, leaving the experimental chamber open, and the alignment process has to be performed by using the visible radiation provided by the beamline, in order to be able to look at the output spot (after the three reflections) and check for probable movements and displacements as the polarimeter is rotated about the optical axis. After the alignment of the stage with respect to the visible beam, the chamber is put in high-vacuum and the XUV beam is sent into the chamber. Ideally, the visible and the XUV beams should be perfectly collinear, but in practice a slight misalignment is observed. However, once the chamber is in vacuum it is not possible to adjust the position of the polarimeter, and the experiment proceeds with a non-optimal alignment.

Eventually, we decided to employ a motorized vacuum stage so that a fine alignment (in vacuum) between the whole polarimeter stage and the XUV beam-axis becomes more feasible. The new motorized alignment platform is mounted at the base of the polarimeter, as seen in Fig. 3.21.

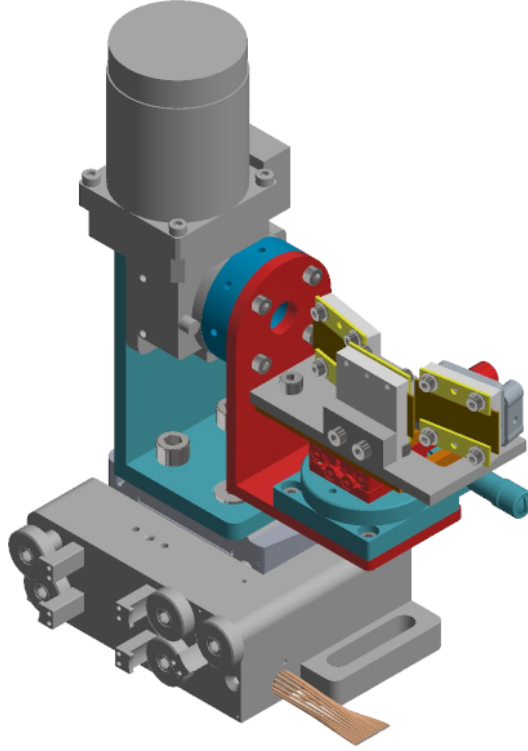


Figure 3.21: CAD model of the newest design of the mechanical structure of the polarimeter assembly, showing the motorized alignment platform at the base.

3.4 CiPo beamline

In order to test the polarimeter in the extreme-ultraviolet, using a broad range of photon energies, it has been necessary to exploit the unique properties of synchrotron radiation.

A synchrotron is a particular type of cyclic particle accelerator, descended from the cyclotron, in which the accelerating electron beam travels around a fixed closed-loop path. The magnetic field which bends the electrons into a closed path increases with time during the accelerating process, being synchronized to the increasing kinetic energy of the particles. When charged particles are accelerated radially, i.e. when they are subject to an acceleration perpendicular to their velocity ($a \perp v$), electromagnetic radiation is emitted, it is called synchrotron radiation or magnetobremstrahlung radiation. This radiation is produced when moving particles accelerate, and this is the case when electrons move freely in a magnetic field. This is similar to a radio antenna, but with the difference that, in theory, the relativistic speed will change the observed frequency due to the Doppler effect by the Lorentz factor γ . Relativistic length contraction then bumps the observed frequency by another factor of γ , thus multiplying the gigahertz frequency of the resonant cavity that accelerates the electrons into the X-ray range. The radiated power is given by the relativistic Larmor formula, while the force on the emitting electron is given by the Abraham–Lorentz–Dirac force. The radiation pattern can be distorted from an isotropic dipole pattern into an extremely forward-pointing cone of radiation. The planar acceleration geometry appears to make the radiation linearly polarized when observed in the orbital plane, and circularly polarized

when observed at a small angle to that plane [38].

The main properties of synchrotron radiation are:

- Broad spectrum (from microwaves to hard X-rays): the users can select the wavelength required for their experiment;
- High flux: high-intensity photon beam allows rapid experiments or use of weakly scattering crystals;
- High brilliance: highly collimated photon beam generated by a small divergence and small-size source (spatial coherence);
- High stability: sub-micrometer source stability;
- Polarization: both linear and circular;
- Pulsed time structure: pulsed duration down to tens of picoseconds allows the resolution of process on the same time scale.



Figure 3.22: General diagram of Synchrotron Soleil. The electrons are accelerated by electric fields in the straight sections between green squares. The red rectangles are magnets that bend the beam. When the beam is bent the electrons emit synchrotron radiation (shown in yellow), especially X-rays; these are sent into the various beamlines (the straight lines branching out of the synchrotron). Each beamline contains scientific instruments, experiments etc. and receives an intense beam of radiation.

The synchrotron radiation is projected at a tangent to the electron storage ring and captured by the so-called *beamlines*. These beamlines may originate at bending magnets, which mark the corners of the storage ring; or insertion devices, which are located in the straight sections of the storage ring. The beamline includes X-ray optical devices which control the bandwidth, photon flux, beam dimensions, focus, and collimation of the rays. The optical devices include slits, attenuators, monochromators, and mirrors. The mirrors may be bent into curves or toroidal shapes to focus the beam. A high photon flux in a small area is

the most common requirement of a beamline. The design of the beamline will vary with the application. At the end of the beamline is the experimental end-station, where samples are placed in the line of the radiation, and detectors are positioned to measure the resulting diffraction, scattering or secondary radiation. A representation of the Soleil synchrotron facility, near Paris, France, is shown in Fig. 3.22.

All the experiments with the polarimeter setup have been performed at the “Circular Polarization” (CiPo) beamline. CiPo is primarily characterized by its capability of providing a synchrotron radiation beam of variable polarization (Circular to Linear) in a very broad range of photon energies, 5 eV to 900 eV. The photon beam is produced by an Electromagnetic Elliptical Wiggler (EEW) and is dispersed by means of two collinear monochromators, a Normal Incidence Monochromator (NIM) and a Spherical Grating Monochromator (SGM), that alternatively provide two beams in the UV/XUV (5 eV to 40 eV) and soft X-rays (40 eV to 900 eV) respectively.

The EEW was designed to provide linearly and circularly polarized radiation over a wide range of photon energies, using both undulator and wiggler modes of operation. The request for helicity switching led to a fully electromagnetic design which combines the horizontal and vertical periodic magnets into one open-side structure. Under wiggler conditions the EEW operates for different values of the vertical and horizontal magnetic field providing an elliptically polarized radiation and a continuum soft x-ray emission spectrum extending from 40 eV to 900 eV. In addition to the continuum, the EEW emits a spectrum of harmonics in the low photon energy side (<40 eV), whose fundamental energy is at 4.5 eV. The degree of circular polarization changes with photon energy in the range from 40% at 8.5 eV to 80% at 575 eV. Full circular polarization condition (90%) is achieved when the EEW works as a pure circular undulator, i.e. when the horizontal and vertical magnetic fields are equal. Under these conditions the available first harmonic lies in the photon energy range between 50 eV to 150 eV. The undulator mode allows to produce also linearly polarized radiation with the polarization vector either parallel or perpendicular to the orbit plane. In fact, by switching off the horizontal magnetic field, linearly polarized radiation parallel to the orbit plane is produced, while switching off the vertical coils causes the remaining field to drive the stored electrons and to oscillate in the direction perpendicular to the orbit plane, emitting vertical linearly polarized radiation.

The availability of such a wide photon energy spectrum, together with the polarization selection, makes the CiPo beamline extremely flexible for our experimental activity.

The beamline consists of two different monochromators (NIM and SGM, i.e. G' and G respectively), which share the entrance and exit slits (S1 and S2) as well as the pre- and post-focusing optics (M0, M1 and M3), as sketched in Fig. 3.23. The normal incidence monochromator (NIM, i.e. G'), covers the photon energy range of 5–35 eV using two different holographic gratings (gold and aluminum). The grazing incidence monochromator (SGM, i.e. G), covers the energy range 30–1000 eV, working in Padmore-type configuration and is equipped with a variable angle plane mirror (M2) and four spherical gratings (G1 to G4). Switching between the two monochromators is obtained by simply inserting or removing one mirror (M'2). The beamline accepts a maximum emission angle of 2×1 mrad² of the

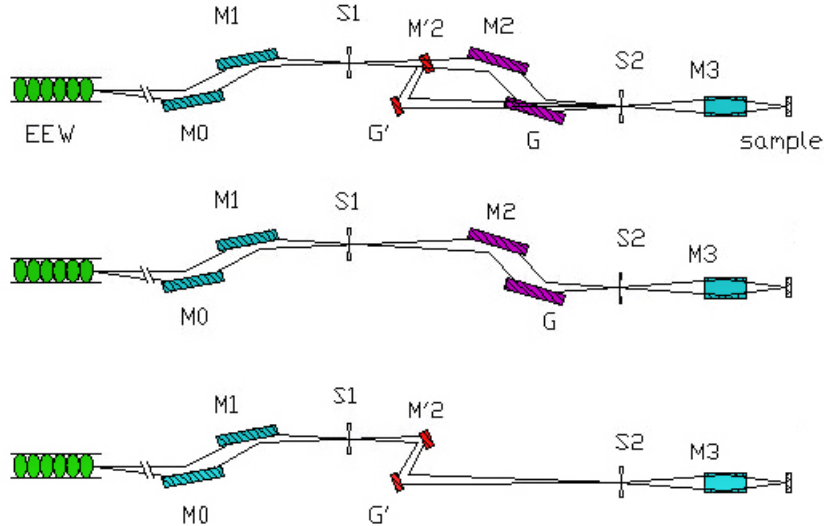


Figure 3.23: Schematic representation of the CiPo beamline. The middle drawing represents the grazing incidence configuration, while the one on the bottom is the normal incidence case.

radiation that is focused in the vertical plane by means of plane (M0) and toroidal (M1) mirrors onto the entrance slit (S1). Both mirrors of the focusing optics have 2.5° grazing incidence and return the radiation parallel to the orbit plane. After the exit slit (S2) the radiation is focused at the sample position with a toroidal mirror (M3).

The last mirror (M3) is the refocusing mirror mentioned in Section 3.3.5, which is used to get a reference signal proportional to the flux of the synchrotron source.

3.4.1 CiPo source optimization

During the first beamtimes we soon realized that the behaviour of the grazing incidence monochromator was far worse than that of the normal-incidence one. First of all, we measured a degree of linear polarization of less than 50%, when instead a synchrotron beamline should provide a linear polarization of about 90% or more; the second problem we encountered was the difficulty in the alignment process of the polarimeter stage. When using the NIM, the polarimeter is aligned with respect to the zero-order radiation of the grating, then the experimental chamber is put in vacuum and the grating is rotated to one of the XUV photon energies. At this point we had usually noticed that the stage was no longer aligned with the XUV beam. This was noticed by using a Ce:YAG phosphor, which emits yellow light when hit by ultraviolet radiation. The spot on the phosphor was seen moving as the polarimeter stage was rotated and, in addition, the quality of the Malus's curves was very low, and even with the aid of the motorized stage inside the chamber we weren't able to adjust and optimize the alignment of the polarimeter. The other anomaly was that the maxima of the acquired intensity curves were not detected at $\alpha = 90^\circ$ and $\alpha = 270^\circ$, as expected for horizontal linear polarization, but, instead, the Malus's curves were shifted by $10^\circ - 15^\circ$.

After some tests we identified the problem of these anomalies. When using the

SGM the beamline was dominated by the *bending* emission, instead of the wiggler emission. It is like having two different sources of radiation, bending and wiggler emission, which are comparable in intensity and have two different directions. In Fig. 3.24 we show the Malus’s curves acquired with the polarimeter in two cases, wiggler on and wiggler off, both for the SGM and the NIM.

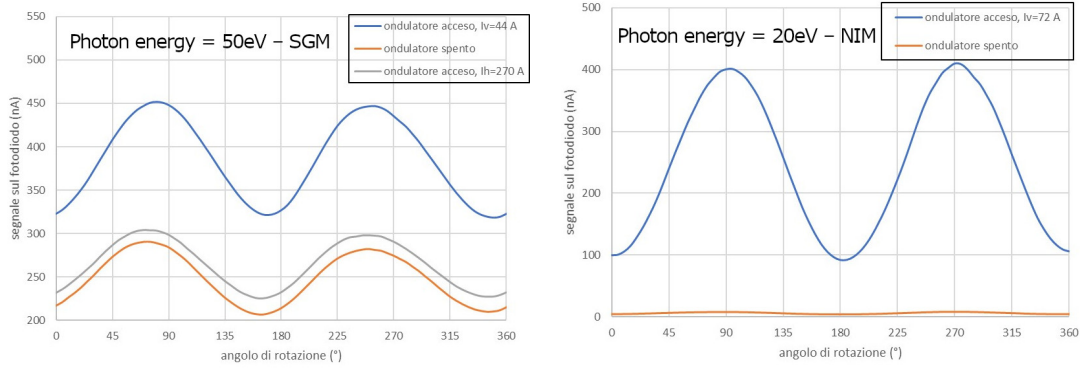


Figure 3.24: (Left) Malus’s curves acquired with turned on wiggler (blue curve) and turned off wiggler (orange curve) in the case of the SGM. (Right) Same curves in the case of the NIM.

When using the SGM, the signal acquired without wiggler, therefore the bending emission, is 67% of the signal we acquire with turned on wiggler. On the right of Fig. 3.24 we see the same curves acquired using the NIM. In this case the bending emission constitutes only 2% of the signal with turned on wiggler. This clearly shows that the SGM is misaligned with respect to the wiggler and thus an observer in the experimental station “sees” a combination of two radiation sources, the bending emission and the wiggler emission. This explains both the low degree of polarization we measured with the polarimeter and the difficulties in the alignment process.

To correct this problem we proceeded with the alignment of the double slits with respect to the wiggler source. The double slits are the entrance slits placed before (up-beam) the gratings and they limit the field of view (solid angle) from the monochromator that the source covers. With the aid of the reflection polarimeter we were able to successfully align the slits while checking the resulting degree of polarization as seen in the end-station. After this procedure the bending emission was measured to be 0.75% of the wiggler emission, in the case of circular polarization, and 0.24% in the case of horizontal linear polarization. Therefore, the beamline is now dominated by the wiggler emission and the amount of the bending radiation seen at the end-station is totally negligible.

Our proposed reflection polarimeter has been an incredibly useful tool to analyze, almost in real time, the polarization state of the radiation entering the experimental chamber, demonstrating its effectiveness as a diagnostic instrument for XUV polarimetry applications.

3.5 Fitting Stokes parameters

As mentioned in Section 3.3.4, after (downbeam) the mirror-stage a photodiode for the direct detection of XUV radiation is placed. The acquired signal is pro-

portional to the optical intensity of the beam after 3 reflections and, therefore, is related to the reflectances of the mirrors. A typical polarimetric measurement requires the acquisition of the XUV intensity while the rotation stage, and thus the mirror-plate, is rotated by 360° about the beam-axis. What is obtained is a one-dimensional plot of the XUV intensity with respect to the polarimeter angle. As mentioned in Section 3.3.5, the intensity plot is actually obtained by dividing the raw current signal from the XUV picoammeter by the electric current coming from the refocusing mirror. The resulting signal is thus an adimensional plot proportional to the light intensity, corrected for fluctuations and/or drifts of the synchrotron radiation intensity.

By varying the polarization of the beamline, which can be achieved by operating the Electromagnetic Elliptical Wiggler with different horizontal and vertical magnetic fields, which in turn is obtained by driving the wiggler with different horizontal and vertical currents, the intensity plot changes accordingly. By analyzing these plots, in particular by performing a fitting process, it is possible to retrieve the Stokes parameter of the input radiation [39].

In Fig. 3.25 some simulations of the output intensity plots, for different polarization states, are shown. These curves are typically called *Malus's curves*, named after Étienne-Louis Malus, a French physicist who analytically explained the change in intensity after light passes through a perfect polarizer. In Fig. 3.26 some polar plots of the same curves are shown.

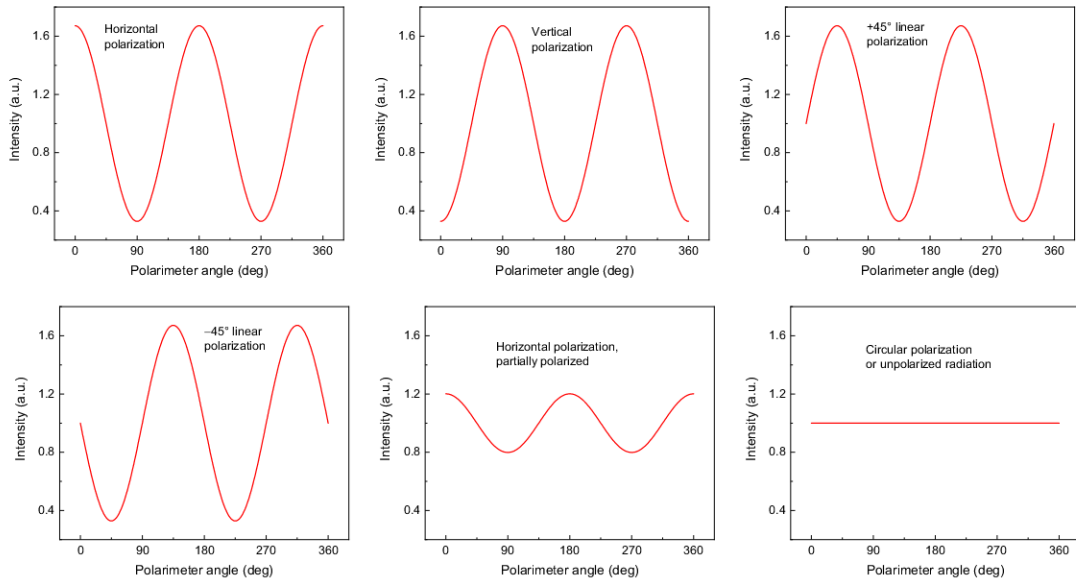


Figure 3.25: Simulations of the expected Malus's curves for different polarization states.

The equation that describes these curves, and that is employed in the fitting process, comes from Mueller calculus, which was introduced in Section 2.8. We remind that Mueller calculus is employed to describe the effects of different optical elements on the polarization of incoming radiation. It consists of a matrix method for manipulating Stokes vectors, in which the effect of a particular linear optical element is represented by a Mueller matrix.

It is recalled that a Stokes vector is made of four different components, called Stokes parameters, each describing a different aspect of the radiation, with respect

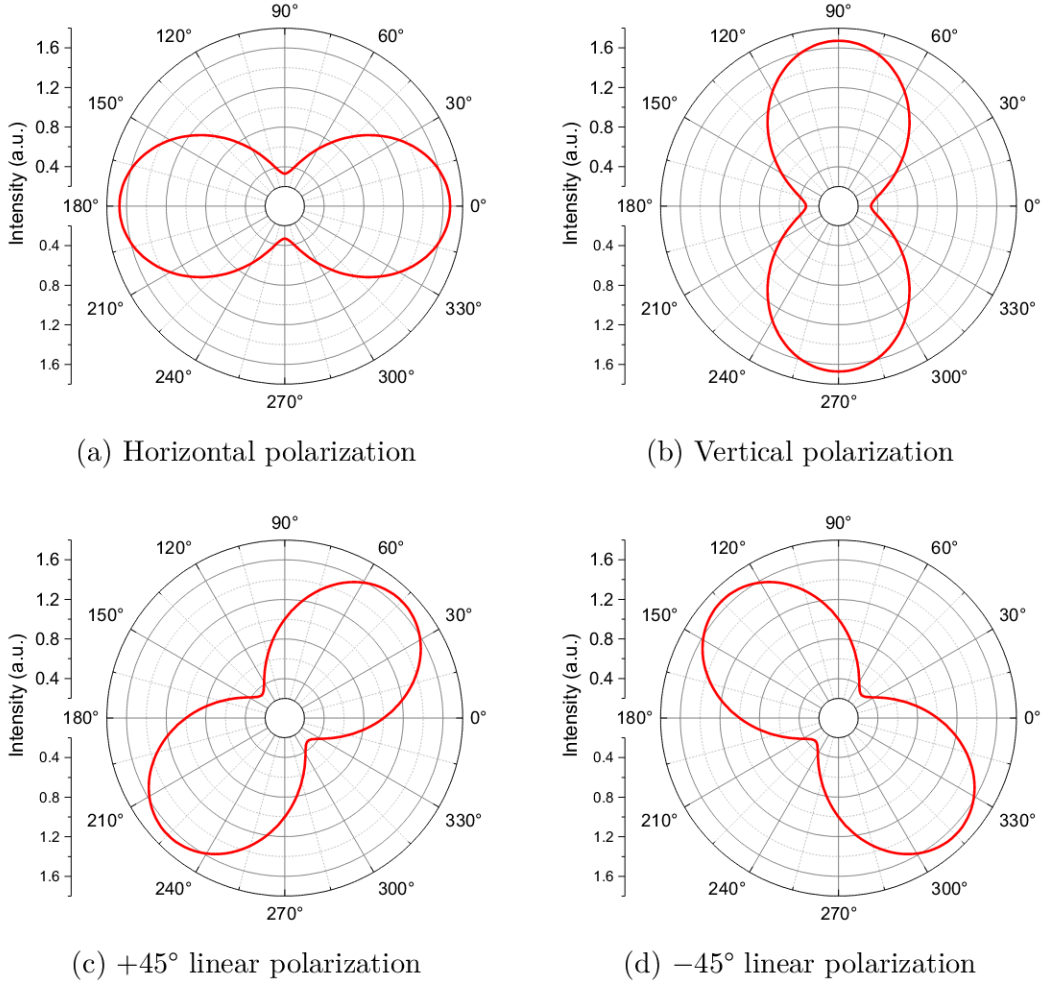


Figure 3.26: Malus's curves plotted in polar form.

to a specific reference frame, e.g. the laboratory frame. The first parameter, S_0 , represents the total intensity of the radiation, S_1 describes the amount of linear polarization (either horizontal or vertical), S_2 is related to linear polarization in the $+45^\circ/-45^\circ$ direction, S_3 describes the amount of circular polarization (either clockwise or anticlockwise).

The last three Stokes parameter can be used as a Cartesian coordinate system to plot the 3-dimensional vector (S_1, S_2, S_3) . The set of all polarization states are mapped to points on the surface of the Poincaré sphere of radius $P = \sqrt{S_1^2 + S_2^2 + S_3^2}$. If the total beam power is not of interest, a normalized Stokes vector is used by dividing the Stokes vector by the total intensity S_0 :

$$\mathbf{S}' = \frac{1}{S_0} \mathbf{S} = \left(1, \frac{S_1}{S_0}, \frac{S_2}{S_0}, \frac{S_3}{S_0} \right) = (1, S'_1, S'_2, S'_3). \quad (3.24)$$

This normalized Stokes vector \mathbf{S}' has unity power ($S'_0 = 1$) and the three significant Stokes parameters plotted in 3 dimensions will lie on the unity-radius Poincaré sphere, for pure polarization states, or inside the sphere if light is partially polarized.

If a beam of light is initially in the state \mathbf{S}_{in} and then passes through an optical element M and comes out in a state \mathbf{S}_{out} , we can write: $\mathbf{S}_{out} = M \times \mathbf{S}_{in}$, where

M is a 4×4 matrix. If a beam of light passes through a series of optical elements M_1, M_2, \dots, M_n it is written $\mathbf{S}_{out} = M_n \times \dots \times M_2 \times M_1 \times \mathbf{S}_{in}$.

In order to describe what happens to light reflected off a surface, it is necessary to introduce the complex reflection coefficients

$$\tilde{r}_s = r_s e^{i\delta_s}, \quad \tilde{r}_p = r_p e^{i\delta_p} \quad (3.25)$$

which describe how the s-polarized and the p-polarized components of the radiation, respectively, are affected by the reflection. In particular, the complex reflection coefficient \tilde{r} is the ratio of the reflected wave's electric field complex amplitude to that of the incident wave. Separate formulae for the s and p polarizations are required. The power (intensity) reflection coefficient, or reflectance, R , is simply the squared magnitude of r :

$$R_s = |\tilde{r}_s|^2 = r_s^2, \quad R_p = |\tilde{r}_p|^2 = r_p^2 \quad (3.26)$$

At this point, two quantities can be defined:

$$\psi = \tan^{-1} \frac{r_p}{r_s}, \quad \Delta = \delta_p - \delta_s. \quad (3.27)$$

ψ is related to the ratio of the complex coefficients' magnitudes while Δ is the difference between the phases of the two complex reflectivities. These two quantities are extensively used in ellipsometry and polarimetry and are therefore called *ellipsometric parameters*.

The Mueller matrix which describes the ideal isotropic reflection off a surface is the following [40]:

$$M(\psi, \Delta) = \frac{1}{2} (r_s^2 + r_p^2) \begin{pmatrix} 1 & \cos 2\psi & 0 & 0 \\ \cos 2\psi & 1 & 0 & 0 \\ 0 & 0 & \sin 2\psi \cos \Delta & -\sin 2\psi \sin \Delta \\ 0 & 0 & \sin 2\psi \sin \Delta & \sin 2\psi \cos \Delta \end{pmatrix} \quad (3.28)$$

where it can be noticed that the matrix elements depend only on the s- and p-reflectivity of the surface, both in term of field amplitude reflectivities (r_s and r_p) and ellipsometric parameters (ψ and Δ) but not on the polarization state of the input radiation.

The polarizer/polarimeter device that has been developed is made of 3 mirrors and this means that the incoming light undergoes 3 consecutive reflections, each described by its own reflections coefficients, \tilde{r}_s and \tilde{r}_p . The entire 3-mirror device can be modeled with a single Mueller matrix, where this time ψ and Δ have to take into account the three reflections:

$$\tilde{r}_{s,tot} = \tilde{r}_{s,1} \cdot \tilde{r}_{s,2} \cdot \tilde{r}_{s,3} = (r_{s,1} \cdot r_{s,2} \cdot r_{s,3}) e^{i(\delta_{s,1} + \delta_{s,2} + \delta_{s,3})} = r_{s,tot} e^{i\delta_{tot}}; \quad (3.29)$$

the same holds for the p-polarized component. Therefore, it can be written:

$$\psi_{tot} = \tan^{-1} \frac{r_{p,tot}}{r_{s,tot}}, \quad \Delta_{tot} = \delta_{p,tot} - \delta_{s,tot}. \quad (3.30)$$

The polarization state of the light coming out from such a three-mirror stage can be calculated as:

$$\mathbf{S}_{out} = M(\psi_{tot}, \Delta_{tot}) \mathbf{S}_{in}, \quad (3.31)$$

Since the whole stage will be rotated about the optical axis, it is useful to model the rotation with an appropriate Mueller matrix. In order to switch to a local frame which is rotated CCW (looking into the beam) by an angle α , we write:

$$\mathbf{S}_{out} = R(\alpha) \mathbf{S}_{in} , \quad \text{where } R(\alpha) = \begin{pmatrix} 1 & 0 & 0 & 0 \\ 0 & \cos 2\alpha & \sin 2\alpha & 0 \\ 0 & -\sin 2\alpha & \cos 2\alpha & 0 \\ 0 & 0 & 0 & 1 \end{pmatrix}. \quad (3.32)$$

The Stokes vector of the output radiation, as a function of the input Stokes vector, the ellipsometric parameters of the mirror-stage and the rotation angle, is thus given by

$$\mathbf{S}_{out} = R(-\alpha) M(\psi_{tot}, \Delta_{tot}) R(\alpha) \mathbf{S}_{in} , \quad (3.33)$$

where α is the rotation angle of the polarizer about the optical axis. We can see that the incoming light vector is first rotated to the local frame of the polarizer (α), then it passes through the polarizer, and lastly it is rotated back to the laboratory frame ($-\alpha$).

The only measurable Stokes parameter is S_0^{out} , which represent the radiation intensity at the output of the system. By computing the matrix multiplication, remembering that $\mathbf{S}_{in} = [S_0 \ S_1 \ S_2 \ S_3]$, we can find the analytical expression for the detected light intensity I_D :

$$\begin{aligned} I_D = S_0^{out} &= \frac{1}{2} (r_{s,tot}^2 + r_{p,tot}^2) (S_0 + S_1 \cos 2\psi_{tot} \cos 2\alpha + S_2 \cos 2\psi_{tot} \sin 2\alpha) = \\ &= \frac{S_0}{2} (r_{s,tot}^2 + r_{p,tot}^2) \left(1 + \frac{S_1}{S_0} \cos 2\psi_{tot} \cos 2\alpha + \frac{S_2}{S_0} \cos 2\psi_{tot} \sin 2\alpha \right) = \\ &= K (1 + S'_1 \cos 2\psi_{tot} \cos 2\alpha + S'_2 \cos 2\psi_{tot} \sin 2\alpha) . \end{aligned} \quad (3.34)$$

where K is a multiplicative factor taking into account the intensity reduction after the three reflections, S'_1 is the first normalized Stokes parameter (+1 for horizontal polarization, -1 for vertical polarization), S'_2 is the second normalized Stokes vector (+1 for $+45^\circ$ linear polarization, -1 for -45° linear polarization).

From Eq. (3.34) we can see that the detected intensity does not depend on the last Stokes parameter, S_3 . This means that, with a single reflection stage as in this experiment, nothing can be said about parameter S_3 and thus it is not possible to measure the amount of circularly polarized light. It is recalled, however, that synchrotron radiation is intrinsically highly polarized. In particular, the radiation is linearly polarized when observed in the orbital plane, and elliptically polarized when observed at a small angle to that plane. This means that the unpolarized fraction of the light is negligible and the following equality holds:

$$S_1^2 + S_2^2 + S_3^2 = 1 \quad (3.35)$$

where the Stokes parameters are already normalized, i.e. divided by S_0 . Therefore, parameter S_3 can be readily obtained with

$$S_3 = \sqrt{1 - S_1^2 - S_2^2} \quad (3.36)$$

In order to determine the polarization state of the incoming radiation we need to extract the Stokes parameter from the acquired data. To do so, a fitting process

using a non-linear least squares method is employed in which the output intensity (the Malus's curve) is fitted with Eq. (3.34). The independent parameter of the fitting problem is α while the fitted parameters are K , S_1 , S_2 and ψ . From now on, S_1 and S_2 , without quotation marks, refer to the already normalized quantities.

These parameters have been bounded by some proper lower and upper limits, in order to exclude not admissible values and reduce the local minima of the fitting process. For this reason, K was set to vary from 0 to positive infinity and S_1 and S_2 could vary from -1 to $+1$. Concerning ψ , the optimal solution would be to perform some reflectivity measurements on the mirrors in order to fix this value, thus reducing the number of free parameters. To do so, one would need the reflection coefficients r_s and r_p for the two incidence angles of the polarizer, 10° and 20° in our case. One should calculate ψ as the following:

$$\psi = \tan^{-1}\left(\frac{r_p}{r_s}\right) = \tan^{-1}\left(\frac{r_{p,1} \cdot r_{p,2} \cdot r_{p,3}}{r_{s,1} \cdot r_{s,2} \cdot r_{s,3}}\right) = \tan^{-1}\left(\frac{r_{p,10^\circ}^2 \cdot r_{p,20^\circ}}{r_{s,10^\circ}^2 \cdot r_{s,20^\circ}}\right), \quad (3.37)$$

where the reflectivity values at 10° are squared since there are two mirrors working at that angle. This process would have to be performed for each photon energy used in the experiment.

What was initially done, instead, was to let the ψ value vary between a lower and an upper limit, like the other fitting parameters. The lower bound for ψ corresponds to the value calculated using the theoretical reflection coefficients, supposing zero roughness of the reflecting surface, i.e. in the presence of an ideal mirror. This represents the best achievable reflection polarizer, for a given photon energy. Since r_p is lower or equal to r_s , the maximum value for the ratio r_p/r_s is unity and, therefore, the upper bound is $\psi = 45^\circ$.

The algorithm that has been employed solves a non-linear least-squares problem with bounds and constraints on the variables. Given the residuals $f(x)$ (an m -D real function of n real variables) and the loss function $\rho(s)$ (a scalar function), the algorithm finds a local minimum of the cost function $F(x)$.

$$\arg \min_x F(x) = \arg \min_x \frac{1}{2} \sum_{i=0}^{m-1} \rho [f_i(x)^2]$$

where x is the vector of fitted parameters (length: n) and m is the number of observations, i.e. the number of points of a single Malus's curve. The purpose of the loss function $\rho(s)$ is to reduce the influence of outliers on the solution. It takes the form

$$\rho(z) = 2 \left(\sqrt{1+z} - 1 \right) \quad (3.38)$$

The residuals $f(x)$ are the difference between the experimental data and the fitted model value, calculated at each of the m observation points:

$$f_i(x) = y_i - \hat{y}_i \quad \text{for } i = 0, 1, \dots, m-1 \quad (3.39)$$

The Python solver employed in the fitting process uses a Trust Region Reflective algorithm to minimize the cost function $F(x)$. It is a modification of the Levenberg–Marquardt algorithm and uses *trust regions*, i.e. subsets of the region of the objective function that are approximated using a model function (often a

quadratic). If an adequate model of the objective function is found within the trust region, then the region is expanded; conversely, if the approximation is poor, then the region is contracted.

It was soon realized that the fitting results, i.e. the obtained fitting parameters, are highly affected by their starting point, or starting guess. This is especially true for the two Stokes parameters S_1 and S_2 . This behavior shows that there are several false minima, also known as local minima, where the objective function value of the fitting problem is greater than its value at the so-called global minimum. In order to be sure that the found minimum corresponds to the global minimum, the fitting process should be performed by widely differing the initial values of the parameters. When the same minimum is found regardless of the starting point, it is likely to be the global minimum. For this reason, it was decided to perform 1000 runs of the same fitting process, each time choosing random values, in the range -1 to $+1$, for the starting points of both S_1 and S_2 . The starting points of parameters K and ψ were found to have less impact on the fitting, therefore their starting points were fixed at 0 and its lower limit, respectively. Proceeding in this way, we obtained 1000 values for each fitting parameter, at each given photon energy. The fitted parameters are then visualized in the form of histograms, which show the distribution and the spread of the found values.

3.6 Results

The polarimeter setup has been tested during several beamtimes on the CiPo beamline, in Trieste. During the course of these experiments, different adjustments have been made, different mirrors have been tried, and various improvements have been proposed. We started by measuring the polarimetric response of gold and, subsequently, we measured its reflectivity on a dedicated beamline. Afterwards, we switched to ruthenium mirrors and the same characterization as for gold was performed. Ultimately, we performed some ellipsometric experiments on thin films with the aim of characterizing the optical and electrical properties of the samples by using our proposed polarimetric system.

3.6.1 Polarimetric measurements of gold

During the first tests of the system only gold-coated mirrors had been used and the alignment of the system was performed with manual stages and adjustments. The experiment had been conducted both with linear and circular polarization, with photon energies ranging from 21.2 eV to 90 eV, corresponding to wavelengths 58.5 nm down to 13.8 nm.

As explained before, for each photon energy of interest the radiation intensity after the mirror-stage was recorded by a photodiode as a function of the rotation stage's angle. The stage was typically rotated by 360° in 5° steps, leading to 72 measuring points. For each point, the rotation stage would stop for ~ 1 s in order to acquire an averaged value of the XUV intensity and one for the reference signal. The light intensity is divided by the reference signal and the thus obtained curves are fitted with Eq. (3.34) in order to retrieve the Stokes parameters of the incoming light. The intensity plots, together with the fitted curves, are shown in Fig. 3.27 for the linear polarization case.

Since the fitting process had been carried out for 1000 runs, there are 1000 possible values for the Stokes parameters, for each photon energy. The values are shown as histograms in Fig. 3.29 for energies 21.2 eV, 50 eV and 80 eV. It is clearly observed that there is no well-defined global minimum, however, the obtained parameters are not spread over the whole range $(-1, +1)$ but, rather, tend to be more or less distributed around some specific values. Nevertheless, the observed values do not seem to follow a specific distribution, like a Gaussian for instance. Some histograms are approximately symmetric and unimodal, while others show a skewed pattern. We proceeded by calculating the mean value for each histogram, thus obtaining one value per photon energy, for each Stokes parameter. Parameter S_3 is actually derived from the first two by using Eq. (3.36), assuming that the incoming light is fully polarized. Given the first two Stokes parameters, it is possible to calculate the degree of linear polarization:

$$\text{DOLP} = \sqrt{S_1^2 + S_2^2} \quad (3.40)$$

Fig. 3.30 shows all three Stokes parameter as a function of the photon energy and, on the right, the degree of linear polarization. It is readily observed that S_1 is higher than 0.9 for all energies, and S_2 is close to zero. S_3 is rather constant with an average value of 0.3. This indicates that the incoming radiation is highly polarized in the horizontal direction but still displays some ellipticity, as is suggested by the plot of the degree of linear polarization, which is always greater than 90% but never exactly 100%. The elliptical polarization component is due to the off-plane emission of the wiggler, as this emits perfectly linear polarization only in the orbital (horizontal) plane of the synchrotron ring, while an observer at an angle from this plane “sees” elliptical polarization.

In Fig. 3.28 all Malus’s curves are normalized with respect to their value at $\alpha = 0^\circ$, in order to plot them and compare them on the same graph. What is clearly noticed is the high contrast of the curves at low photon energies, which decreases monotonically as the energy is increased. The contrast is defined as the following:

$$C = \frac{I_{D,\max} - I_{D,\min}}{I_{D,\max} + I_{D,\min}} \quad (3.41)$$

where $I_{D,\max}$ is the maximum intensity, e.g. the intensity at $\alpha = 90^\circ$, and $I_{D,\min}$ is the minimum intensity, e.g. at 0° . The contrast is directly related to the difference between the two reflectances (R_s and R_p) and it gives us an idea about the ability of the polarimeter to distinguish and discriminate different polarization states. A high contrast allows for an efficient characterization of the polarization even when the incoming radiation is not fully polarized, whereas a low contrast produces “flatter” curves, making it more difficult to perform the fitting process. The contrast is in fact directly linked to the Stokes parameters. The analytical formula can be derived by finding the expressions of the minimum and the maximum values of the Malus’s curve equation (Eq. 3.34), and by putting them into Eq. (3.41).

$$C = \cos 2\psi \left[S_1 \cos \left(\arctan \frac{S_2}{S_1} \right) + S_2 \sin \left(\arctan \frac{S_2}{S_1} \right) \right] \quad (3.42)$$

One thing to notice is that in Mueller calculus, α (the polarimeter angle on the x -axis) is the angle between the reflecting surface and the horizontal plane (orbital

plane, xz -plane), therefore, $\alpha = 0$ corresponds to mirrors “lying”, i.e. incidence planes parallel to the yz -plane. In our experiment, however, we chose the zero-point such that when $\alpha = 0$ the mirrors were “standing”, as seen in Fig. 3.15. As is easily seen, this is just a matter of which reference frame one chooses. We could simply change the signs of the extracted Stokes parameters, in order to be consistent with the Mueller calculus convention, or we simply state that, in our reference frame, $S_1 = +1$ corresponds to vertical polarization (y -axis) while $S_1 = -1$ corresponds to horizontal polarization (x -axis). The former option has been adopted here.

The intensity curves had been measured also with circularly polarized light in the same photon energy range, from 21.2 eV to 90 eV. In Fig. 3.31 three Malus’s curves with their fitted plots are shown, together with the histograms of the fitted S_3 Stokes parameters. The contrast of these curves is significantly lower than in the linear polarization case, and the values of parameter S_3 are higher than 0.8, indicating a degree of circular polarization of more than 80%.

The contrast of all the intensity curves as a function of the photon energy, compared in the two cases, linear and circular polarization, is shown in Fig. 3.32.

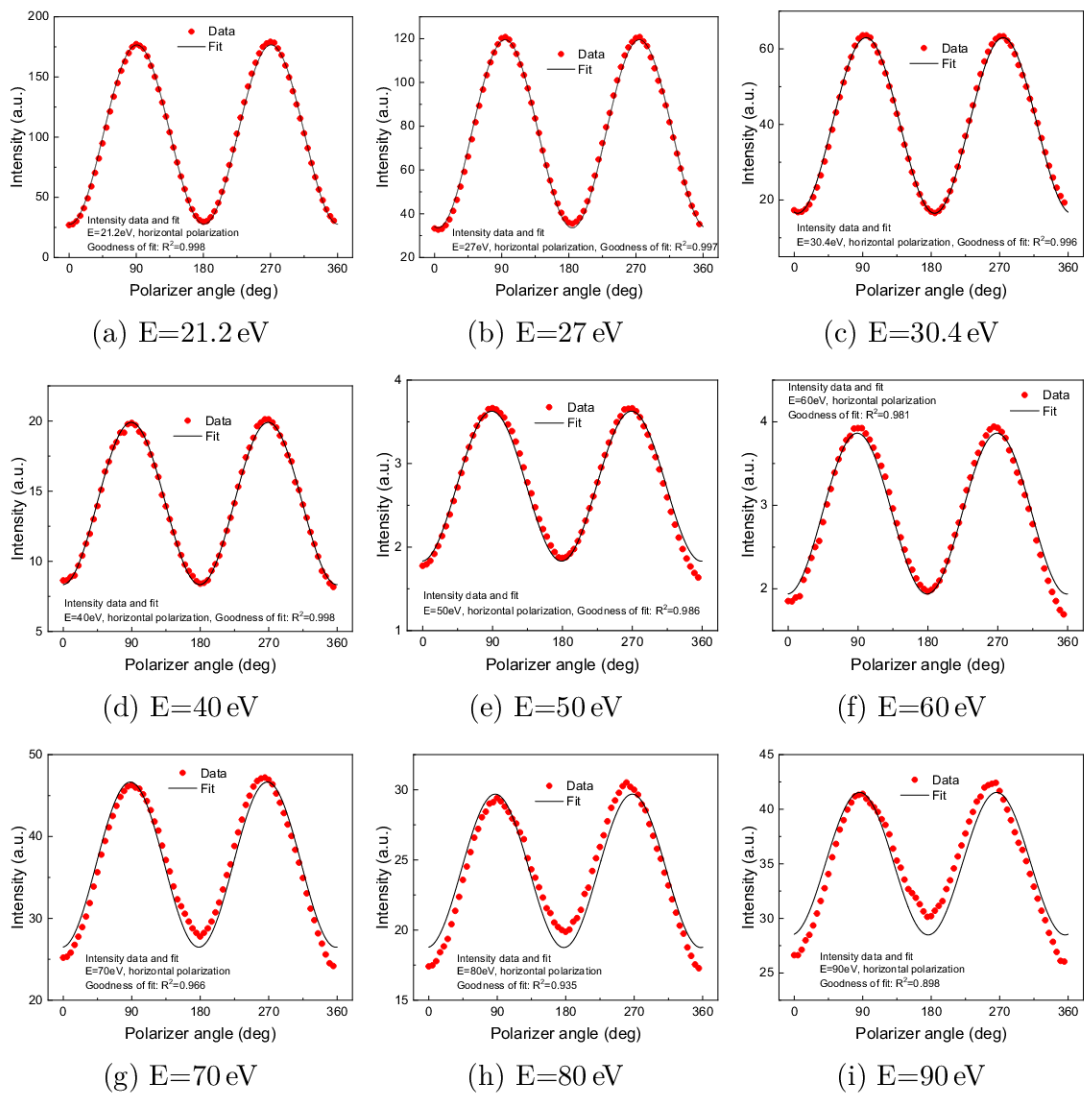


Figure 3.27: Intensity plots and fitting curves of gold, for the different photon energies (linear polarization), beamtime: June 2019.

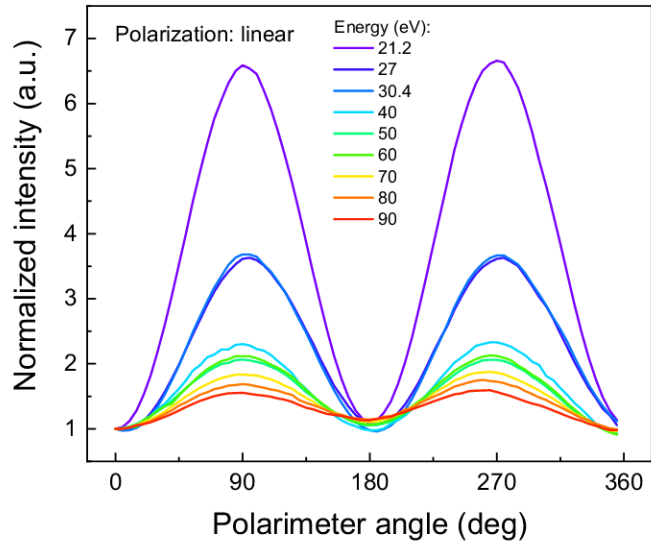


Figure 3.28: Intensity plots of gold for the different photon energies (linear polarization) normalized with respect to the value at 0° .

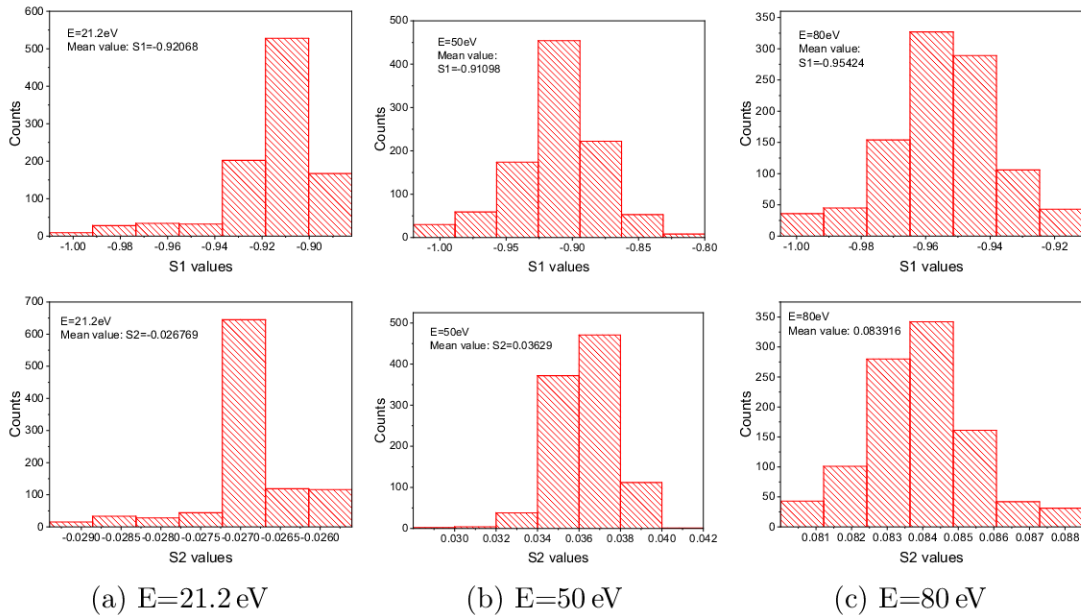


Figure 3.29: Histograms of the Stokes parameters' values obtained during 1000 runs of the fitting process of the gold Malus's curves (linear polarization).

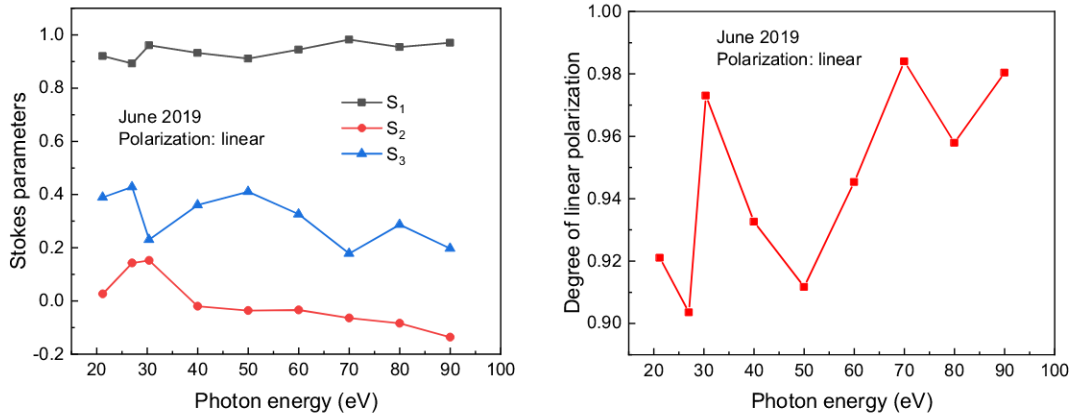


Figure 3.30: (Left) The three fitted Stokes parameters plotted with respect to the photon energy. (Right) Degree of linear polarization vs. photon energy.

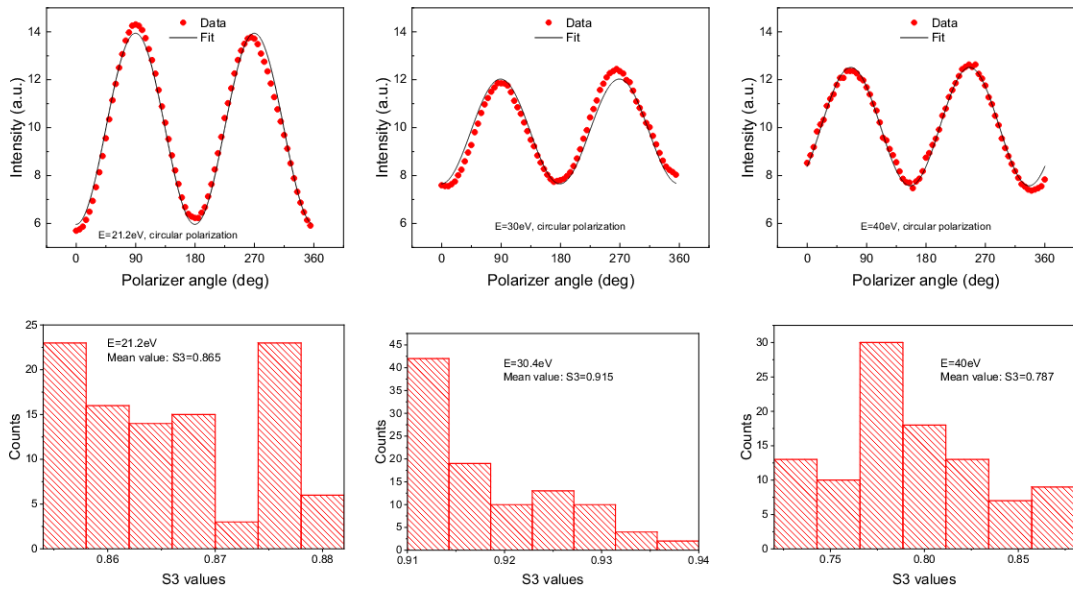


Figure 3.31: Circular polarization case with gold mirrors. (Top) Intensity plots and fitting curves for 3 photon energies. (Bottom) Histograms of the fitted S_3 parameters.

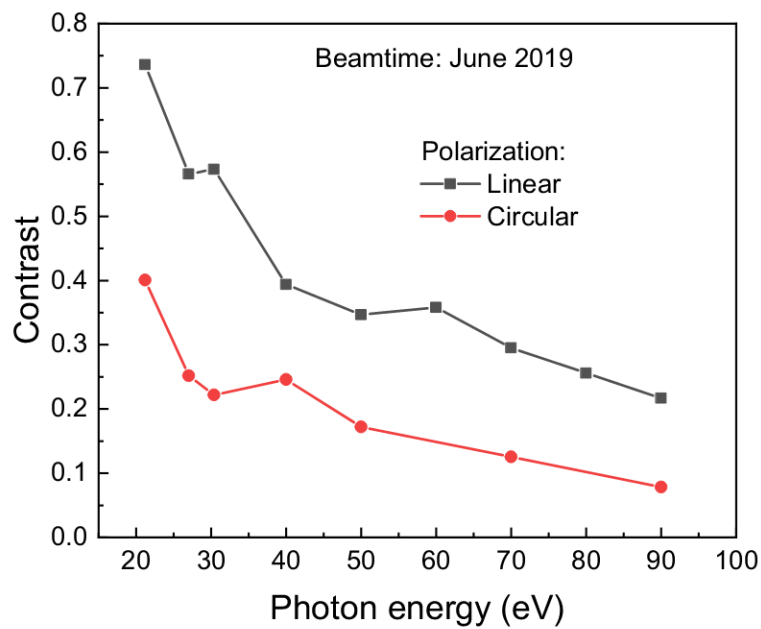


Figure 3.32: Contrast of the Malus's curves with respect to photon energy, for linear and circular polarization, for gold mirrors.

Probable carbon contamination

After several beamtimes using gold mirrors we noticed a significant deterioration of the contrast values and thus of the subsequently fitted Stokes parameters. During the first beamtimes, the contrast values of the acquired intensity curves were always in good agreement with the theoretical values, calculated with Eq. (3.42) using the theoretical values of the reflectivities and assuming a horizontal linear polarization state ($S_1 = 1, S_2 = 0$).

After three beamtimes in which only gold had been used, the intensity curves showed a lower contrast than before, significantly lower than the expected values, as seen in Fig. 3.33. The first points at low energies, from 9 eV to 12 eV, are measured with a LiF filter (cut-off energy: 11.8 eV) inserted before the experimental chamber, in order to limit the contribution of the second order coming from the normal-incidence grating (GNIM).

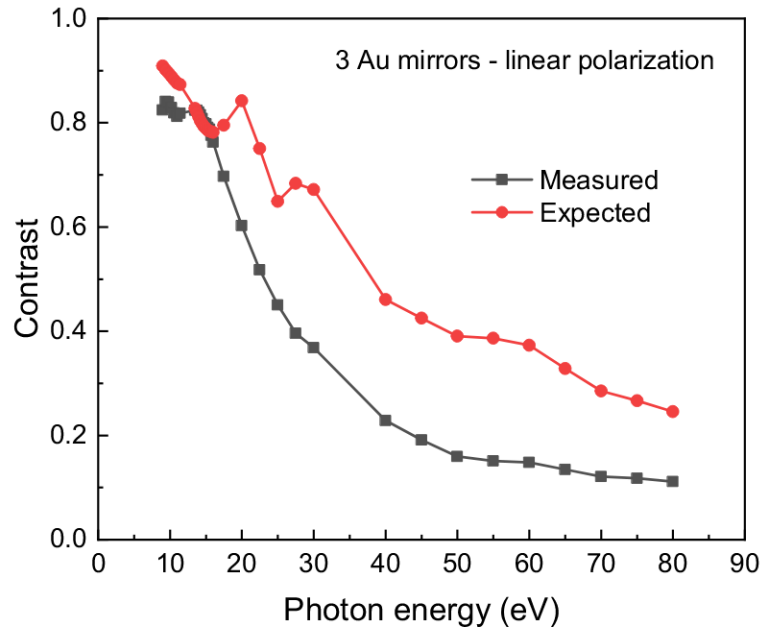


Figure 3.33: Contrast vs. photon energy with 3 gold mirrors. Except for a small spectral region around 9–15 eV, the measured values are significantly lower than the expected ones. Beamtime: December 2020.

The low measured contrast can be explained by the degree of linear polarization of the CiPo beamline, which is near 90%, certainly not 100%. It is possible, however, that the metal coating of the mirrors has been damaged by the repeated dose of XUV radiation, or, more probably, by a contamination of carbon, which is a major problem in vacuum experimental chambers [41, 42]. Several studies highlight how various factors and environmental conditions, such as beam illumination, residual gas pressure and composition, and interaction with liquid water, could play roles in the build-up of carbon on the surface [43]. Furthermore, beam-induced effects locally increase the amount of carbon in the irradiated area. We tested this hypothesis by first performing a series of fitting processes of the Stokes parameter S_1 , simulating different thicknesses of a hypothetical superficial carbon layer. The results of the simulation are shown in Fig. 3.34. In this case, only

the low-energy spectral range ($E < 33$ eV) has been acquired because, during the whole beamtime, the control software of the grazing incidence monochromator (SGM) was under maintenance and thus only GNIM could be used.

The purple curve (no carbon layer) is Stokes parameter S_1 as retrieved with the fitting process on the acquired Malus's curves. The other curves represent the same parameter S_1 obtained with simulations of an increasing carbon-layer thickness on top of the gold mirror. It is clearly observed that only at low energies (below 17 eV) we get an acceptable value for S_1 while, at higher energies, as the thickness of the (simulated) contaminant layer increases also parameter S_1 increases, getting progressively closer to 0.9, which is a reasonable value for linear polarized radiation on CiPo.

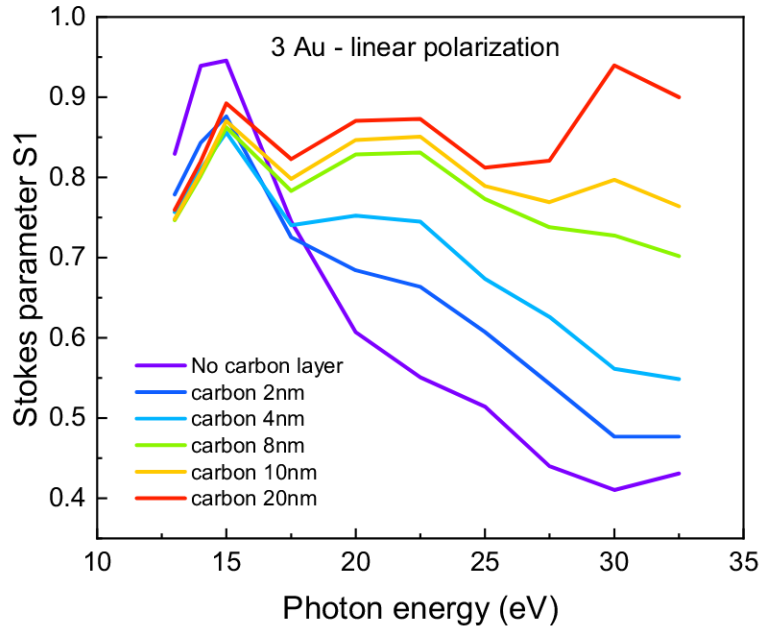


Figure 3.34: Fitted Stokes parameter S_1 obtained by fixing different ψ values, corresponding to different thicknesses of a superficial carbon layer.

Reflectivity measurements

To further investigate the cause for the low observed contrast, we decided to perform some reflectivity measurements on the gold mirrors, in order to quantitatively evaluate the degradation of the surface.

For accurate reflectivity measurements we relied on a dedicated beamline in Trieste: BEAR (Bending magnet for Emission, Absorption and Reflectivity). This beamline aims to provide a number of spectroscopic tools to investigate the basic properties of the electronic states in solids or molecules through the measurement of the optical absorption, the reflectivity and the photoemission yield in a UHV environment. The apparatus is based on a bending magnet as a source, a beamline optics delivering photons from near visible up to about 1600 eV with selectable degree of ellipticity and an end-station featuring, in an UHV environment, a large variety of scattering geometries. The UHV end-station has a movable hemispherical electron analyzer and a set of photodiodes to collect angle resolved

photoemission spectra, optical reflectivity and fluorescence yield, respectively. The photoemission/scattering geometries can be chosen with a wide flexibility thanks to the movability of the detectors inside the UHV chamber.

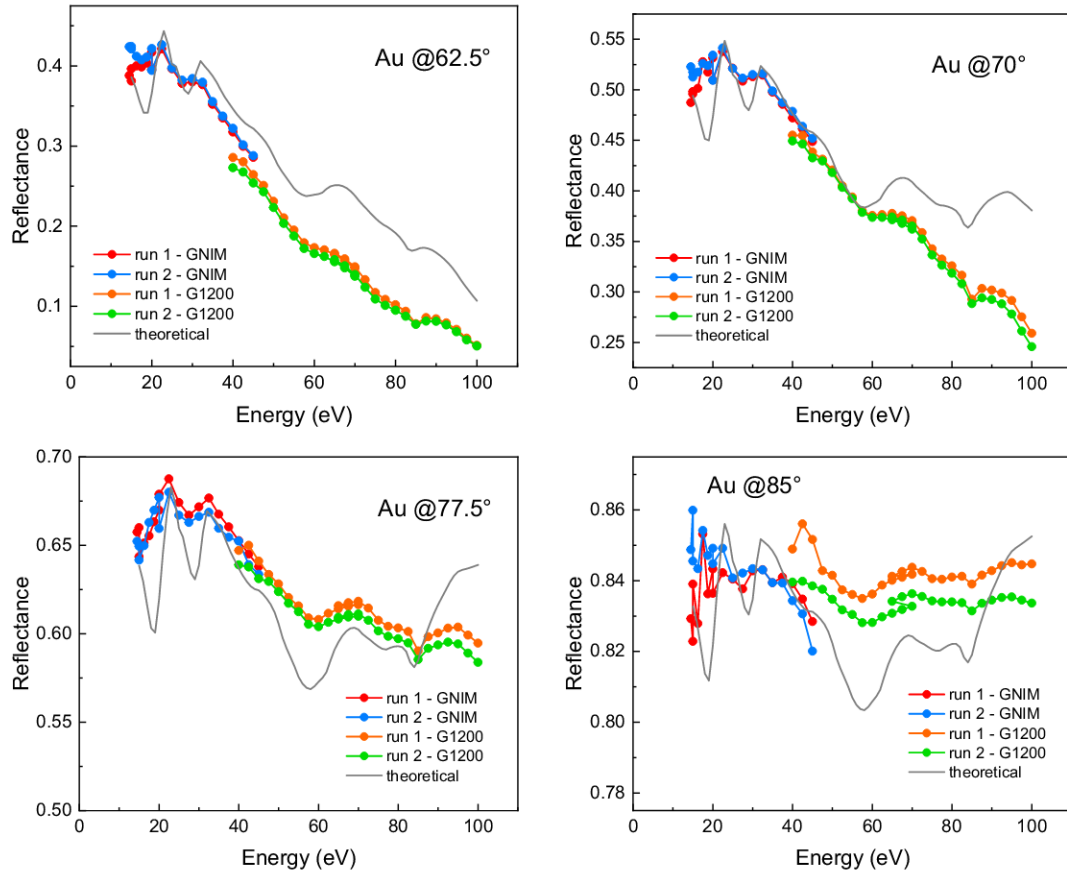


Figure 3.35: Reflectance curves of gold as a function of the photon energy, for different incidence angles.

The reflectance of the gold samples was measured with s-polarized radiation, from 14 eV to 100 eV for different incidence angles, from 60° to 85°. In Fig. 3.35 we show the reflectance curves of gold taken at 4 different incidence angles. It can be seen that there are two separate sets of points: a low-energy region (from 14 eV to 45 eV), and a high-energy region (from 40 eV to 100 eV). For each region two measurements have been taken, run 1 and run 2. The continuous line, in gray, represents the theoretical reflectance. It can be clearly seen that at low energies, up to ~ 50 eV, there is good agreement between the acquired data and the theoretical one, whereas at higher energies the behaviour of gold is worse than the expected one. These measurements clearly indicate that the gold samples have undergone some kind of optical degradation, probably because of a combined effect of the repeated dose of XUV radiation and carbon contamination. In addition, it can be noticed that there are some evident differences between the reflectance values taken between the two runs, in the high-energy range (orange and green curves). This is due to the fact that, in the two runs, two different areas of the gold sample have been illuminated. Therefore, we can conclude that the carbon contamination is inhomogeneous on the sample surface.

The reflectance data has been modelled with a gold bulk with a 20 nm-thick

superficial layer of carbon, in order to simulate the suspected contamination. The acquired data has been fitted to retrieve the complex refractive index of carbon and gold, but the high number (4) of free fitting parameters did not lead to a defined global minimum of the objective function. This suggests that the simple proposed model, made of a superficial layer of carbon on top of a gold bulk, is not adequate to describe the carbon contamination and, therefore, the complete understanding of the phenomenon requires specific measurements like X-ray photoelectron spectroscopy (XPS) or near edge X-ray absorption fine structure (NEXAFS) [44, 45].

3.6.2 Polarimetric measurements of ruthenium

For our polarimetry application, we seek both a high reflectivity and a high contrast. One of the most common materials used in the field is gold, which offers a good reflectivity across a large spectral range and an acceptable contrast. Moreover, gold is the standard material extensively employed on optical elements working in the XUV range, and thus the deposition technique of gold is a well-established process, providing a cost-effective solution and high quality of the final deposition.

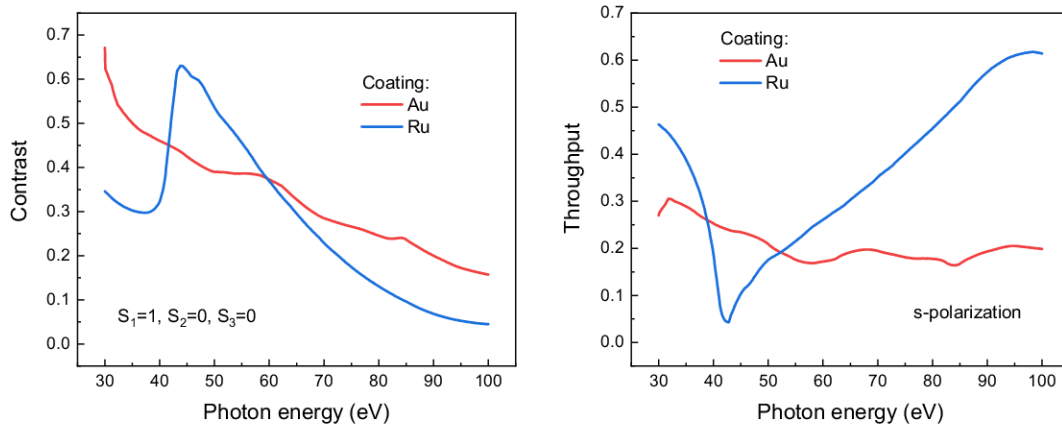


Figure 3.36: (Left) Expected contrast of a 3-mirror reflection polarimeter in the case of fully linear polarized light. (Right) Expected throughput for s-polarized light.

However, there are materials, especially transition metals, that exhibit higher performance with respect to gold, but limited application studies exist and, moreover, the deposition of these metals is not as simple and straightforward as with gold.

One of the goals of this project is to test the superior performance of ruthenium as a coating material for a reflection polarimeter. For this reason we first employed gold-coated mirrors and then switched to ruthenium, in order to test them both and compare their efficiency. In Fig. 3.36 the theoretical contrast and throughput of a 3-mirror polarimeter are shown as a function of the photon energy, for gold and ruthenium. It can be noticed that the expected contrast of ruthenium is not so different from gold, being just slightly lower than gold for higher photon energies, above ~ 60 eV. The remarkable feature of ruthenium is given by its higher

throughput (the product of the three s -reflectivities) compared to that of gold, for energies greater than ~ 55 eV.

The ruthenium coating was deposited on top of the same silicon plates used with gold, mono-crystalline silicon plates cut out from a standard 0.7 mm-thick wafer, polished on one side. The deposit was performed by using a technique called *sputtering*, performed at the Legnaro National Laboratories, part of the National Institute for Nuclear Physics. Sputtering is a PVD technique (Physical Vapor Deposition), a low temperature process where a plasma is generated in vacuum, in order to bombard the target connected to the negative electrode of an electric power supply with positive ions. The target is vaporized and the vapours are deposited on the substrate creating a thin atomic layer over atomic layer. The sputtering technique allows the deposition of thin films of any material on a substrate of a second material, with practically infinite applications ranging from high temperature superconducting films to hard coatings for cutting tools, from films that limit the secondary ionization of the surfaces to the materials used in thermodynamic panels. An important advantage of sputter deposition is that even materials with very high melting points are easily sputtered and the deposited films have a composition close to that of the source material.

Reflectivity measurements of ruthenium samples

After a deposition of 70 nm of Ru, with a subsequent surface analysis that showed a surface roughness of ~ 0.2 nm, which is sufficiently low to avoid surface scattering, we decided to measure the reflectivity of the ruthenium mirrors on the BEAR beamline. The reflectance was measured with s -polarized radiation, from 0° to 90° glancing angle (the angle between the incident beam and the sample surface), for different photon energies, 60 eV to 90 eV. The acquired reflectances and the theoretical curves are shown together in Fig. 3.37. It is observed that there is an optimal agreement between the measured reflectance and the theoretical one, indicating that the deposited layer is indeed ruthenium, with a high quality of the sputtering process.

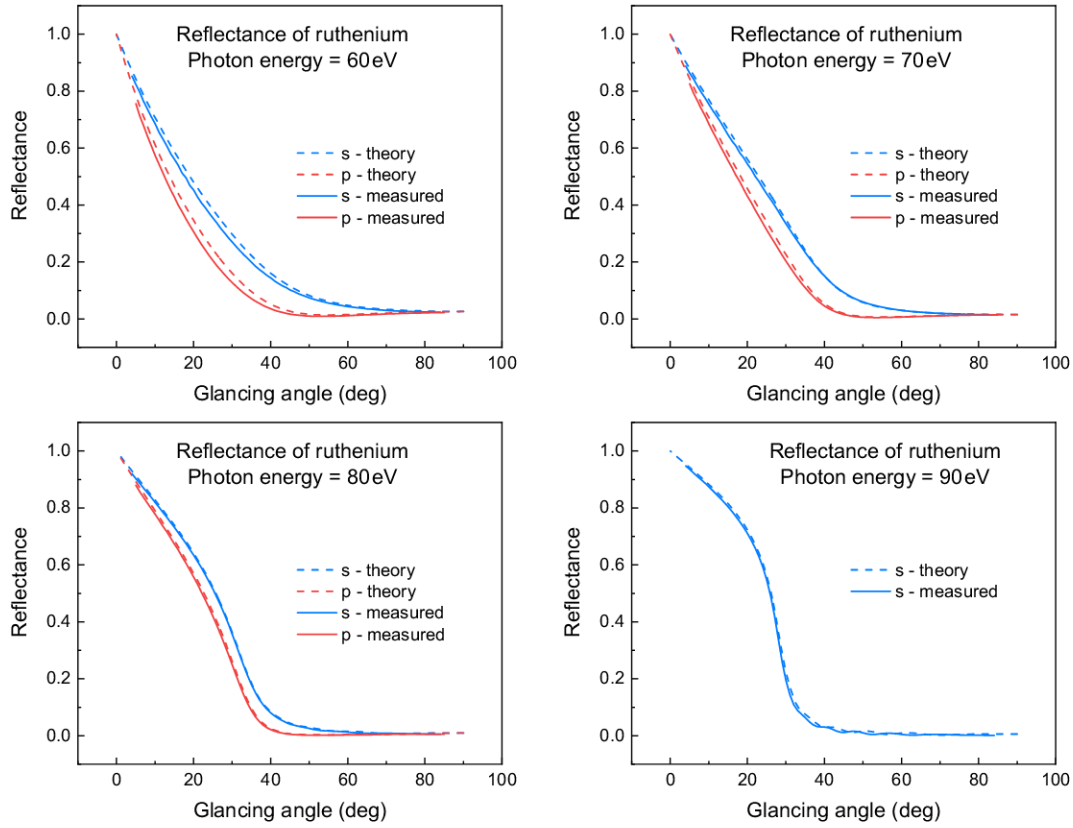


Figure 3.37: Reflectance curves of ruthenium (thickness: 70 nm) as a function of the glancing angle, for different photon energies. The p -polarization curve at $E = 90$ eV was acquired with a wrong instrument setting and thus is not shown here.

Intensity curves with Ru

In Fig. 3.38 all the intensity plots acquired with ruthenium mirrors are shown. Thanks to the alignment stage, the spot on the photodiode was not moving as the stage was rotated, thus symmetrical Malus's curves are obtained. The contrast of the intensity curves, together with the expected one, is plotted as a function of the photon energy in Fig. 3.39. The measured contrast is slightly lower than the expected one, especially in the region 40–60 eV. It was soon realized that the low measured contrast in this energy range was due to the misalignment between the wiggler source and the grazing-incidence monochromator (SGM), which is used for the high energy spectral range ($E > 30$ eV). The analysis of this problem and the subsequent alignment and correction using the reflection polarimeter has been already discussed in Sec. 3.4.1.

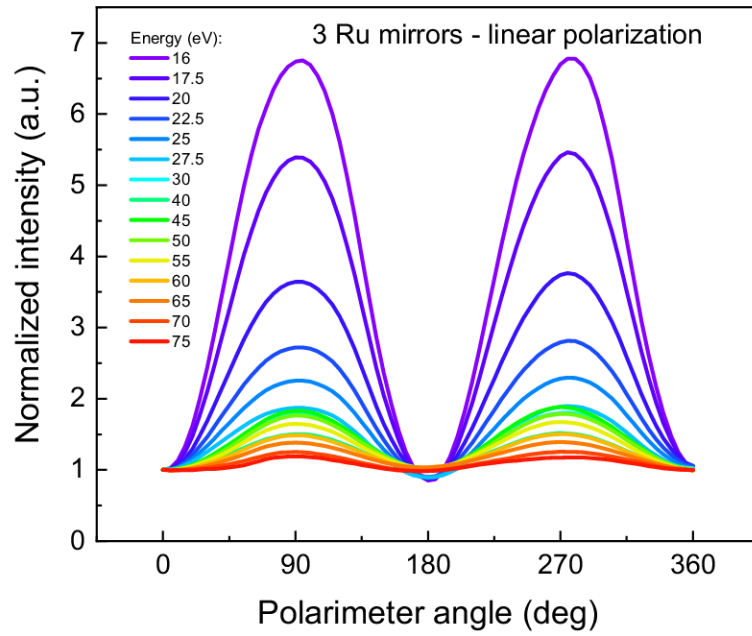


Figure 3.38: Malus's curves of 3 Ru mirrors for different photon energies, linear polarization.

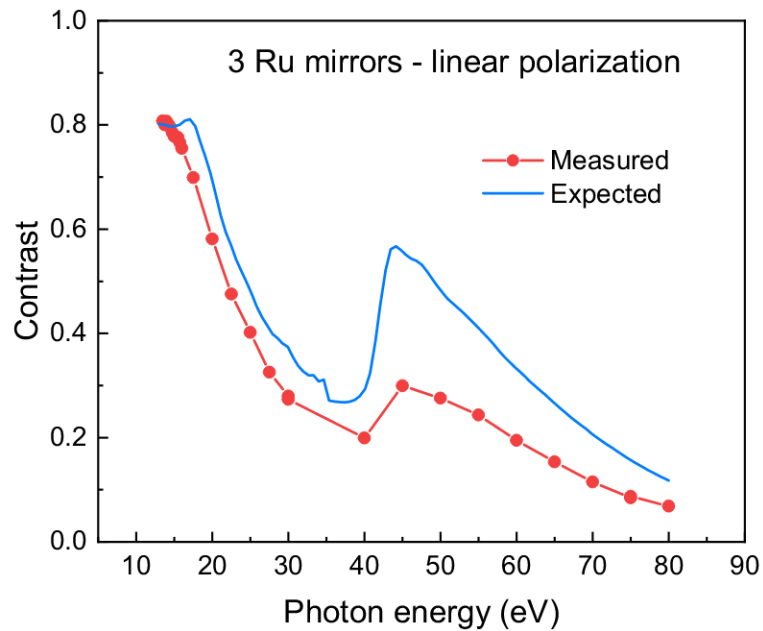


Figure 3.39: Measured and expected contrast of the polarimeter stage with 3 ruthenium mirrors.

Probable Ru contamination

After the alignment of the CiPo beamline, both gold and ruthenium mirrors had been extensively used but unfortunately the performance of the Ru-stage never reached the expected values. We soon suspected that after few beamtimes also the ruthenium samples may have undergone the same carbon contamination as already seen with gold.

By focusing only on the low-energy range, we acquired more Malus's curves and compared the measured data with different ruthenium refractive index data sets, in order to assess the reliability of the theoretical data and to evaluate whether the ruthenium coating is actually contaminated.

The contrast and the fitted Stokes parameter S_1 are shown in Fig. 3.40. The measured contrast (on the left) is compared to the theoretical one, obtained with 4 different values for the refractive index of Ru: 3 data sets found in literature, namely Cox, Windt, and Weaver, and the fourth (red points) which are obtained by fitting the reflectivity measurements performed on the BEAR beamline, as will be described later. All the expected contrast values are calculated supposing a perfectly (horizontal) polarized radiation, which corresponds to Stokes parameters $S_1 = 1, S_2 = 0$.

A similar approach is done for the fitting of Stokes parameter S_1 , where the ellipsometric parameter ψ is calculated using the different refractive index data sets; it is then fixed, i.e. it is not a free fitting parameter, and the best values of S_1 are found. The fitted Stokes parameter S_1 has a minimum value of ~ 0.7 at 32.5 eV as can be seen in Fig. 3.40 on the right.

The obtained results show a certain variability of the possible polarization states as a function of the photon energy, not sufficient, however, to justify such low values of measured contrast. Apparently, also the ruthenium samples could have undergone some carbon contamination, although not as severe as in the case of the gold mirrors. This is consistent with the fact that the gold samples have been used extensively over the course of several beamtimes, while the ruthenium mirrors were only tested few times.

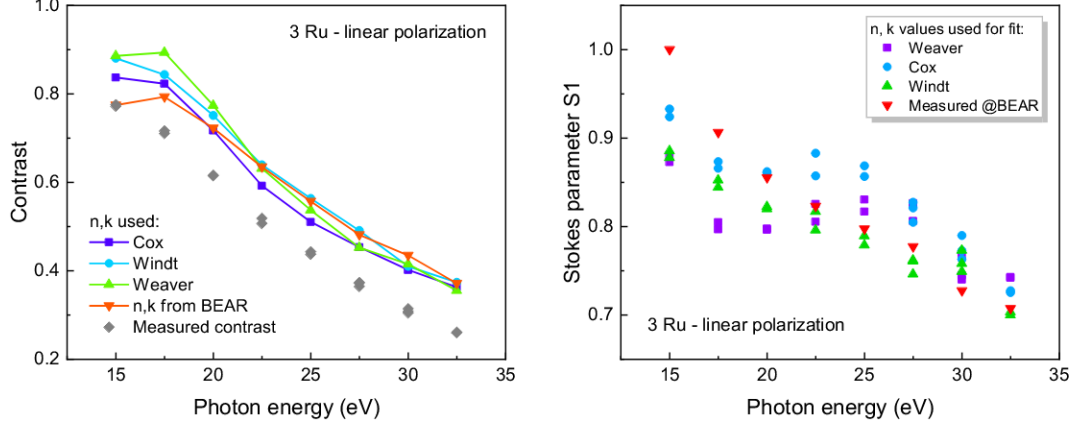


Figure 3.40: (Left) Measured and expected (with $S_1 = 1, S_2 = 0$) contrast for 3 Ru mirrors. (Right) Fitted Stokes parameter S_1 using different values of the refractive index. Beamtime: February 2021.

Reflectivity measurements after contamination

We measured the reflectance of the ruthenium samples after the probable carbon contamination, with s-polarized radiation, from 14 eV to 100 eV for different incidence angles, from 60° to 85° . The measured reflectance data has been used to fit for the refractive index of the sample. In particular, the refractive index is used to calculate the r_s and r_p reflectivities which, in turn, are used to calculate the ellipsometric parameter ψ of the whole 3-mirror stage. This parameter is then kept fixed during the fitting process of the Malus's curves and the Stokes parameter are retrieved. This procedure will be extremely useful in the thin films characterization described in the next section.

The acquired reflectance of ruthenium, and the theoretical one, are plotted in Fig. 3.41. As expected, there is no good agreement between the experimental data and the expected one, especially in the high-energy range. In the last two incidence angles, 77.5° and 85° , in the second run of the low-energy range, the instrumentation was not set correctly, and thus that data is not shown. In addition, it can be noticed that there are some evident differences between the reflectance values taken between the two runs, especially in the high-energy range (orange and green curves). This is due to the fact that, in the two runs, two different areas of the ruthenium sample, separated by few millimeters, have been illuminated. Therefore, we can conclude that the carbon contamination is inhomogeneous on the sample surface.

The fitted values of the refractive index of ruthenium are shown in Fig. 3.42. These values have been obtained with a fitting process of the plots shown above. The measured reflectance is actually a mix of s- and p-reflectance, since the BEAR beamline radiation is not fully linear but, instead, has a degree of linear polarization, DP, which is less than unity. Therefore, the measured data can be expressed as a linear combination of R_s and R_p , weighted by the degree of polarization, which is 90% over the whole photon energy range.

$$R_{\text{meas}} = DP \cdot R_s + (1 - DP) \cdot R_p . \quad (3.43)$$

This is the equation that is used to fit the experimental data. R_s and R_p are given

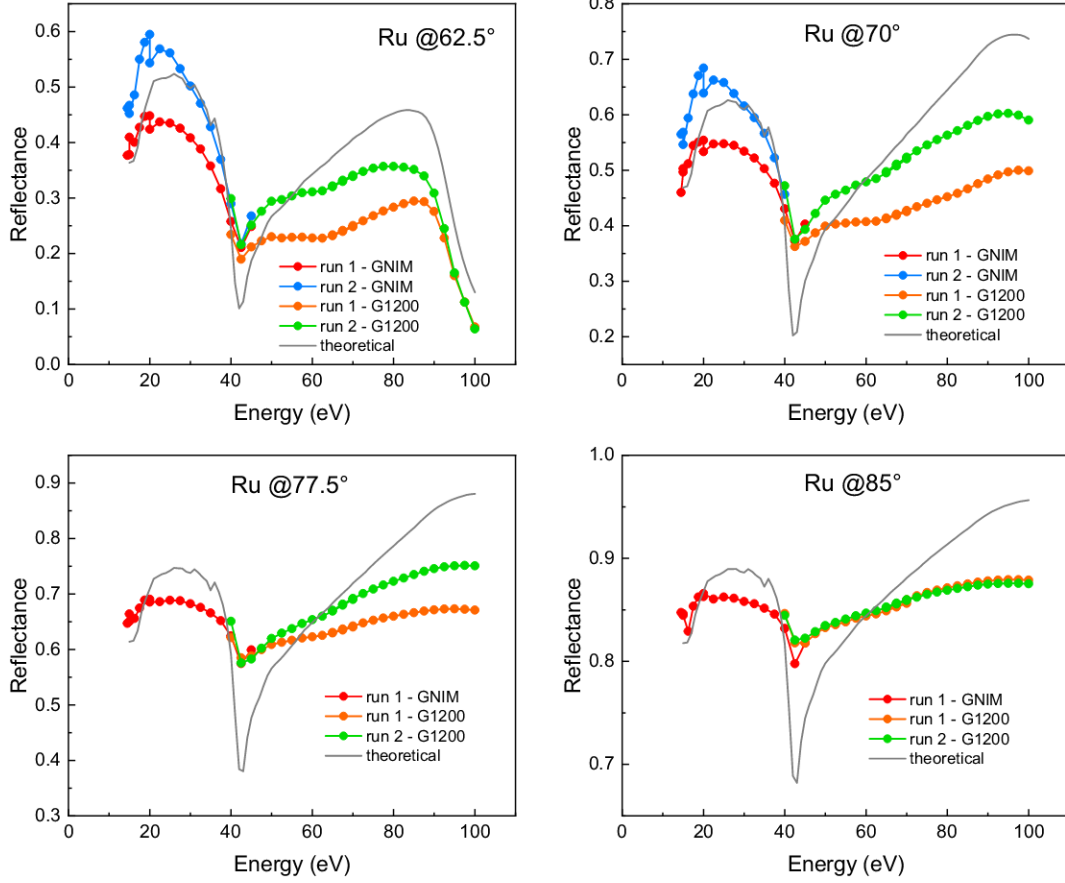


Figure 3.41: Reflectance curves of ruthenium as a function of the photon energy, for different incidence angles.

by Fresnel equations, which describe the reflection and transmission of light when incident on an interface between different optical media.

$$R_s = |\tilde{r}_s|^2 = r_s^2, \quad R_p = |\tilde{r}_p|^2 = r_p^2. \quad (3.44)$$

$$\tilde{r}_s = \frac{\sin \theta_g - \sqrt{\tilde{n}^2 - \cos^2 \theta_g}}{\sin \theta_g + \sqrt{\tilde{n}^2 - \cos^2 \theta_g}} \quad \text{for the } s \text{ component} \quad (3.45)$$

$$\tilde{r}_p = \frac{-\tilde{n}^2 \sin \theta_g + \sqrt{\tilde{n}^2 - \cos^2 \theta_g}}{\tilde{n}^2 \sin \theta_g + \sqrt{\tilde{n}^2 - \cos^2 \theta_g}} \quad \text{for the } p \text{ component} \quad (3.46)$$

where \tilde{n} is the complex refractive index: $\tilde{n} = n + ik$ and θ_g is the glancing angle, i.e. the angle between the incoming radiation and the surface of the sample. The two reflectivities are complex quantities:

$$\tilde{r}_s = r_s e^{i\delta_s}, \quad \tilde{r}_p = r_p e^{i\delta_p}$$

The result of the fitting process is actually an *equivalent* refractive index, obtained from the average reflectivity of two different areas of the sample. Nevertheless, the retrieved equivalent refractive index is significantly different from the

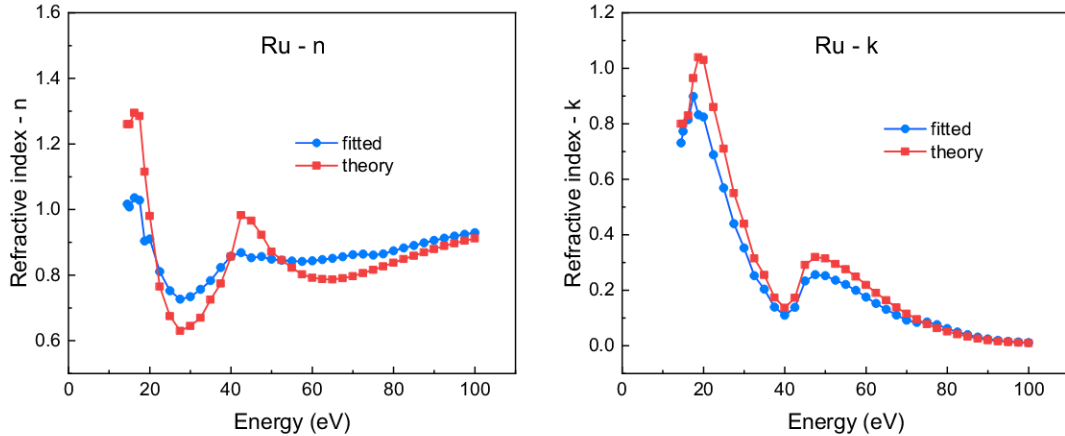


Figure 3.42: Fitted refractive index of ruthenium; real part, n (left) and imaginary part, k (right).

expected one, suggesting that the samples may have undergone some contamination.

These measurements show that the performance of ruthenium is very different compared to that measured on BEAR at the beginning, right after the successful deposition of 70 nm of Ru. It seems very probable that also the ruthenium samples suffered from the repeated dose of XUV radiation, in combination with the carbon contamination, which is a major problem in high-vacuum environments.

3.6.3 Polarimetric measurements of thin films

After the characterization of the beamline's polarization state with gold and ruthenium mirrors, we started to experiment with thin film samples like silicon dioxide and graphene. The idea was to measure the polarimetric response of thin films, employing the proposed reflection polarimeter and the developed fitting software tool, in order to investigate the possibility of studying the properties of such materials in the XUV spectral range. The aim was to perform a sort of ellipsometric experiment, in which we could retrieve some information about the sample by analyzing the polarimetric curves acquired at different photon energies. In particular, we were interested in the response difference between graphene and silicon dioxide (SiO_2), since the graphene is applied onto such a substrate.

The idea was to employ the 3 Ru mirror-stage in which only the central mirror, the one working at 20° glancing angle, was substituted by a graphene sample. We chose to work with 2 ruthenium samples because of the lower radiation (or contamination) damage they experienced, compared to the gold samples. The sample under test is made of a square SiO_2 substrate (10 mm side) on top of which the graphene is deposited. We had access to mono-layer and three-layer graphene, which should give us different polarimetric responses.

The interest for such measurements arises because of the contamination we observed on the gold and ruthenium optics. We therefore investigated the possibility of finding a procedure for an ellipsometric measurement which is not dependent on the reflectivity, and thus on the contamination, of the two outer mirrors. This would mean that regardless of the nature of the outer mirrors and their probable

contamination, one could get ellipsometric information about the sample under investigation just by acquiring two Malus's curves for each photon energy, one with the sample and one with the reference substrate.

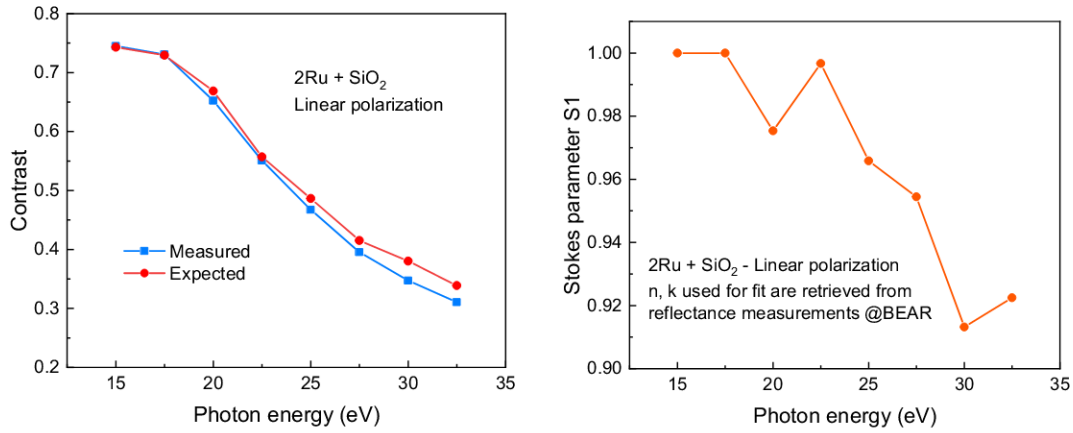


Figure 3.43: (Left) Measured and expected contrast in the case of 2 ruthenium mirrors and 1 SiO₂ sample. (Right) Fitted Stokes parameter S_1 .

First we measured the polarimetric response of the stage composed of 2 ruthenium mirrors and 1 silicon dioxide sample. The measured contrast is very close to the expected one (for the same configuration of 2 Ru + 1 SiO₂), as can be seen in Fig. 3.43. The expected contrast is calculated using the theoretical refractive index of SiO₂ and the fitted refractive index of Ru, which was retrieved from the reflectance measurements performed on the BEAR beamline.

On the right of Fig. 3.43, Stokes parameter S_1 is plotted against photon energy. The values are obtained by fitting the intensity curves while fixing the refractive index to the one obtained from the reflectivity measurements at BEAR. Parameter S_2 is not shown here as it remains constant, at approximately zero, across the whole energy range.

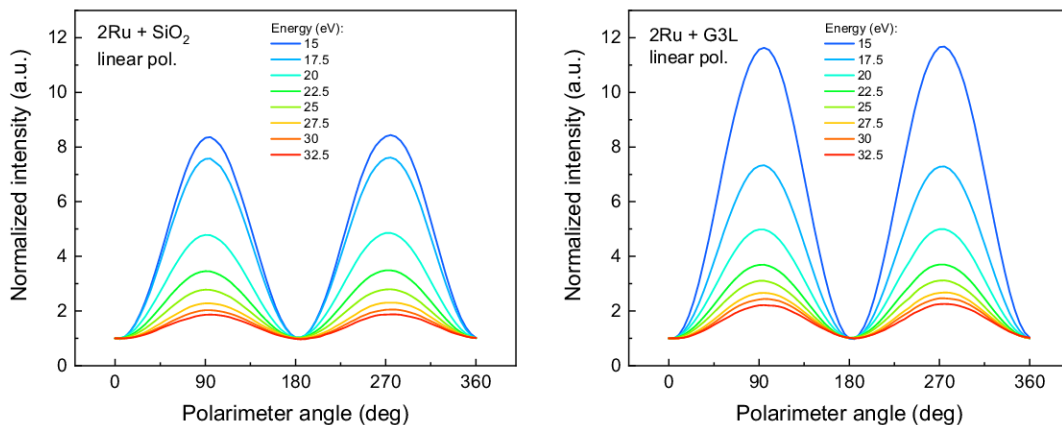


Figure 3.44: (Left) Intensity curves taken with the silicon dioxide sample. (Right) Intensity curves taken with the 3-layer graphene sample.

Afterwards, we substituted the silicon dioxide sample with the graphene. In Fig. 3.44 the intensity plots of silicon dioxide and 3-layer graphene (G3L) are

shown. It is clearly seen that the graphene layer enhances significantly the contrast of the Malus's curves.

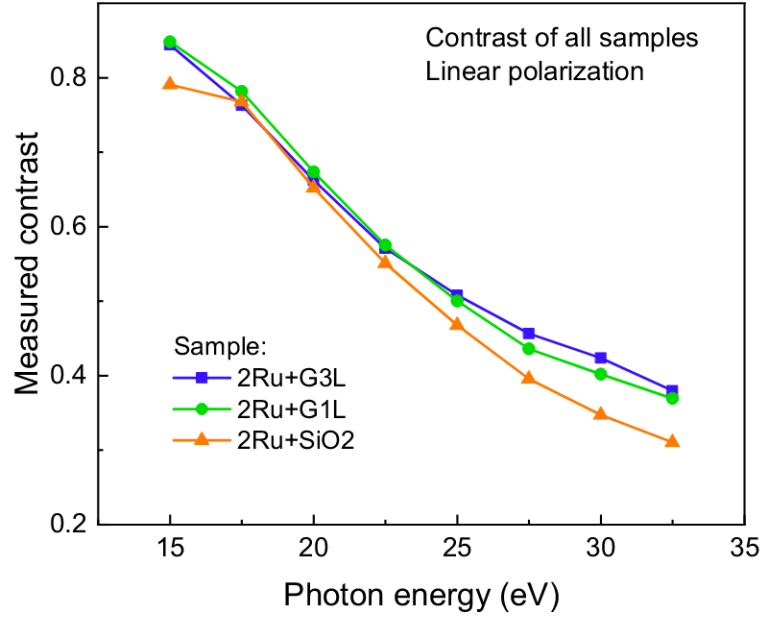


Figure 3.45: Measured contrasts of all the samples, for linear polarization. Error bars are not shown for sake of clearness.

Fig. 3.45 summarizes the contrasts of all the Malus's curves acquired with the different samples, namely 1-layer graphene, 3-layer graphene, and silicon dioxide. As expected, all samples decrease as the photon energy is increased. The biggest difference is observed between SiO₂ and the two graphene samples, while G1L and G3L behave very similar to each other. These measurements have been repeated several time to assess the repeatability of the experimental procedure. The error associated to the contrast measurements is, in the worst case, ± 0.014 (at 17.5 eV), given in the contrast's unit of measure. At 30 eV the error is in the range ± 0.005 . This shows that the differences in the measured contrasts between samples are bigger than the experimental uncertainty and thus the polarimetric measurement is able to discern between different samples.

Ellipsometric parameters

By fixing the Stokes parameters S_1 and S_2 to the values obtained with n, k retrieved on BEAR (Fig. 3.43 on the right), the Malus's curves of the samples have been fitted to find the ellipsometric parameter ψ , which contains the information about the optical characteristics of the whole mirror-stage, and thus also of the sample under test. Parameter ψ and the derived reflectance ratio are shown in Fig. 3.46.

As explained in Section 3.5, parameter ψ depends only on the optical characteristics of the 3-mirror stage, namely on the ratio of the p - and s -reflectivities. By taking the square of the tangent of ψ we obtain a ratio of reflectances (R_s and R_p), which is the quantity plotted in Fig. 3.46 on the right.

Our goal now was to find a procedure to eliminate the dependence on the two outer mirror's reflectivities, in order to be able to perform ellipsometric measure-

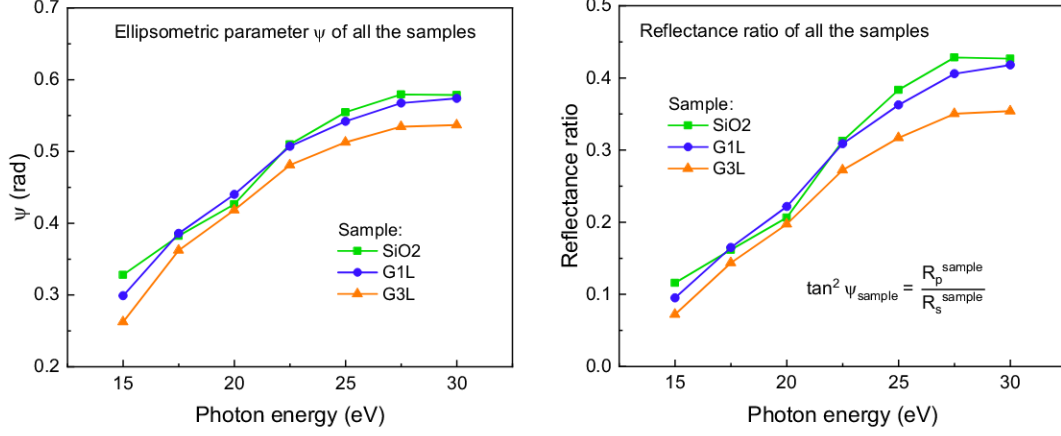


Figure 3.46: (Left) Ellipsometric parameter ψ retrieved from the fitting process of graphene and SiO_2 , as a function of the photon energy. The absolute error associated to the ψ measurement is ± 0.021 (rad). (Right) Reflectance ratio of the different samples calculated from the values of ψ . The associated error is ± 0.011 (in units of reflectance ratio).

ments regardless of the nature of the mirrors and their probable optical damage or contamination.

Recalling Eq. (3.37), the total reflectivity of the mirror stage is given by the product of the three different reflectivities. In our case we have 2 ruthenium mirrors and 1 sample (either graphene or silicon dioxide). If we choose to work with reflectances we can write

$$\tan^2 \psi_{\text{sample}} = \frac{R_{p,\text{tot}}}{R_{s,\text{tot}}} = \frac{R_{p,\text{Ru}_1} \cdot R_{p,\text{sample}} \cdot R_{p,\text{Ru}_2}}{R_{s,\text{Ru}_1} \cdot R_{s,\text{sample}} \cdot R_{s,\text{Ru}_2}}$$

Since the same 2 ruthenium mirrors are used both with graphene and with silicon dioxide, we can take the ratio of the two quantities to eliminate the dependence from the Ru optics:

$$\frac{\tan^2 \psi_{\text{graphene}}}{\tan^2 \psi_{\text{SiO}_2}} = \frac{R_{p,\text{graphene}}}{R_{s,\text{graphene}}} \cdot \frac{R_{s,\text{SiO}_2}}{R_{p,\text{SiO}_2}}$$

By using this normalization with respect to the silicon dioxide data, we obtain a quantity which is independent of the two mirrors used inside the 3-optic stage. This normalized reflectance ratio is plotted against photon energy both for the 1-layer and the 3-layer graphene in Fig. 3.47. It should be noticed that the reflectivity of the silicon dioxide sample is not needed to obtain these plots, as the graphene curves have been normalized with respect to the SiO_2 data.

The normalization highlights the difference between the two samples, and shows that the proposed polarimeter is an effective tool to measure the polarimetric response of thin films, even in the case of mono-atomic layers (G1L). This confirms the fact that in the XUV spectral range the radiation interacts only with a very thin superficial layer, and that the different response with respect to the 3-layer graphene is measurable by our instrument.

Until this point, the psi parameter has been retrieved with a fitting process of the intensity curves using the Stokes parameters measured with 2 Ru and 1

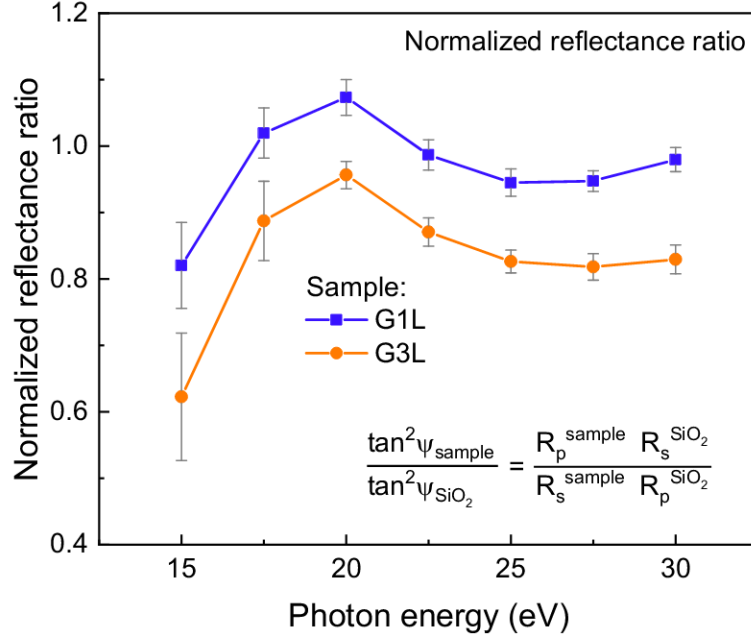


Figure 3.47: Reflectance ratios of 1-layer and 3-layer graphene normalized with respect to the reflectance ratio of SiO_2 . The error associated with these quantities is calculated as the maximum observed range of the measured values during the different experimental runs.

SiO_2 . Those values of S_1 and S_2 were obtained by fixing the refractive index of ruthenium and silicon dioxide to the values found from the fitting of the reflectivity measurements performed on BEAR. The reflectivity was measured on different spots on the samples and thus the fitting process gave us an equivalent refractive index.

We already demonstrated that by normalizing the reflectance ratio of the samples with respect to that of a reference sample, we are no longer dependent from the reflectivity of the outer mirrors, making our procedure independent from probable contamination of the optics. For the next step, our goal was to identify a method to obtain the ellipsometric parameter of the sample, ψ , without depending on the knowledge of the polarization of the input light, i.e. the Stokes parameters of the radiation used for the experiment. We want to assume a fixed polarization state of the light, for example linear horizontal polarization with a degree of polarization of 90%. Given only this information, the fitting process should return the ellipsometric parameter ψ and should be independent both from the polarization state of the light and from the reflectivities of the two outer mirrors.

The same procedure described previously, which was used to calculate the normalized reflectance ratio of Fig. 3.47, has been repeated by imposing fixed Stokes parameters across the whole energy range. The aim of this method is to demonstrate the independence of the normalized reflectance ratio from the polarization state of the input light. The procedure is performed for all 3 samples (1-graphene, 3-graphene, and SiO_2) by first fitting the intensity curves in order to retrieve the ellipsometric parameter ψ . To do this we fix the Stokes parameters to a constant value across the whole energy range, instead of using the parameters measured before and shown in Fig. 3.43 on the right. Three different values of

the Stokes parameters S_1 have been used: 0.9, 0.95, and 1. Parameter S_2 was kept fixed at 0. Once ψ is found, we proceed by calculating the reflectance ratio; this is simply performed by taking the square of the tangent of ψ , for all the samples. Finally, the reflectance ratio of graphene (both 1-layer and 3-layer) is divided by the reflectance ratio of silicon dioxide, what is obtained is what we call the *normalized* reflectance ratio of the sample under test. In Fig. 3.48 we compare the normalized reflectance ratios obtained with the 3 Stokes parameter values with the one obtained above (Fig. 3.47), for the two graphene samples.

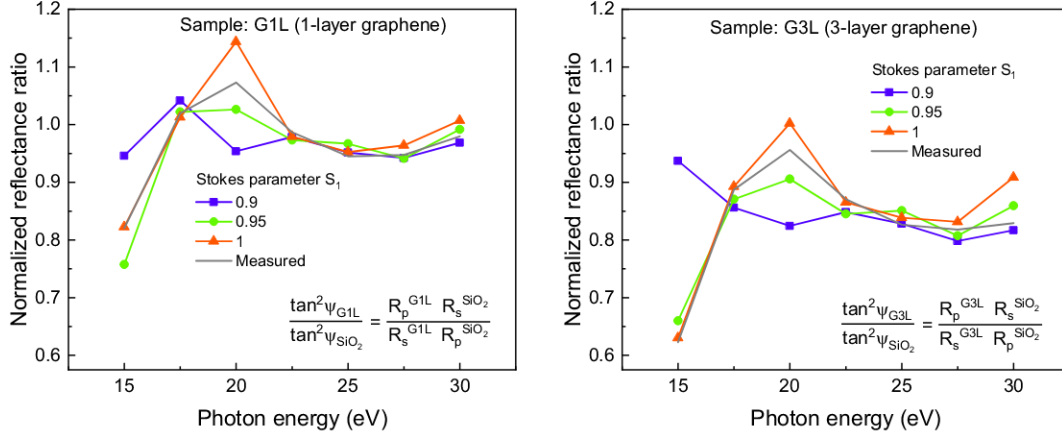


Figure 3.48: Normalized reflectance ratios for 1-layer graphene (left) and 3-layer graphene (right), obtained by fixing Stokes parameter S_1 to a constant value across the whole energy range. The grey continuous lines are the same quantities as shown in Fig. 3.47.

What is observed is that the spread of the obtained values is relatively small, indicating that the normalized reflectance ratios, which describe the polarimetric response of the samples, are insensitive to the polarization state of the light used in the experiment. It is noticed that the gray continuous line in Fig. 3.48, which is the same quantity plotted in Fig. 3.47, was obtained with the Stokes parameters of Fig. 3.43 (on the right, orange curve), while the coloured curves are obtained by fixing Stokes parameter S_1 to the constant value indicated in the legend, for the whole energy range.

Excluding the first points at 15 eV, at which a high deviation of the values is observed, the variability of the retrieved normalized ratios are in the range ± 0.0335 for G1L and ± 0.0514 for G3L (in units of the normalized reflectance ratio), averaging over all the photon energies. In terms of percentages, again excluding the points at 15 eV, the variations are within a range of 6.8% and 12.1% for G1L and G3L, respectively.

This procedure shows that, regardless of the (constant) S_1 value employed for the fitting process, at least for values in the range 0.9–1, the obtained normalized reflectance ratios vary by a relatively small amount, indicating that the retrieved parameter is actually a quantity which depends only on the optical properties of the analyzed sample, and not on the polarization of the light being used or the other 2 mirrors.

What is obtained from this normalization process is some specific information about the sample under test, without the influence of the other two mirrors and

the polarization state of the used light. This property is extremely useful because it enables ellipsometric experiments even in the case of the 2 outer mirrors presenting some optical damage, as experienced during our tests. The normalization process cancels the dependence from the 2 mirrors and from the knowledge of the polarization state for each photon energy, allowing for an easy and straightforward analysis of the acquired polarimetric data, even in the case of an unknown degree of linear polarization.

3.7 Conclusions

In this chapter I presented the work carried out for the design and the development of a reflection polarimeter to be used in the XUV spectral region. The working principle of the proposed system is based on the polarization change that incoming radiation undergoes after reflection off a metallic surface. By employing 3 consecutive reflections the polarizing effect is enhanced and, at the same time, the output beam is collinear with the optical axis, leaving the overall direction unaltered.

During the course of several beamtimes at the CiPo beamline in Trieste, the design of the polarimeter assembly has undergone substantial modifications and improvements, which have been crucial for the optimal alignment of the mirror-stage and the overall quality of the acquired Malus's curves.

The polarimeter was used to successfully align the double slits of the beamline with respect to the wiggler source, as measurements had shown that, when using the grazing incidence monochromator, the beamline was dominated by the bending emission instead of the radiation produced by the wiggler. This problem was the cause for the low degree of linear polarization and the difficulties we had encountered during the alignment process of the mirror-stage. The proposed reflection polarimeter has been an incredibly useful tool to analyze, almost in real time, the polarization state of the radiation entering the experimental chamber, demonstrating its effectiveness as a diagnostic instrument for beamlines where a fast and reliable measure of the polarization is required.

After this optimization, the polarimeter system was used to efficiently characterize the state of polarization of the CiPo beamline, across a wide range of photon energies, from 10 eV to 100 eV. We used mirrors coated in gold and ruthenium, which have a well-known behaviour in the XUV spectral range and whose refractive indexes are readily available in literature. By fixing the ellipsometric parameter ψ , a fitting process was performed on the acquired intensity curves in order to retrieve the Stokes parameters of the beamline's radiation. The fitted parameter S_1 is greater than 0.9 across the whole measured spectral range, indicating that the degree of linear (horizontal) polarization is always at least 90%.

The gold and ruthenium samples have been measured at the BEAR beamline, in order to evaluate their optical reflectance. The gold samples had already undergone some optical damage and therefore the measured reflectivity was not in good agreement with the theoretical data. A simple model made of a carbon layer on top of a gold bulk could not be confirmed by the fitting process we performed on the acquired reflectance data. The ruthenium samples have also been measured and we observed an optimal agreement between the measured reflectance and the

theoretical one, indicating that the deposited layer is indeed a high-quality layer of ruthenium, obtained with an optimized sputtering process.

After several beamtimes we noticed a performance worsening of the gold-mirror polarimeter. Simulations of the expected contrast and the fitted Stokes parameter S_1 showed that it is very likely that the mirror surface has undergone carbon contamination, which is a major problem in high-vacuum environments. Furthermore, beam-induced effects locally increase the optical damage on the surface, lowering the reflectivity and the overall contrast of the polarimeter stage, as observed in different reflectance and polarimetric measurements. A similar degradation in the measured contrast has been observed with ruthenium samples, although by a smaller amount compared to the gold mirrors.

The polarimeter was also used to measure the polarimetric response of thin films, in particular graphene (both mono-layer and three-layer) and silicon dioxide. These measurements constitute a sort of ellipsometric experiment and they are of great interest because they enable the study of the optical properties of thin films in the XUV spectral range. The acquired polarimetric curves indicate that the proposed polarimeter is able to effectively measure and discriminate between the different samples, even in the case of a mono-atomic graphene sample, as can be seen in the contrast and the ellipsometric parameter plots. Furthermore, we showed that by normalizing the response of a sample with respect to that of a reference substrate, in our case silicon dioxide, we are able to obtain a quantity which is no longer dependent on the 2 optics used in the mirror-stage (Ru in our case), meaning that the normalized curves do not depend on the reflectivities of the outer mirrors, including their probable contamination. The same measurements have been repeated to investigate the dependence of the procedure from the input polarization state. In particular, we fixed the Stokes parameters to a constant value across the whole analyzed energy range, we retrieved the ellipsometric parameter ψ , we calculated the reflectance ratio, and we normalized the ratio of graphene with respect to that of SiO_2 . What is observed is that the same reflectance ratio is obtained independently of the polarization state of the light, assuming it the same for the two measurements, at least for $S_1 \geq 0.85$. Therefore, with this procedure we demonstrate the ability of our reflection polarimeter to effectively analyze polarimetric data of different samples, in particular when combined with a procedure of normalization of the fitted ellipsometric parameter with respect to a reference sample. What is obtained is specific information about the sample under test, without the influence of the other two mirrors and the polarization state of the used light. This means that the proposed procedure is robust and suitable for cases in which the input polarization degree is not known with a high precision.

Future work concerning the ellipsometric experiments should be devoted to the development of appropriate fitting models for the polarimetric responses of the analyzed materials, in order to retrieve quantitative knowledge of the optical properties of the samples, as given, for instance, by the refractive index or the permittivity.

The research activity described in this chapter is being prepared for a journal paper which will be submitted as a peer-reviewed article in *Optics Express*, a scientific journal published by The Optical Society (OSA).

Future research in the field of XUV polarimetry should be focused on the de-

development of new kind of polarimeters for single-shot acquisition, i.e. without moving parts, unlike the system discussed in this chapter for which a complete rotation of the stage is required before obtaining the result of the polarimetric measurement. Such a “fast” polarimeter is especially useful for pump-probe experiments, where rapid information about the rotation of the polarization is required. Two configurations are already being considered. The first employs two mirrors in Kirkpatrick-Baez configuration, each of them reflecting 50% of the beam toward two photodiodes. The mirrors are mounted on two orthogonal planes at the same grazing angle. In this configuration, the polarization state is retrieved by analyzing the signals from the two photodiodes, provided the two channels are cross-calibrated. The second design needs two mirrors in Kirkpatrick-Baez configuration where each of them reflects the full beam toward the output. The mirrors are mounted on two orthogonal planes at the same grazing angle. The photocurrent generated by the XUV radiation on each of the two mirrors (which is proportional to the absorbance) is acquired. In this configuration, the polarization is derived from the two photocurrents, although the analysis model is more complex than that of the previous case, since the polarization of the radiation impinging on the second mirror will be modified by the reflection from the first mirror. The beam is transmitted to the output, where an additional diagnostic tool can be possibly installed. The two configurations are schematically depicted in Fig. 3.49.

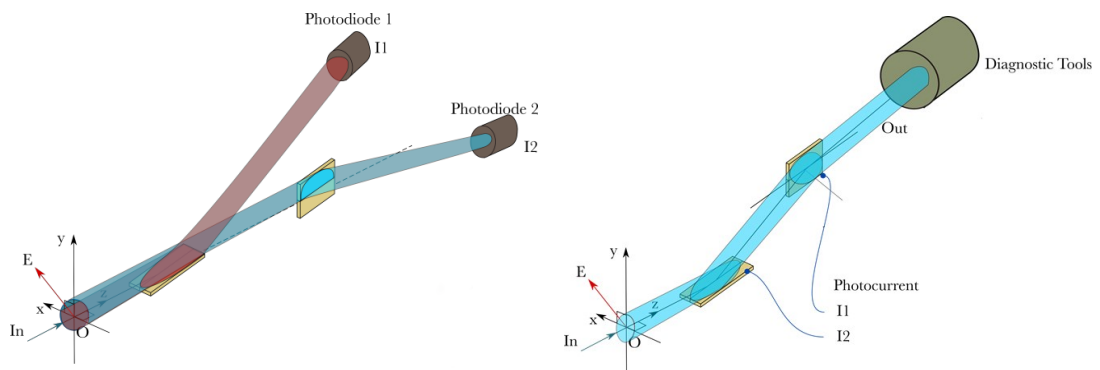


Figure 3.49: (Left) Polarimeter based on the measurement of the photon flux reflected by two mirrors in Kirkpatrick-Baez configuration, each of them intercepting 50% of the beam. (Right) Polarimeter based on the measurement of the photocurrents by two mirrors in Kirkpatrick-Baez configuration.

Chapter 4

Design and development of a deformable diffraction grating

4.1 Introduction

In this chapter the work carried out for the development of a low-cost deformable diffraction grating is presented. The proposed system has been designed to be used in a *High-Harmonic* (HH) beamline, in order to select a specific wavelength in the Extreme-Ultraviolet (XUV) spectral region, and, at the same time, to focus the radiation on the desired image point, usually where the sample has been placed.

The main advantage of such an object is the reduction of the number of optical elements needed in a monochromator of a HHG beamline. As will be explained in the next chapter, one of the most interesting research activities carried out in a HHG laboratory is the generation of ultrashort optical pulses (in the femtosecond regime) and their application to the study of ultrafast dynamical processes in materials. The selection of a single harmonic with the preservation of the pulse duration is a crucial task. The typical solution employs a monochromator with two plane diffraction gratings and four mirrors, where the second grating is used to compensate for the pulse-front tilt introduced by the first one. The four mirrors are needed for the collimation and the focus of the radiation and their role will be described in more detail in the next chapter. Such an instrument is called a time-delay compensated monochromator and uses a total of 6 optical elements. Having an object which is able to separate the different harmonics and, at the same time, to focus the radiation on a precise spot makes it possible to reduce the number of optical elements from 6 down to 3. A schematic representation of such a monochromator is depicted in Fig. 4.1.

Concave diffraction gratings are already well-established in many research laboratories working in the XUV spectral region, in particular where a single wavelength (an harmonic) has to be selected and subsequently focused onto the desired target point. The main disadvantage of a concave grating is that it has a fixed radius of curvature and thus, given fixed input and output arms, only one wavelength can be focused on the image plane. In order to focus other wavelengths, one would need to move the image plane to a different position, i.e. changing the length of the output arm, given a fixed input arm. If a fixed geometry is required, the only way to focus different wavelengths on the same output plane is to change the radius of curvature of the focusing element.

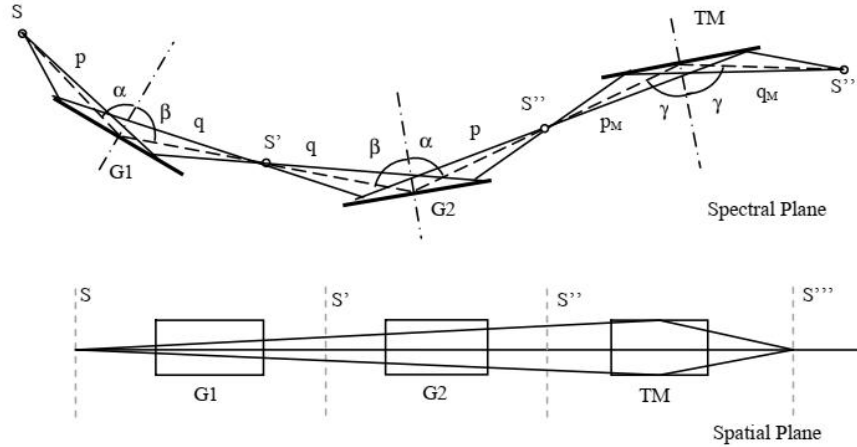


Figure 4.1: Schematic representation of a time-delay compensated monochromator realized with three optical elements: 2 deformable gratings (G1 and G2) and 1 toroidal mirror (TM).

The simplest way to introduce a variable radius of curvature is to employ a thin piece of glass, thin enough that it becomes possible to introduce a symmetric torque on both sides (something similar to [46]) and thus bend it under elastic deformation. According to classical beam theory [47, 48], the torque creates a perfectly cylindrical shape.

The idea for this work is to employ a replicated reflection grating, which is not as expensive as a mechanical-ruled grating, with a thickness of at most 2 mm such that it becomes possible to bend it, taking a cylindrical shape with a radius of curvature ranging from infinite (plane surface) down to approximately 3 m.

4.2 Experimental setup

The diffraction grating used in this experiment is a 50×15 mm replica of a mechanical-ruled reflection grating, manufactured and provided by Richardson GratingsTM (Newport Corporation).

Commercially available diffraction gratings are replicated optical components comprised of three layers: a substrate, an epoxy layer, and (usually) a reflective coating, as depicted in Fig. 4.2. Each layer meets a different purpose: (1) the metallic layer provides high reflectivity, (2) the epoxy layer holds the groove pattern and groove profile and (3) the substrate (usually glass) keeps the optical surface rigid.

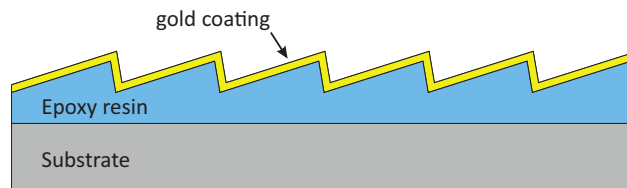


Figure 4.2: Schematic structure of a typical replicated diffraction grating.

The substrate material of our grating is a specially annealed borosilicate crown glass (known as BK-7), with a thickness of 1.5 mm, which is sufficient to bend it, without breaking it, to a radius of 3 m. The grating has a sawtooth-shaped groove profile at an angle, the so-called *blaze* angle, of 2° . On top, there is a gold coating, in order to maximize the reflectivity in the XUV spectral range. The line density, i.e. the number of grooves per millimeter, is 246 grooves/mm.

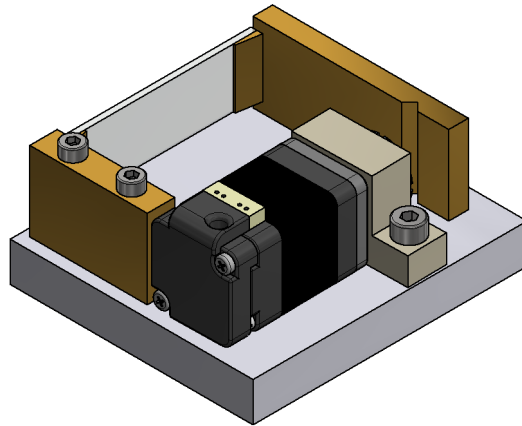


Figure 4.3: Schematic 3D representation of the grating system and the stepper-motor.

The grating is glued onto two clamps, one of which is fixed while the other is free to move on the tangential plane, i.e. the horizontal plane. The bending effect is achieved by pushing the free clamp away from the fixed one, thereby introducing a torque, which causes the grating to bend and to take a concave cylindrical shape. The clamp is moved with a micro-pusher, that is a linear actuator driven by a 2-phase stepper motor, provided by Micronix. A schematic representation of the system is seen in Fig. 4.3. The clamps and the stepper motor sit on top of an aluminum plate which, in turn, is fixed on top of a linear translation stage and a rotation stage. The first is used to move the system in the direction parallel to the normal of the grating. This is used to compensate for the difference in pointing when the grating is bent, since the bending is not symmetric with respect to the middle point of the grating. The rotation stage allows to rotate the whole system, enabling to scan for different wavelengths while keeping the input- and the output-arm fixed. This is the functioning principle of a so-called *constant-deviation* monochromator, in which the angle between the input and the output slits remains constant as the grating is rotated to scan wavelengths.

4.3 Diffraction efficiency of replica gratings

The proposed system works in the classical diffraction mount (CDM), a geometry in which the diffraction grating has uniform spaced grooves oriented perpendicular to the incidence plane. Another possible geometry is the off-plane mount (OPM), in which the grating grooves are oriented parallel to the incidence plane. The OPM is normally used in the 15–124 eV photon energy range to minimize the pulse stretch due to diffraction (typically well below 100 fs), although with medium-to-low spectral resolution ($\lambda/\Delta\lambda < 500$). The CDM, on the other side, gives a longer

time response (in the range of few hundreds of fs), but a definitely higher spectral resolution.

Since the throughput of a monochromator is dominated by the gratings' diffraction efficiency, a comparison between theoretical and experimental results has been performed for the two configurations described before. The efficiency of two pairs of blazed gold-coated plane gratings has been measured in the 41–310 eV region, in CDM and OPM, at the Circular Polarization (CiPo) beamline at ELETTRA Synchrotron, in Trieste.

As represented in Fig. 4.4, the gratings have been positioned on a X-ray reflectometer that has been installed at the output of the beamline [49]. The precision of the combined positioning of grating sample and detector (photodiode) angles is better than 0.01° . Since our application is surface physics oriented, we required a half-width beam section on the grating of about $200\ \mu\text{m}$ in order to have a compromise between a large spot, which would illuminate an area larger than the sample width at extreme grazing incidence angles, and a small spot, which would not be able to give a sum of a sufficient number of interfering wave components from the grating sample. The sample mounting inside the reflectometer allows five degrees of freedom: the three translations along the Cartesian coordinates, and the rotation around two axes: the first perpendicular to the direction of the incoming beam (for CDM measurements), and the second parallel to it (for OPM measurements). The detector can only scan along a circumference parallel to the incidence plane.

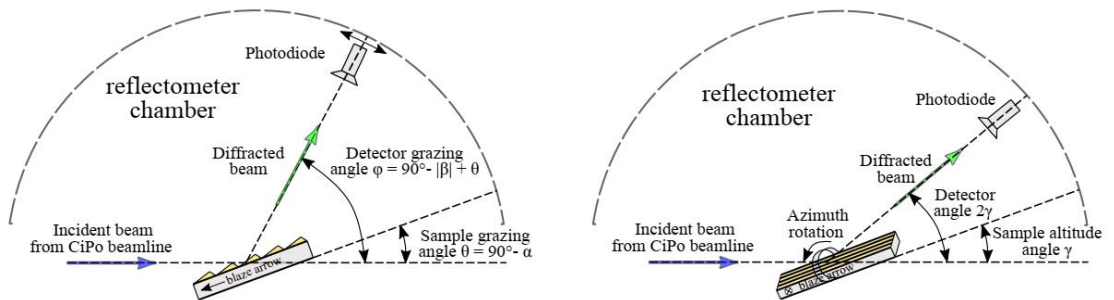


Figure 4.4: Side view of the reflectometer working principle inside the end-chamber of the CiPo beamline. (Left) Reflectometer configuration for CDM efficiency measurements. (Right) Reflectometer configuration for OPM efficiency measurements.

For each photon energy of interest, the grating has been rotated with respect to the incident beam while the full diffracted signal has been acquired through an angular scan of the detector. At each photon energy change the direct beam has been acquired in order to have a reference signal which was used for the normalization of the acquired absolute intensities. Finally, the grating efficiency was calculated as the ratio of the diffracted intensity (with background subtraction) to the incident-beam intensity.

After the efficiency measurements at CiPo, the theoretical diffraction efficiency was simulated with the aid of GSolver, which is a full vector implementation of a class of algorithms known as Rigorous Coupled Wave Analysis (RCWA). The groove profile is approximated by an ideal triangular profile and the first-order diffraction efficiency is simulated for the same photon energies used during the measurements at the synchrotron. The simulation process is explained in more

detail in [50].

In Fig. 4.5 and 4.6 the first order experimental and GSolver simulated efficiency peak values, for a set of discrete photon energies of interest, are shown.

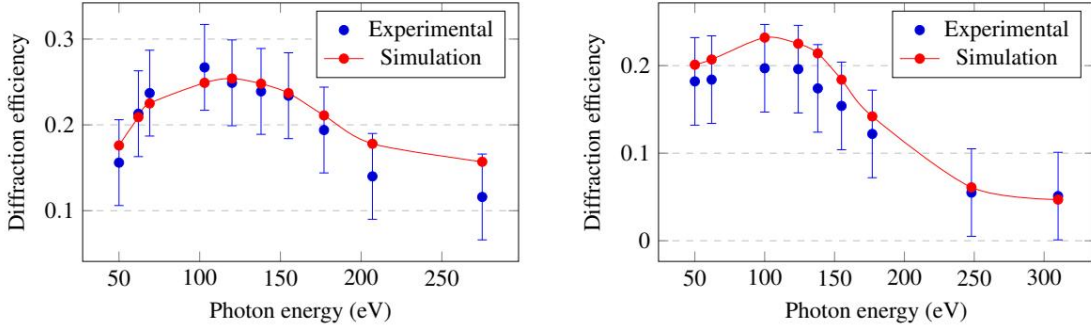


Figure 4.5: CDM first-order diffraction efficiency for two different gratings: 180 grooves/mm (left) and 600 grooves/mm (right).

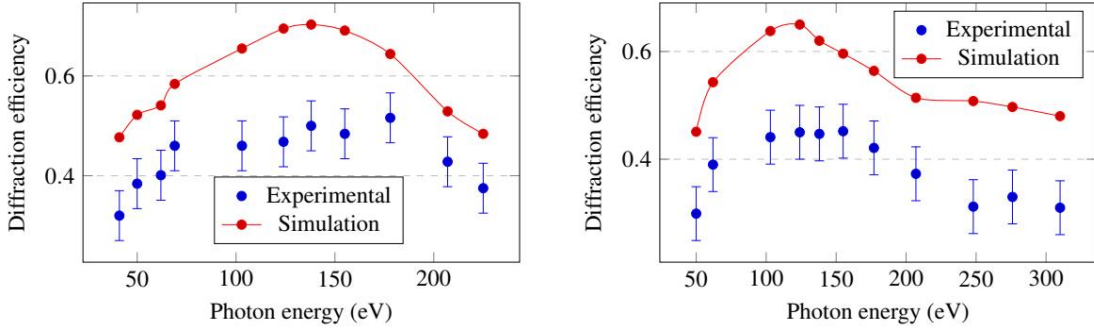


Figure 4.6: OPM first-order diffraction efficiency for two different gratings: 1800 grooves/mm (left) and 2400 grooves/mm (right).

A close agreement between simulated and measured efficiency curves has been obtained for the CDM case; the differences between the two curves are mostly attributed to the experimental random error (estimated of about 5%). Conversely in the OPM case, simulations can be considered only as an overestimation of the real efficiency, based on the assumption of an ideal saw-tooth grating profile. Since the deformable grating system will be used in the CDM geometry with photon energies not higher than 100 eV, we can conclude that for our application the replicated gold-coated gratings offer a first-order diffraction efficiency of approximately 20%.

4.4 FEA of the bending process

Before actually bending the diffraction grating, a Finite-Element-Analysis was performed to estimate the maximum curvature achievable without breaking the delicate component. The system was modelled by using two clamps and a rectangular glass plate, which should replicate the mechanical properties of the actual diffraction grating. A given force was applied to one of the clamps, while the other was attached to the “ground”. The parameter that was observed, and that served

as an indication of the stress within the glass, is the so-called *safety-factor* (SF), i.e. the ratio between the yield stress and the applied stress:

$$\text{SF} = \frac{\text{yield stress}}{\text{applied stress}}.$$

The yield is the point on a stress-strain curve that indicates the limit of elastic behavior and the beginning of plastic behavior. In brittle materials like glass, once the yield point is reached the material shows no apparent plastic deformation and fracture occurs, breaking the glass.

Having a structure with a safety factor of exactly 1 means that the applied stress is equal to the maximum allowed stress. Any additional load will cause the material to break. A structure with a SF of 2 will fail at twice the design load.

Simulations showed that a radius of curvature of approximately 3 m could be reached with a minimum SF of 2, as seen in Fig. 4.7.

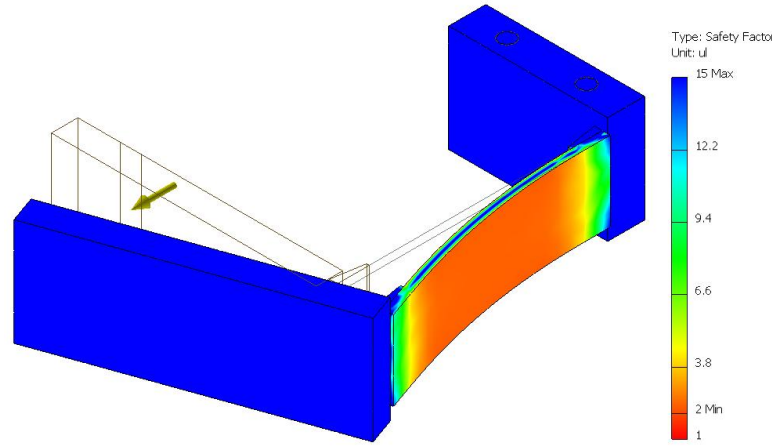


Figure 4.7: Finite element simulation of the bending process. The color gradient represents the Safety Factor, showing a minimum value of 2 in the central part of the glass (the deformation is exaggerated for visualization purpose.)

4.5 Manual bending tests

After the FEA simulations, a mechanical structure for the manual bending of test substrates has been developed. The system is composed of two clamps which hold the test substrate and two manual adjustment screws which are used to push the clamps apart, thus causing the substrate to take a cylindrical shape. The assembly is depicted in Fig. 4.8. The substrates that have been used for the tests are rectangular plates of poly-Si, which have a similar Young's modulus of BK-7 glass, and therefore are the ideal substrates to bend, before employing the more expensive diffraction grating.

The system was installed in an optical setup, similar to that described in Section 4.6, to retrieve the radius of curvature while the substrate was bent. During several tests the material would always break at a radius of curvature between 2.5 m and 3 m, which led us to the conclusion that the actual grating could perform in a similar way, reaching a radius of no less than 3 m.

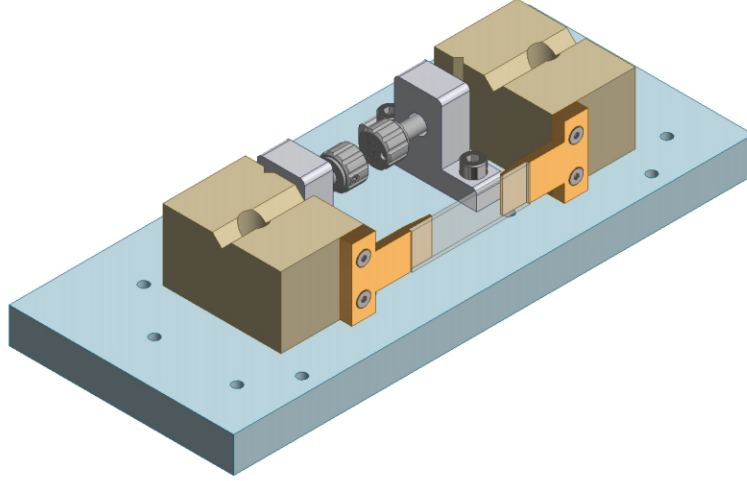


Figure 4.8: CAD model of the mechanical assembly for the preliminary bending tests.

4.6 Focusing properties with zero-order light

The first tests of the motorized system were performed with a He-Ne laser beam. The objective was to test the focusing ability of the deformable grating by using the zero-order light (reflected light), and, moreover, to perform a calibration of the stepper motor, in order to map different curvatures of the grating with the corresponding stepper motor positions.

The setup consists of a He-Ne laser, a 100 μm pinhole, which causes diffraction and thus acts as the source point, an iris, in order to limit the accepted light-cone, the deformable grating system, and a beam profiler to monitor the size and shape of the reflected light at the image plane.

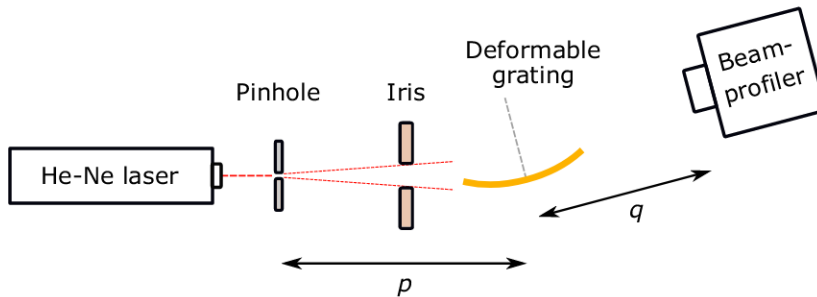


Figure 4.9: Schematic drawing of the visible-light experimental setup.

The equation that relates the different parameters of the setup is the equation of the tangential focus in the case of spherical surfaces:

$$\frac{1}{p} + \frac{1}{q} = \frac{2}{R \cos \alpha} \quad (4.1)$$

where p is the input arm, i.e. the distance between the entrance slit (the pinhole) and the middle point of the grating, q is the output arm (the distance between the

grating and the tangential focal spot), R is the radius of curvature of the grating, α is the incidence angle, i.e. the angle between the input arm and the normal to the grating surface. Since we are looking at the reflected light, α is also the angle between the normal and the output arm. For our experiment we fixed p at 80 cm and α was set to 80° . For different values of the radius of curvature, the focal plane position (q) varies following Eq. (4.1), as can also be seen in Fig. 4.10.

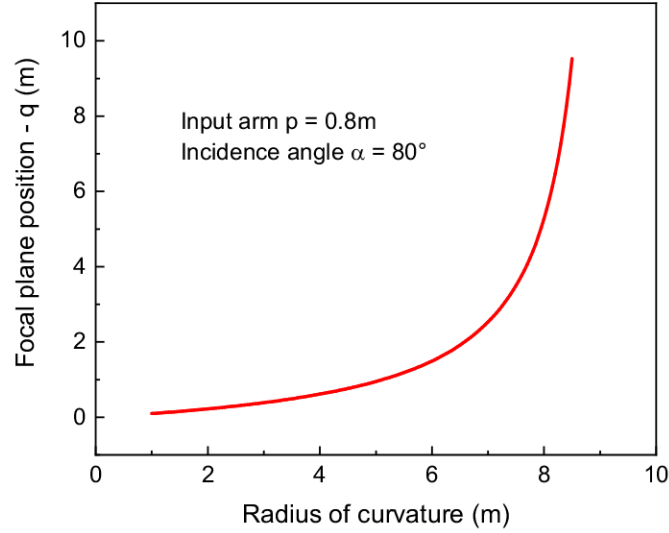


Figure 4.10: Theoretical focal plane position vs. radius of curvature, calculated with Eq. (4.1)

The calibration of the stepper motor was performed by fixing the image plane, i.e. the position of the beam profiler, at a certain distance q from the grating. By fixing p, q and α there is only one possible value for the radius of curvature R , as can be seen from Eq. (4.1). The motor was moved, causing the grating to bend, until the spot on the image plane was seen to be on focus. The best focus was chosen to be the one where the horizontal width of the spot (the one on the tangential plane) was lowest. At this point the absolute number of steps of the motor was recorded.

4.7 Focusing properties in the XUV

In order to test the deformable grating system in the XUV spectral range, a vacuum experimental setup has been employed. The XUV light source is a hollow-cathode lamp which can be used with noble gases like helium, neon or argon to generate some specific spectral lines. Immediately after the lamp there is a vertical slit, which acts as the entrance slit. The grating system is fixed inside a vacuum chamber, after an iris which limits the accepted light-cone. On the output arm there is a filter and a thermoelectrically cooled back-illuminated CCD, for the direct detection of XUV radiation. As mentioned before, the grating works as a constant-deviation monochromator, meaning that the angle between the input- and output-arm remains constant. What moves is the grating itself; it is rotated in order to scan for different wavelengths. The deviation angle was chosen to be 163° , while the input-arm and the output-arm are both 70 cm. The main parameters of the XUV experiment are summarized in Table 4.1.

input arm (p)	700 mm
output arm (q)	700 mm
deviation angle (k)	163°
entrance slit aperture	100 μm \times 5 mm
grating's groove density (σ)	246.16 gr/mm

Table 4.1: Main experimental parameters for the XUV measurements.

The diffraction and the focusing properties of the system are described by a set of equations:

$$\begin{cases} \frac{\cos^2 \alpha}{p} + \frac{\cos^2 \beta}{q} = \frac{\cos \alpha + \cos \beta}{R} \\ \sin \alpha - \sin \beta = m\sigma\lambda \\ \alpha + \beta = k \end{cases} \quad (4.2)$$

where α and β are the angles between the normal to the grating and the input- and output-arm, respectively; p and q are the lengths of the input and output arms; R is the radius of curvature of the grating; m is the diffraction order, σ is the line density of the grating; λ is the wavelength of the radiation in the m^{th} diffraction order; k is the (constant) deviation angle. Fig. 4.11 shows the input and output angles, along with the diffracted orders. It is worth noting that in the zero-order case (simple reflection, $m = 0$) we have $\alpha = \beta$ and the first equation in (4.2) becomes Eq. (4.1).

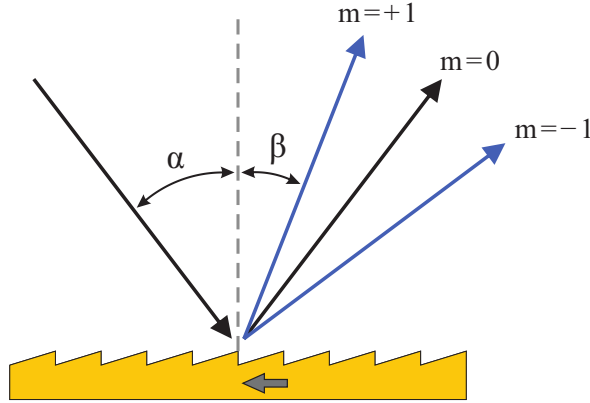


Figure 4.11: Schematic view of the two angles and the diffracted orders, together with the blaze arrow.

Using the sum-to-product trigonometric rule, the second equation, i.e. the one relating the angles with the wavelength of the diffracted light, can be rewritten as:

$$2 \sin \left(\frac{\alpha - \beta}{2} \right) \cos \left(\frac{\alpha + \beta}{2} \right) = m\sigma\lambda,$$

and using the third relation it becomes

$$2 \sin \left(\alpha - \frac{k}{2} \right) \cos \left(\frac{k}{2} \right) = m\sigma\lambda. \quad (4.3)$$

Eq. (4.3) relates the input angle α with the wavelength of the diffracted radiation in the m^{th} order, given a constant deviation angle k and line density σ .

To test the focusing ability of the deformable grating, we looked at the zero-order radiation and at different spectral lines, and acquired CCD images at different radii of curvature. Since the system works as a constant-deviation monochromator, we chose to always direct the focused light towards the center of the active area of the sensor. In order to observe different spectral lines, the grating must be rotated by an angle which is found with Eq. (4.3). In the special case of the zero-order radiation, the grating acts as a mirror, m is zero, and thus $\alpha = k/2$.

The gases that were used are helium and neon. With He we looked at the lines at 30.3 nm and 58.4 nm while with Ne we focused the lines at 46.1 nm and 74 nm. The neon lines are actually two pairs of very close spectral lines, the first pair consists of the wavelengths 46.07 nm and 46.24 nm, while the lower energy pair is at 73.6 nm and 74.4 nm.

When we started the experiment, with Ne, the grating was already glued with the blaze arrow pointing towards the output, meaning that the diffraction order with the highest efficiency was $m = -1$, and therefore the grating had to be rotated to a smaller incidence angle (input arm closer to the grating normal). Conversely, when switching to He, the grating was turned with the blaze arrow towards the input arm. For this reason, the most intense diffraction order was $m = +1$ and the grating had to be rotated to a more grazing geometry. Table 4.2 shows the angles at which the system has to be rotated in order to direct the required spectral line towards the CCD, and the required radius of curvature needed for the focusing. As can be seen, the values of α , for the helium spectral lines, become closer to 90° with respect to the zero-order case, while with Ne it's exactly the opposite.

	λ (nm)	α	R (m)
	Z.O.	81.5°	4.74
He	30.3	82.95°	4.61
	58.4	84.29°	4.29
Ne	46.1	79.30°	4.45
	74	77.97°	4.05

Table 4.2: Incidence angles and radii of curvature for different spectral lines.

As done with the He-Ne laser, different images were taken, one for each different radius of curvature. The process is repeated for each spectral line of interest. The CCD was cooled down to 0°C , in order to reduce the thermal noise and to get cleaner images. A single CCD image is a matrix of 1300×1340 pixels, with each pixel occupying 2 bytes, meaning that the range of possible values goes from 0 to 65535.

To reduce the read-out time and to improve the signal-to-noise ratio, the images were *binned*, i.e. a cluster of pixels is combined into a single (larger) pixel. In our case, we used a binning size of 2×1 , meaning that the charges of two vertical adjacent pixels are combined (summed) together, producing a 650×1340 pixels image. In spectroscopic images, where the image of a spectral line typically has a high aspect ratio, i.e. the line is very long and thin and orientated perpendicular to

the readout register, CCD binning provides the best signal-to-noise ratio without any deterioration in spectral resolution.

On each image the pixel values were summed vertically, along the columns of the matrix. What is obtained is a one-dimensional profile curve of intensity values vs. horizontal position on the sensor (in pixels), as seen in Fig. 4.12, where the CCD images and the 1-D profiles of the Ne lines around 46.1 nm are shown, for two different radii of curvature.

It can be noticed that there is a substantial glow on the left side of the spectral lines, even in the on-focus position (image on the right in Fig. 4.12). This effect is ascribed to the coma aberration, which is always present in a spherical optic element working off-axis, i.e. when the incoming rays strike the mirror in grazing incidence.

On the profile plot, the peak corresponding to the observed spectral line was identified, and the full-width at half-maximum (FWHM) was calculated. This quantity is the parameter which is used to evaluate the focusing properties of the system and thus it is plotted as a function of the steps of the linear actuator.

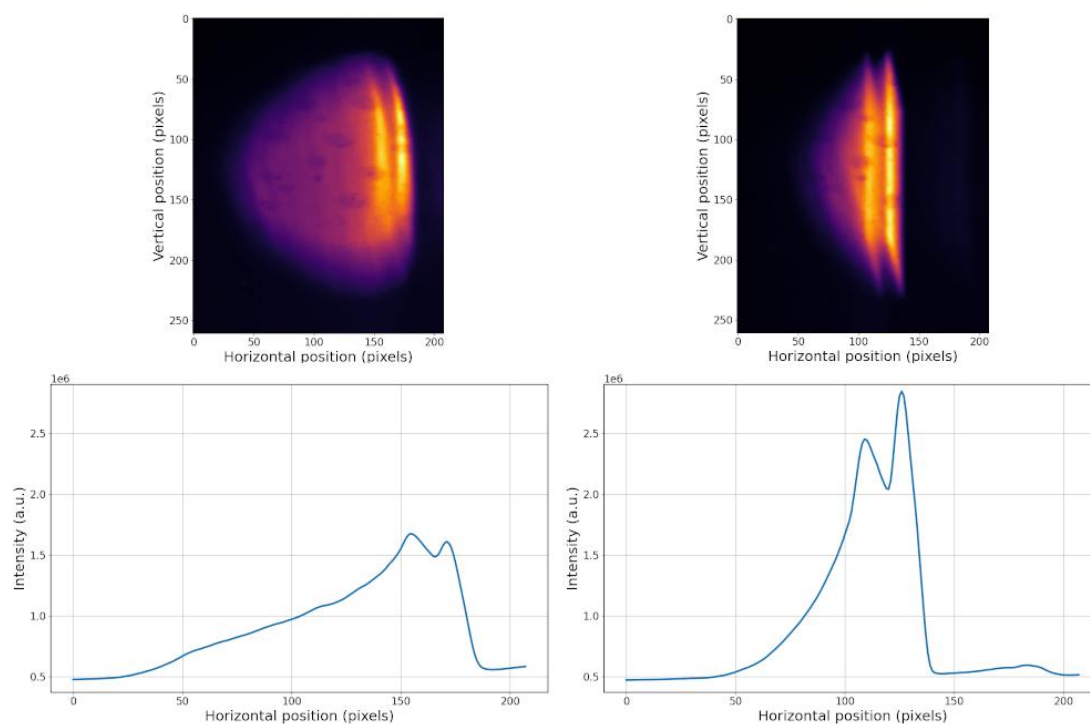


Figure 4.12: (Top) CCD images of the 46.1 nm spectral lines of Ne (actually two very close lines at 46.07 nm and 46.24 nm) taken with two different radii of curvature: 5.5 m (out of focus) on the left, and 4.45 m (on focus) on the right. (Bottom) One-dimensional profiles obtained by summing along the columns of the CCD images.

In Fig. 4.13 and 4.14 the focusing curves, i.e. the FWHM values plotted with respect to the motor steps, are shown for the zero-order radiation and the two spectral lines, for helium and neon. The fact that the FWHM values decrease, reaching a minimum, and then increase again, shows that there is a specific point where the diffracted spot has a minimum lateral width, meaning that it is effectively focused by the deformable grating. The FWHM values for the Ne spectral

line at 74 nm are significantly higher than the other ones because we are actually observing two very close lines, and thus the FWHM is the width of the combined profile of the two lines.

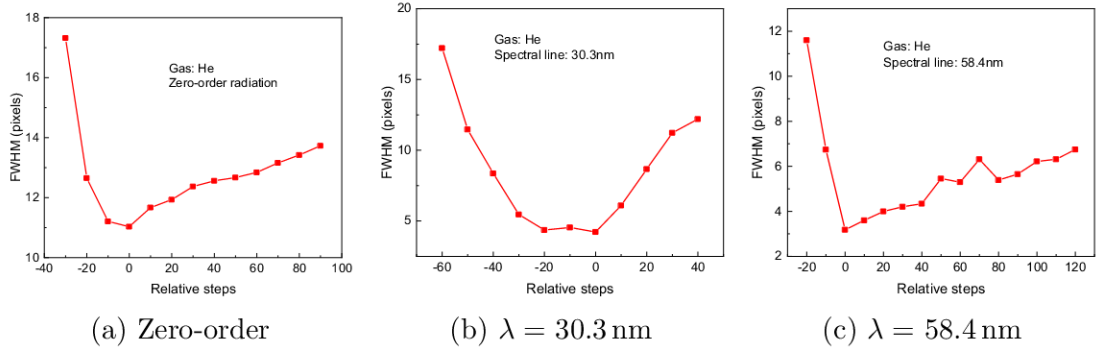


Figure 4.13: Helium focusing curves.

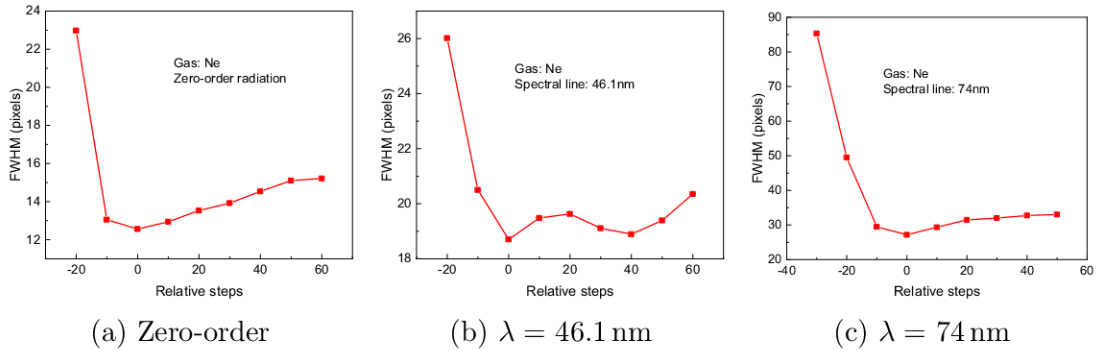


Figure 4.14: Neon focusing curves.

On the other hand, the FWHM values obtained with helium are smaller since both wavelengths are actually single spectral lines. Here, some considerations about the resolution of the instrument can be made. By looking at the focusing curves of He we observe that the minimum value of FWHM is reached for the spectral line at $\lambda = 58.4$ nm, for which we have $\text{FWHM} \approx 3$ pixels. The CCD image and the spectral profile of the selected line of He are shown in Fig. 4.15. Since each pixel of the CCD camera is $20 \mu\text{m}$ wide, the width of the focused spectral line on the detector is $\Delta l = 60 \mu\text{m}$.

Now by fixing the incidence angle α in the grating equation (second equation in (4.2)) and differentiating with respect to λ , the angular dispersion, D , or change in diffraction angle per unit wavelength can be determined as:

$$D = \frac{\partial \beta}{\partial \lambda} = \frac{m \sigma}{\cos \beta} \quad (4.4)$$

For a given order m , the angular dispersion represents the ability to discriminate between signals at different wavelengths.

The wavelength dispersion on the focal plane of an instrument, for example at the position of the detector, is usually specified as the reciprocal linear dispersion, given in nm/mm. Being q the distance from the grating to the detector (the length

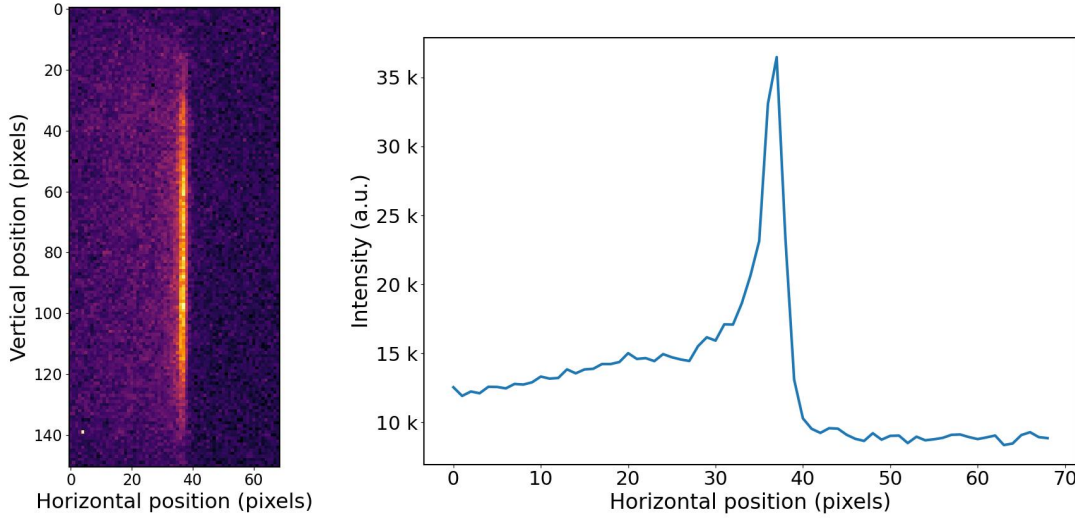


Figure 4.15: Spectral line of helium at $\lambda = 58.4\text{ nm}$ in the on-focus condition ($R = 4.29\text{ m}$). Acquired CCD image (left) and summed 1-D profile (right).

of the output arm), the reciprocal linear dispersion, L_D , is given by:

$$L_D = \frac{\partial\lambda}{\partial x} = \frac{\cos\beta}{m\sigma q} \quad (4.5)$$

From Table 4.2 we see that for the He line at 58.4 nm we need an incidence angle $\alpha = 84.29^\circ$, which corresponds to a diffraction angle $\beta = k - \alpha = 78.71^\circ$. By putting this value in Eq. (4.5) we get $L_D = 1.136\text{ nm/mm}$. If we multiply this value by the width of the spectral line on the camera we get the wavelength dispersion of the selected line: $\Delta\lambda = L_D \Delta l = 0.0682\text{ nm}$. Finally, we are able to calculate the resolution of the proposed instrument, which indicates the separation ($\Delta\lambda$) between two spectral peaks that can just barely be detected as separate with the instrument. The resolution, or resolving power, is a dimensionless number defined as

$$R = \frac{\lambda}{\Delta\lambda} = \frac{58.4}{0.0682} = 856. \quad (4.6)$$

The calculated value of the instrument resolution is relatively high for a HHG application, where usually a high dispersion is not needed, but instead it is required to select one harmonic, or a subset of it, with a sufficient photon flux to perform the experiments. Typically, a resolving power of $\Delta E = 100\text{ meV}$ at $E = 30\text{ eV}$ is required, which corresponds to $R = 300$.

If we suppose to employ the deformable grating system in a monochromator for a HHG application, we could be more “conservative” and assume to work with a $100\text{ }\mu\text{m}$ exit slit and a grating-detector distance of 500 mm , in order to get a more compact geometry. In this configuration, for the same wavelength of above ($\lambda = 58.4\text{ nm}$), we would get a resolution of $R = 365$, which is a reasonable value considering the requirements of a HHG beamline.

4.8 AFM analysis

The diffraction grating has been analyzed with an *Atomic Force Microscope* (AFM) on an area of $50\text{ }\mu\text{m} \times 50\text{ }\mu\text{m}$, in order to verify the line-density and to evaluate the

surface quality of the coating. In Fig. 4.16 the three-dimensional topography of the analyzed portion of the grating is shown. In Fig. 4.17 we show the acquired (2-D) surface plot and a horizontal cross-section profile. The average groove distance, measured as the distance between two consecutive peaks or valleys of the surface profile, is $4.05\ \mu\text{m}$, which is exactly the inverse of the groove density of the grating (246 grooves/mm).

The 1-dimensional profile is then fitted with piece-wise linear slopes, in order to approximate an ideal triangular (sawtooth) profile. The so-called roughness profile is obtained by subtracting the fitted model from the original data, as shown in Fig. 4.18. Two parameters, which are typically used in surface analysis, are retrieved from the surface roughness profile: the arithmetic average, R_a , and the root-mean-square value, R_q

$$R_a = \frac{1}{l_r} \int_0^{l_r} |z(x)| dx \quad (4.7)$$

$$R_q = \sqrt{\frac{1}{l_r} \int_0^{l_r} z(x)^2 dx} \quad (4.8)$$

where l_r is the length of the analyzed profile section and $z(x)$ is the (1-D) roughness profile as a function of the x -position.

We measured a R_a of $3.71\ \text{nm}$ and a R_q of $4.76\ \text{nm}$.

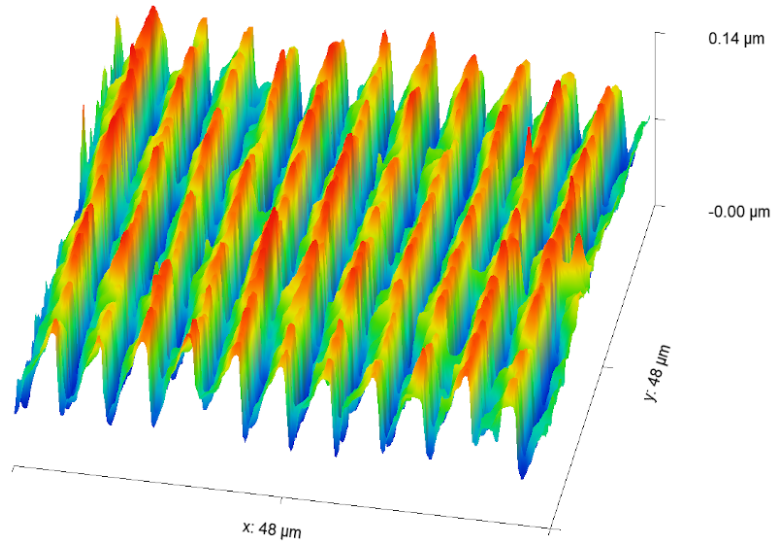


Figure 4.16: 3D AFM topography ($48\ \mu\text{m} \times 48\ \mu\text{m}$) of the grating surface.

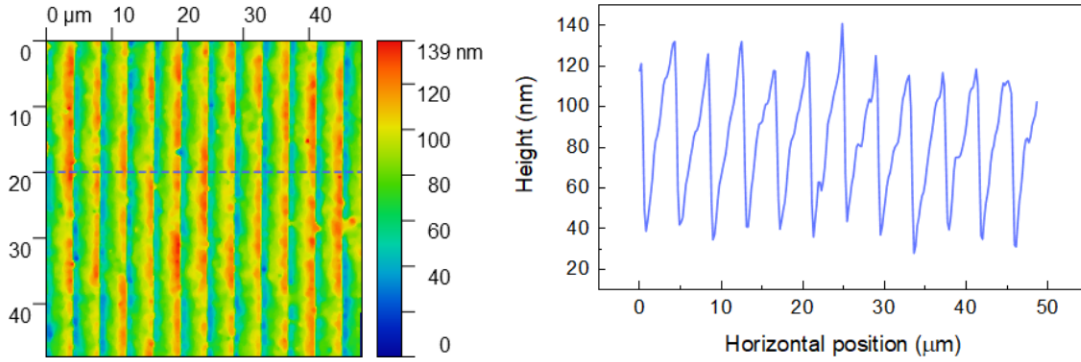


Figure 4.17: (Left) Pseudocolor plot of the AFM raster scan of the diffraction grating. (Right) Horizontal cross-section of the surface profile corresponding to the blue dashed line on the left.

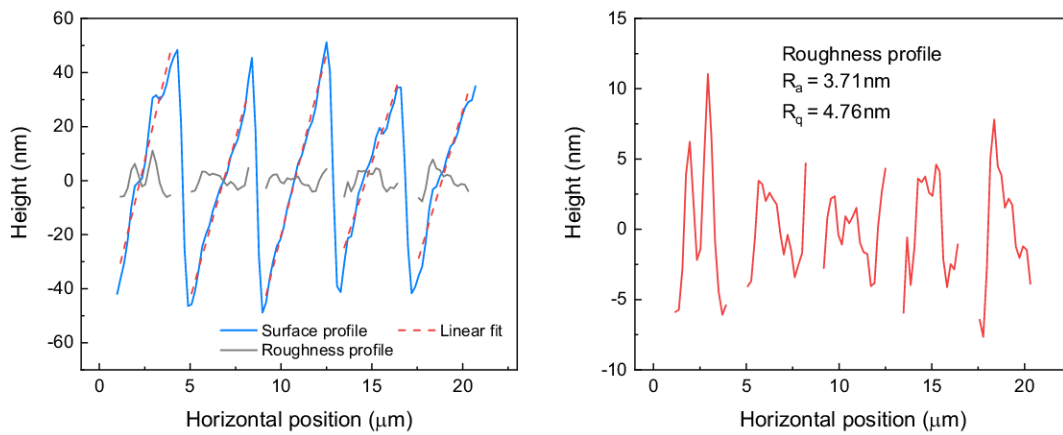


Figure 4.18: (Left) Measured surface profile with linear fitting slopes and the obtained roughness profile. (Right) Roughness profile obtained by subtracting the fitted model from the original data. On this profile the arithmetic average, R_a , and the root-mean-square value, R_q , are calculated.

4.9 Aberration analysis with wavefront sensor

After the test of the system in the XUV spectral range, we performed an analysis of the surface shape, for different radii of curvature, by measuring the wavefront distortion that the curved surface introduces. In particular, by illuminating the surface under test with a plane wave (a collimated laser beam), and by measuring the wavefront phase of the reflected wave with a wavefront sensor (WFS), it is possible to reconstruct the surface profile. This technique is typically used in adaptive optics (AO) applications in order to correct optical aberrations that otherwise would limit the performance of the optical system. In an AO system aberrations are corrected by measuring the wavefront phase with a wavefront sensor and optically conjugating it with a deformable mirror (DM), as seen in Fig. 4.19. These two elements are connected to a control system which, in order to perform an optimal correction, must work in real-time and have a low latency to achieve a cutoff frequency higher than the aberration bandwidth.

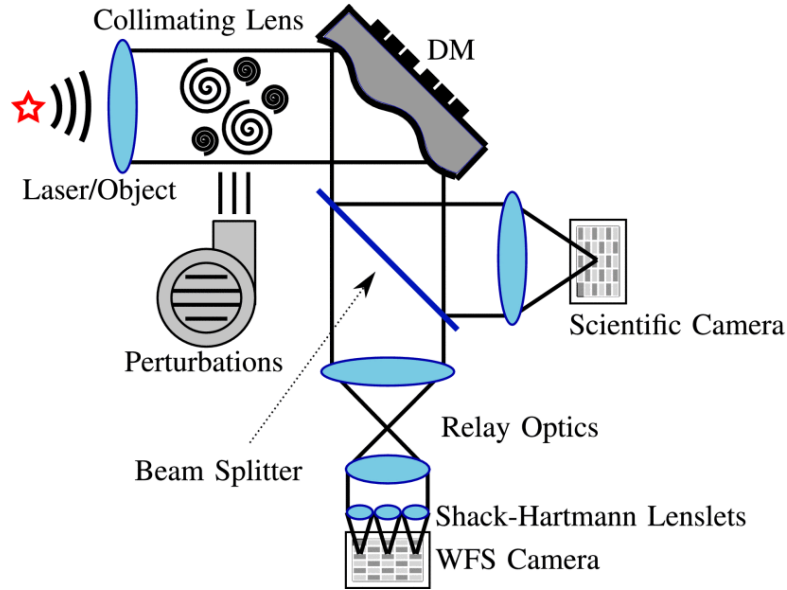


Figure 4.19: Simplified schema of an AO system: a light source (laser or scientific object) is observed on a Scientific Camera after the correction with DM. The wavefront distortion is measured by a WFS whose lenslets are optically conjugated to the DM by means of a relay optics.

4.9.1 Wavefront measurement

A Shack-Hartmann WFS is the most commonly used device to determine the wavefront shape by measuring its local gradients. In this device, the wavefront of the incoming optical beam is spatially sampled with an array of P lenslets. Each lenslet $p \in P$ focuses a portion of the light beam on a spot within the area \mathbb{A}_p of the photosensitive pixel array (typically a CCD or CMOS camera), as shown in Fig. 4.20.

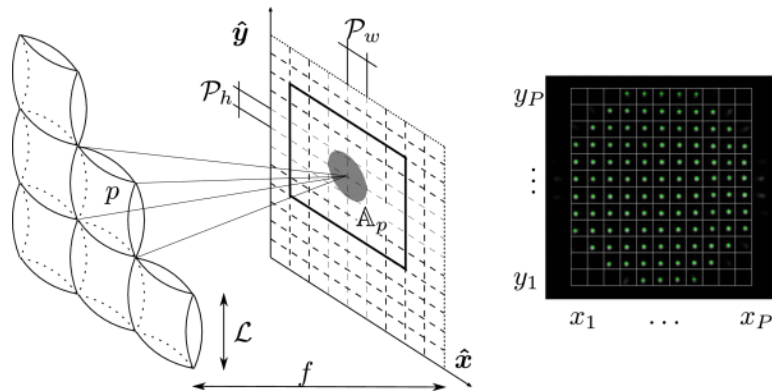


Figure 4.20: (Left) Shack-Hartmann WFS working principle. Each lenslet p focuses a portion of the incoming light on the pixels area \mathbb{A}_p . The position of the light spot is related to the wavefront local gradient and the lenslet focal f . (Right) Example of Shack-Hartmann spots as seen by the camera.

According to light refraction, the wavefront gradient of the p th lenslet along the Cartesian coordinates x, y is related to the spot's centroid position. Therefore, the wavefront over the whole optical aperture can be reconstructed by determining

the positions of all the centroids. A center of gravity (CoG) algorithm, which exploits the Gaussian intensity distribution of the p th lenslet spot, can be used to find the centroid positions. The wavefront is then reconstructed by projecting the slopes on a suitable base (modal reconstruction). This is usually performed using the Zernike polynomials, an orthonormal basis over a circle of unitary radius commonly used to represent circular wavefront aberrations [51]. The wavefront phase $\phi(x, y)$ can be approximated for any $(x, y) \in \mathbb{S}$ Cartesian point, within the circular support $\mathbb{S} = \{(x, y), x^2 + y^2 \leq 1\}$, as the sum of a N -terms Zernike series

$$\phi(x, y) = \sum_{n=1}^{\infty} w_n Z_n(x, y) \simeq \sum_{n=1}^N w_n Z_n(x, y) \quad (4.9)$$

where w_n is the coefficient of the n th Zernike mode Z_n .

4.9.2 Experimental setup

The setup needed for the wavefront measurement is simpler than the AO system discussed above, as no deformable mirror is needed. The light coming from a single emitter laser diode (Thorlabs CPS670, $\lambda = 670$ nm, power 4.5 mW) is collimated to create a point-like source at infinity. A beam-splitter directs a part of the beam toward the diffraction grating while the other part is reduced in size by a telescope and directed to the WFS. The diameter of the beam at the grating is 22 mm but since the grating has a dimension of 50×15 mm, only the central part of the grating (approximately 22×15 mm) is actually observed. The WFS camera is a USB 3.0 global-shutter CMOS type monochromatic sensor with square pixel size $\mathcal{P}_w = \mathcal{P}_h = 5.86 \mu\text{m}$ manufactured by the *iDS* company. The lenslet array has lenslet pitch $\mathcal{L} = 150 \mu\text{m}$ and focal $f = 6.4$ mm. The area \mathbb{A}_p is 25×25 pixels. Spot images are transferred as 8-b integer matrices representing the quantized pixel intensity I . In Fig. 4.21 a schematic representation of the experimental setup is depicted. On the left the calibration of the system is shown, in which the beam-splitter is rotated to direct the beam to a reference mirror, i.e. a mirror whose surface profile is assumed to be perfectly plane. Once the calibration is performed, the system works in the configuration seen on the right of Fig. 4.21.

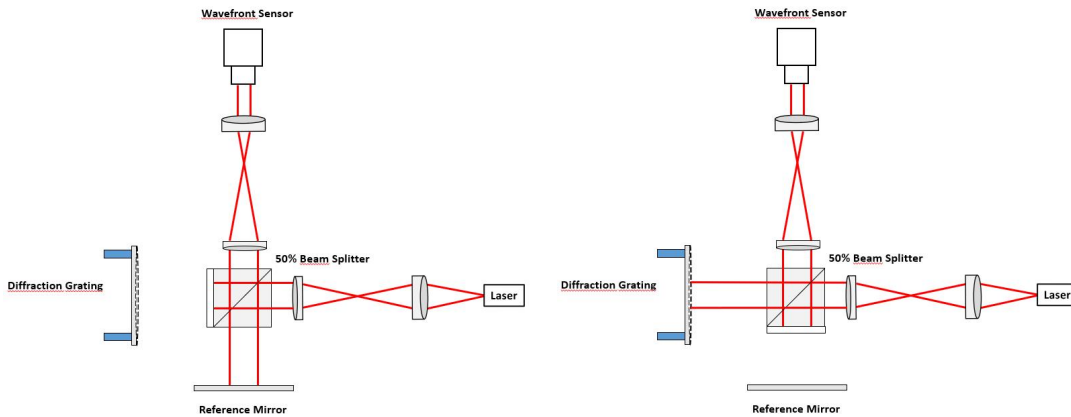


Figure 4.21: Schematic view of the experimental setup. System calibration using a reference mirror (left), measurement of the distorted wavefront caused by the diffraction grating (right).

4.9.3 Results

The grating has been bent from the plane condition ($R = \infty$) down to 8 m, measuring the reflected wavefront and reconstructing the grating surface. In Fig. 4.22 we show the reconstructed surfaces (only the illuminated portion of the grating) for decreasing values of the radius of curvature, from $R = \infty$ down to 8.7 m.

For every analyzed radius of curvature, the reconstructed slope has been fitted with the Zernike polynomials and their coefficients are plotted against the radius of curvature of the grating, in order to show how the bending affects the surface profile.

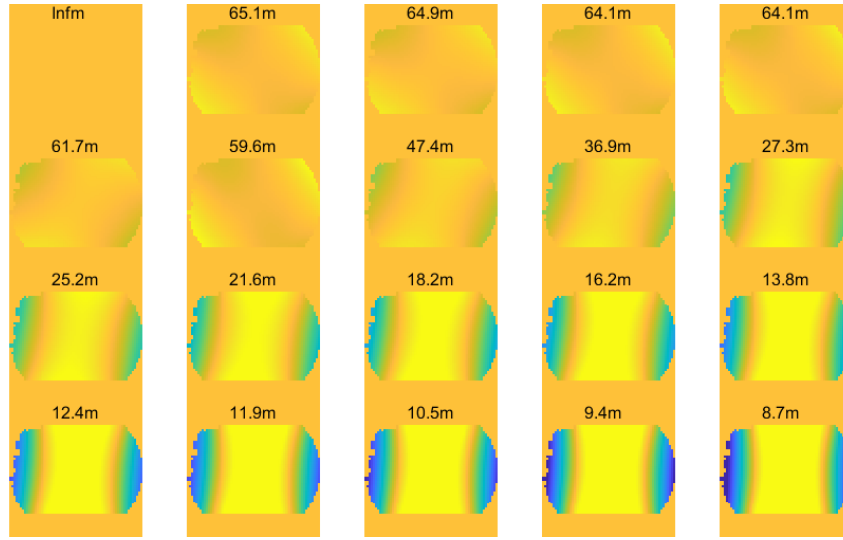


Figure 4.22: Reconstructed surface profiles of the illuminated portion of the grating, for decreasing values of the radius of curvature.

In Fig. 4.23 we show the coefficient related to the astigmatism in the tangential plane (Astigmatism X) and the coefficient linked to the defocus aberration, plotted against the radius of curvature of the grating. It is clearly noticed that both aberrations are approximately zero for high radii (plane, unbent, condition) and they increase in magnitude as the radius decreases (grating is more bent). Together, the two aberrations describe a cylindrical wavefront, which is compatible with the bending process on the grating. Specifically, it takes both the Astigmatism X and the Defocus to obtain a pure cylindrical surface which focuses the incoming radiation on the tangential plane. The plot on the right of Fig. 4.23 shows the ratio of the two aberrations as a function of the radius of curvature. Except for the first points at high radii, the values tend to remain constant as the radius is decreased. This confirms the fact that the analyzed surface bends taking a cylindrical shape, which is the desired outcome that we aim to achieve with the proposed deformable grating system.

In Fig. 4.24 the astigmatism in the orthogonal direction (Y, in the sagittal plane) is shown for the different radii of curvature. In the plane condition (high curvature radius) the coefficient of the Astigmatism Y has a small value of approximately $-0.25 \mu\text{m}$ that remains almost constant until $R \approx 20 \text{ m}$; further bending causes the astigmatism to decrease, reaching zero at the last radius ($R = 8.7 \text{ m}$). The sagittal astigmatism described here is clearly an unwanted effect, as it describes a surface which is twisted, introducing a deformation into an otherwise

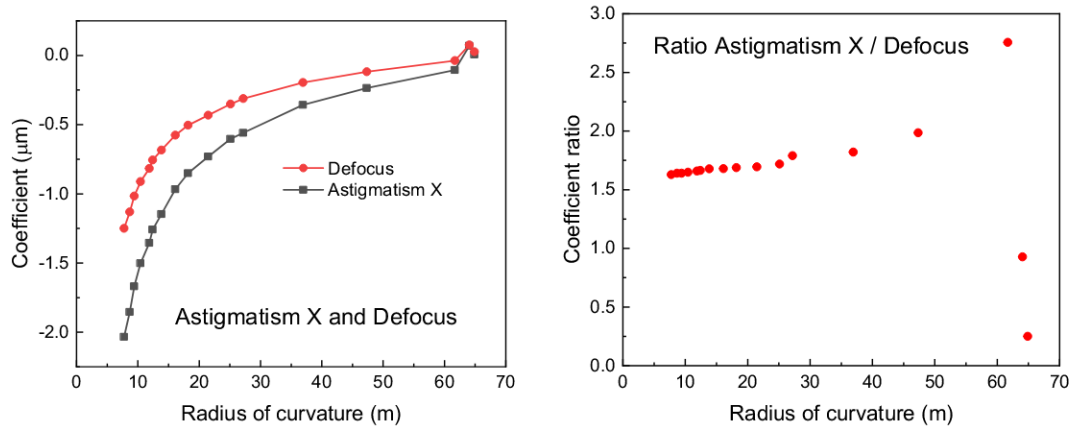


Figure 4.23: (Left) Astigmatism X and Defocus aberration plotted against the radius of curvature. (Right) Ratio between Astigmatism X and Defocus.

pure cylindrical surface. The presence of this aberration, even at high radii of curvature (plane condition), is ascribed to the gluing process of the grating, which could have introduced a slight torsion to the substrate. The other reason for this sagittal astigmatism could be due to the cylinder of the linear actuator pushing in a slightly off-centered position, thus introducing a torsional effect on the bending. It is observed, however, that the Astigmatism Y decreases in magnitude as the radius is decreased, meaning that, as the bending process proceeds, the effect of this aberration becomes gradually negligible.

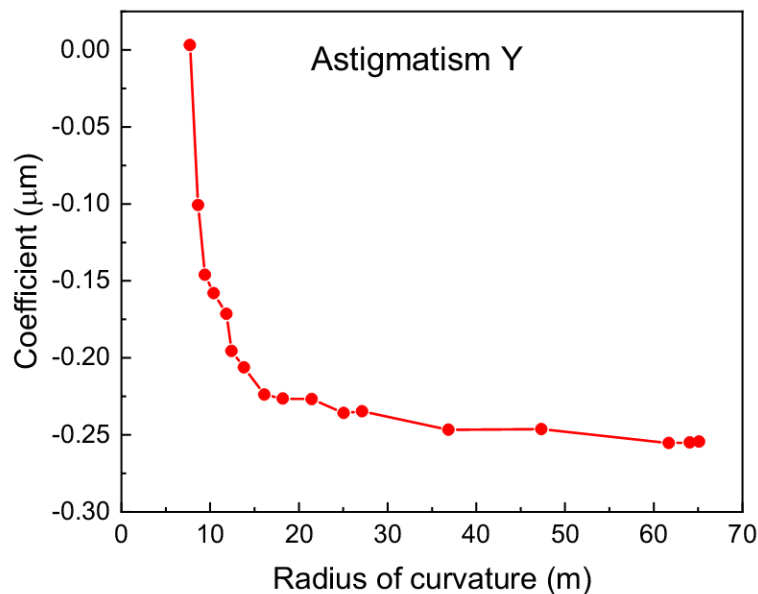


Figure 4.24: Astigmatism Y vs. radius of curvature.

In Fig. 4.25 all the fitted coefficients are plotted together as a function of the radius of curvature. The predominant effect is observed for the Astigmatism X and the Defocus, which are the two Zernike modes needed to obtain a pure cylindrical shape. The only undesirable contribution is the one given by the Aberration Y (blue curve), which, nevertheless, is seen to go to zero for increased bending.

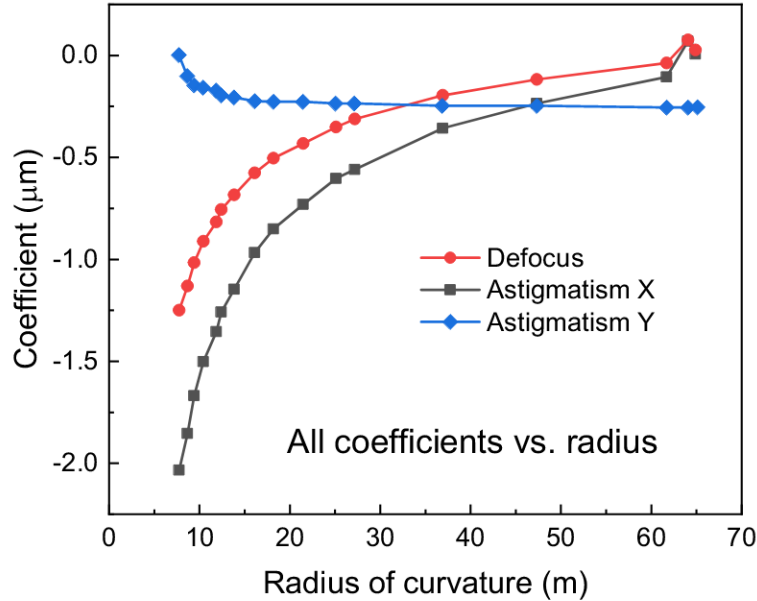


Figure 4.25: All the coefficients plotted against the radius of curvature.

4.10 Conclusions

In conclusion, we have presented a low-cost deformable diffraction grating that can be used to select a specific harmonic line in the XUV spectral region and, at the same time, to focus the radiation on the desired image plane (in the same position for all wavelengths). Despite the use of a low-price commercially-available replica grating, with a total cost of the whole system of no more than 10 000 € (the replicated grating has a cost of less than 2000 €), we demonstrate the outstanding capabilities of the proposed solution, which makes it very appealing to budget-tight laboratories.

A preliminary Finite-Element-Analysis showed that a radius of curvature of 3 m could be reached without breaking the material. Subsequently, a mechanical structure for manually bending test substrates has been realized. The radius of curvature has been retrieved with an indirect measurement, in which a divergent He-Ne laser beam is directed onto the (reflecting) substrate and the distance of the focal plane is measured. By employing the tangential focus equation for spherical surfaces, given the input and output arms and the incidence angle, the radius of curvature can be easily calculated.

Using a constant deviation-angle configuration, as typically found in monochromators and spectrometers, the system has been tested in the XUV spectral range by using a hollow-cathode lamp with He and Ne characteristic spectral lines. These measurements demonstrate the ability of the grating to bend from a plane condition down to approximately 3 m, effectively dispersing and focusing the radiation onto the image plane. The measured resolution of the instrument is particularly suitable for being employed in a monochromator for the spectral selection of high-harmonics in a HHG beamline.

An AFM analysis has been performed, which gave us a close-up look on the grating surface and its grooves. The replicated ruling pattern proved to be of high quality and the measured surface roughness is less than 5 nm. The surface

smoothness, and thus the optical quality of the system, could be enhanced only by employing a master grating, with the major downside of its high cost (>10 000 €).

A wavefront distortion measurement has been carried out in order to evaluate the performance of the bending system in obtaining a cylindrical surface. The measured wavefront slopes were fitted with the Zernike polynomials and the obtained coefficients were plotted as a function of the radius of curvature. Increasing the bending of the grating, both Astigmatism X and Defocus are seen to increase in magnitude and their ratio remains constant, indicating that the surface bends in a pure cylindrical shape. The orthogonal Zernike mode (Astigmatism Y) is very low when the substrate is plane, indicating a probable torsional effect due to the gluing process, and is observed to decrease as the bending proceeds.

The next planned activity involving the proposed deformable grating system is a study of the stress and the reliability of the grating, observing for potential adhesion losses of the resin layer. The stress experiment will be carried out by repeatedly bending (and unbending) the grating with the motorized system and a dedicated control software. One thing to notice, however, is that for the final application as part of a monochromator the system will work only in a specific wavelength range (20 nm to 90 nm, corresponding to energies 62 eV to 13.8 eV), meaning that the grating will remain almost always in the bent condition, and only small adjustments of the curvature radius could be made in order to focus a different wavelength in the above-mentioned spectral range. As an example, with the same grating parameters used in our experiment, wavelengths $\lambda = 20$ nm and $\lambda = 90$ nm are focused with a radius of curvature of $R = 4.68$ m and $R = 3.79$ m, respectively. These are the two extreme values of curvature radius that the grating will experience, thus any adjustment made inside this working range will be relatively small and should not cause any stress to the grating. It is highly advisable to avoid frequent bending cycles from the plane condition ($R = \infty$) to the nominal radius, as this introduces large amounts of stress inside the substrate, causing potential breaking of the glass or the detachment of the resin layer. Nevertheless, the system will be tested also under this aspect, in order to get quantitative knowledge about the maximum strain that can be applied to the grating before losing its functionality.

Future activities and research should eventually be devoted to the development of a time-delay compensated monochromator made of 3 optical elements instead of 6, by employing 2 deformable diffraction gratings and 1 toroidal mirror for the focusing effect in the sagittal plane. The system will be installed as part of a HHG beamline, where harmonic selection and the compensation of the pulse-front tilt are crucial tasks for the optimal generation of ultrashort XUV pulses.

The research activity described in this chapter is going to be submitted as a peer-reviewed article in *Optics Express*, a scientific journal published by The Optical Society (OSA).

Chapter 5

Upgrade of a time-delay compensated monochromator

The third activity in which I have been involved is the upgrade of a time-delay compensated monochromator employed in a High-order Harmonic Generation (HHG) beamline at the Polytechnic University of Milan.

In Milan there is a well-established research activity in the field of ultrashort light pulse generation and the application of these pulses to the study of ultrafast phenomena in matter. The research activity concerns the development of new laser sources for the generation of ultrashort optical pulses (in the femtosecond regime) and their application to the study of dynamical processes in materials.

The natural time scale of molecular dynamics, and therefore for the building and breaking of chemical bonds, is in the femtosecond domain ($1 \text{ fs} = 10^{-15} \text{ s}$). The observation of chemical or biological transformations therefore typically requires measurements with femtosecond time resolution. Such observations are only possible with correspondingly short pulses, which then allow the photo-induced initiation of a process of interest using a short “pump” laser pulse, followed by a stroboscopic observation after a well-defined time delay, using an equally short “probe” pulse.

The electronic motion, can occur on much faster, attosecond time scales ($1 \text{ as} = 10^{-18} \text{ s}$), taking as reference the 152 as orbital period derived from the Bohr atomic model of hydrogen. Until recently, direct measurements on these time scales were impossible. However, two ultrafast, XUV and x-ray sources are the new leading sources of the last decade, namely HHG discovered in 1961 by Franken et al. [52] and free-electron lasers (FELs) invented by John Madey in 1971 [53]. They are able to provide time-resolved access to processes that are happening into the attosecond domain.

In HHG, an intense femtosecond infrared (IR) laser is focused on an atomic or molecular gas. The XUV radiation can then be produced at laser frequencies that are odd, and in some cases very high multiples of the driver laser frequency. Only in 2001, it has been demonstrated that attosecond XUV pulses can be created through HHG [54, 55].

The research carried out in Milan exploits state-of-the-art technologies and methodologies in the field of lasers, with important implications in non-linear optics, optical communications and material diagnostics. The main research projects are:

- Generation of few-optical-cycle laser pulses for extreme non-linear optics applications (generation of high-order harmonics);
- Attosecond pulses and related technologies;
- Application of femtosecond pulses to the study of electronic state dynamics in low-dimensional materials, such as nanoparticles, polymers and in general carbon-based nano-structured materials;
- Ultrashort laser sources tunable from the near-infrared to the visible and ultraviolet, for spectroscopical applications with high temporal resolution;
- Scanning Near-Field Optical Microscopes (SNOM) with high spatial and temporal resolution for nano-optical applications.

The involved beamline is a laboratory for XUV ultrafast spectroscopy called *FEXRAYS*. The aim of this laboratory is the experimental investigation, with femtosecond temporal resolution, of ultrafast processes in atoms and molecules excited by pulses in extreme ultraviolet spectral range (XUV) generated through the High-order Harmonic Generation process. A single harmonic is selected with a monochromator compensated in time (that allows for preserving the temporal duration of the given harmonic) characterized by a high photon flux and good spectral tunability. Such pulses are used to study ultrafast processes in atoms and molecules with pump-probe techniques. The laboratory is equipped with several instruments for detecting ions and electrons generated after the interaction with XUV pulses, such as a Time of Flight spectrometer (ToF) for electrons and ions and a Velocity-Map Imaging spectrometer (VMI).

The driving source of the beamline is a Ti:sapphire amplified laser system which generates 35 fs pulses with an energy of 6 mJ and repetition rate of 1 kHz. A fraction of the amplified femtosecond laser (1.2 mJ energy per pulse) is then sent to a hollow fiber compressor for the generation of 5 fs pulses with an energy of 0.8 mJ. The remaining beam is used for the generation of ultrashort pulses in the ultraviolet spectral region by means of non-linear processes.

5.1 High-harmonic generation in gases

High-harmonic generation (HHG) in gases is a process in which a high intensity ($10^{13} - 10^{15} \text{ W cm}^{-2}$) infrared (IR) laser pulse is focused on a noble gas jet (typically He, Ne and Ar). Such intensity is already comparable with the static Coulomb field experienced by an outer-shell electron in an atom, therefore the light-matter interaction can not be seen as a perturbative process anymore. This highly nonlinear interaction with the conversion medium generates a train of sub-femtosecond bursts every half-optical cycle of the driving IR laser field. When detecting the radiation emitted on the laser axis, the measured spectrum is made up of discrete peaks at the multiple odd frequencies of the IR laser frequency, the so-called harmonic frequencies. The intensity of the first harmonic orders decreases quickly. However, they are followed by a plateau region with almost constant intensity and a cutoff energy with exponential decrease. Extremely high orders have been generated since the plateau has been shown to extend until the keV range [56].

The underlying physics can be understood with a semi-classical model in three separate steps [57–59]. The whole process is laser driven and thus fully temporally and spatially coherent. Moreover, the HHG broadband spectrum should result in attosecond pulses if the different harmonics are perfectly phase-locked [60]. The unique properties of HHG have found applications in different research fields such as the study of ultrafast phenomena in matter and the study of molecular and even electronic motion. They represent a powerful tool for temporal resolved measurements with sub-femtosecond resolution, with the enormous advantage of being a tabletop source. They can also be used as a seed for Free Electron Lasers (FEL) in order to improve their temporal coherence [61], and they can be applied to coherent lensless diffraction imaging of nanostructures with a spatial resolution of few tens of nanometers [62].

5.2 Femtosecond XUV beamline

Instrumentation capable of maintaining the few-femtosecond, or even attosecond, time scale of HHs generated pulses is needed in order to perform high-resolution pump-probe experiments and for maximizing the instantaneous power during chemical interactions. In particular, the selection of a single harmonic with the preservation of the pulse duration is a crucial task.

Harmonic spectral selection can be obtained with the use of a normal incidence multilayer mirror, which does not alter the pulse duration up to fractions of a femtosecond [63]. Although high efficiency performances and a wide range of focalization schemes, the main drawback is the lack of tunability, and therefore the necessity of using different optics to cover a wide spectral region. One possible solution to the last requirement is the use of an ordinary diffraction grating. In this case, the diffraction mechanism itself is the main effect that alters the duration of the pulse, since the pulse-front of the incident radiation is tilted after the diffraction by the difference of the optical paths of rays at the same wavelength diffracted by adjacent grating grooves. This effect generates a pulse-front tilt that can be considered negligible for picosecond or longer pulses, but it is dramatic for femtosecond ones. In fact, as an order-of-magnitude estimate, a grating illuminated for a length of 10 mm with 1200 grooves/mm uses $N = 12\,000$ grooves. At a wavelength of 10 nm, for the first diffraction order ($m = 1$), the optical path difference is $\Delta_{OP} = Nm\lambda = 120\,\mu\text{m}$ which corresponds to a time delay of $\Delta t = \Delta_{OP}/c \approx 400$ fs. Nevertheless, it is possible to design grating monochromators that do not alter the temporal duration of the ultrashort pulses by using two gratings in a subtractive configuration to compensate for the temporal and spectral dispersion. This solution is the one adopted in Milan and it is called time-delay compensated (TDC) configuration.

To obtain the maximum possible diffraction efficiency the so-called *off-plane* mount (OPM) configuration was adopted. It consists of a first mirror which collimates the light on a plane diffraction grating with uniform spaced grooves oriented almost parallel to the incidence beam, and a second mirror acting as a focusing element on a horizontal exit slit placed on the image plane. The mirrors have equal incidence angles and unity magnification in order to minimize aberrations at the output. The grating performs the wavelength selection through the rotation



Figure 5.1: Picture of the laboratory for XUV ultrafast spectroscopy (FEXRAYS beamline).

around an axis which is tangent to the grating surface, passes through its center, and is parallel to the grooves. The exit slit has to be placed horizontally since the diffracted orders are distributed over a semi-cone. A typical OPM configuration is shown in Fig. 5.2.

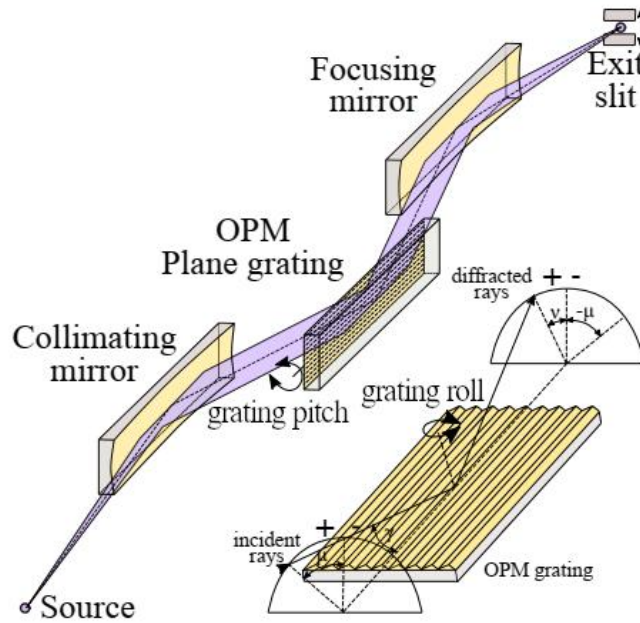


Figure 5.2: Layout of a plane-grating monochromator in OPM geometry.

As explained before, a single grating introduces necessarily a pulse-front tilt because of the diffraction, therefore the temporal resolution gets worse after the monochromator. A monochromator with zero front-tilt requires the use of at least two gratings in the compensated configuration. The design of a time-delay compensated monochromator (TDCM) in the OPM geometry requires four toroidal mirrors and two plane gratings, as shown in Fig. 5.3. The first mirror collimates the light coming from the entrance source point; the first grating, G1, is operated in parallel light, then the second mirror, T2, focuses the diffracted light on the exit slit. The light coming out of the slit is now monochromatized and the pulse-front is tilted. The second section compensates for the pulse-front tilt, therefore

the number of grooves illuminated on G2 has to be the same as G1. Since the gratings are typically identical and are operating at the same altitude angle, this condition is fulfilled with a symmetrical configuration, i.e. $q_1 = q_2$. Furthermore, in order to minimize the aberrations, each of the two sections is operating with unity magnification, i.e. the input arm of the collimator is equal to the output arm of the successive focusing element. The wavelength scanning is provided by rotating the gratings around an axis passing through the grating center and parallel to the groove direction. The last mirror of the second section is also demanded to focus the radiation onto the output image point.

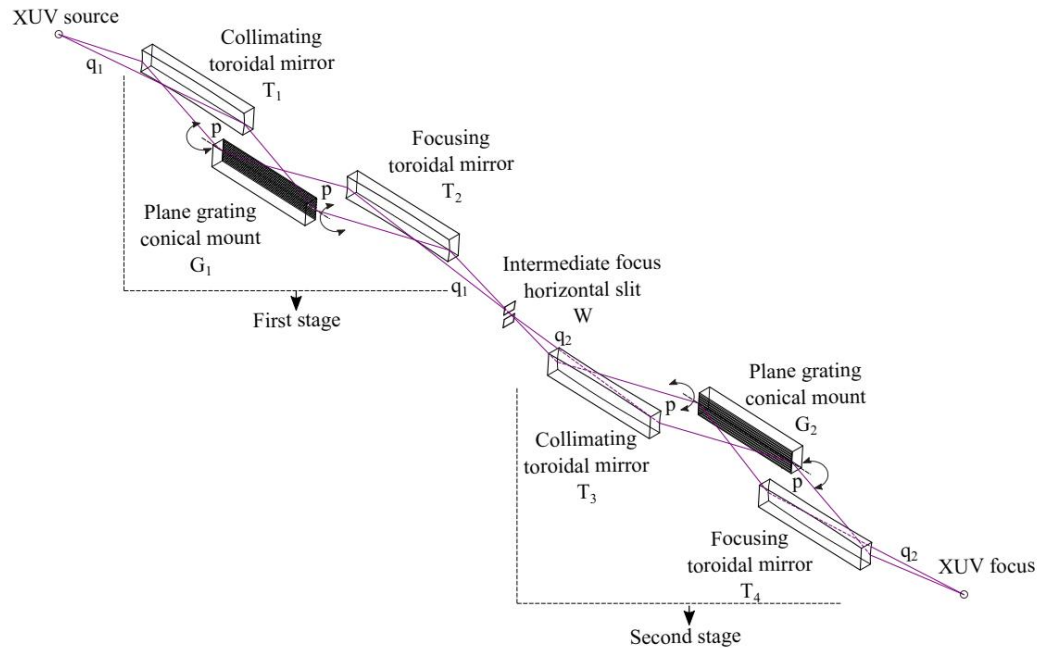


Figure 5.3: Layout of a double-grating TDC monochromator in the OPM geometry.

5.3 Upgrade of the monochromator

Before the upgrade, the monochromator consisted of 6 optical elements (4 mirrors and 2 gratings) mounted on manual alignment holders, except for the gratings which were installed on top of rotation stages in order to allow for the wavelength scan. The upgrade introduced several important features:

- Interchangeable gratings on both sections. There are two gratings available for each stage: one for the low-energy and one for the high-energy spectral range;
- Introduction of a new degree of freedom for the grating stages. Each section allows for the independent regulation of the grating *roll*, i.e. the rotation about an axis which passes through the center of the grating and is normal to the surface;
- Possibility of remotely controlling all three rotational degrees of freedom of the last toroidal mirror;

- Introduction of a beam-stabilization system performed with a He-Ne laser beam running parallel to the XUV beam.

The new features required the design of the mechanical holders and alignment stages, together with a control software to remotely regulate all the different degrees of freedom introduced with the upgrade.

The gratings are mounted on top of a motorized stage which offers 3 independent, decoupled motions: the rotation for the wavelength scanning, the linear movement for the grating selection, and the roll, needed for the precise alignment of the grating grooves with respect to the incoming light direction. The same structure is replicated for the second stage.

The first three mirrors, T1, T2, and T3 in Fig. 5.3, are mounted on manual alignment holders, which allow for the regulation of all the rotational degrees of freedom, namely the yaw, the pitch, and the roll. These are set during the installation phase and are not meant to be changed during the normal operation of the monochromator.

The last mirror, instead, is provided with vacuum motorized stages, which allow the remote control of the mirror-pointing at any time during the run-time of the instrument. This is needed because each of the two gratings has a slightly different pointing, meaning that the selected harmonic is focused in different positions on the image plane. To compensate for this effect, the last refocusing mirror enables a fine correction of the output direction, mainly by acting on the yaw and the pitch, which move the output spot on the image plane in the horizontal and vertical direction, respectively. Moreover, there could be small misalignments of the system on a day-to-day basis, typically due to variations of the infrared input beam pointing, which is aligned with the aid of two distant irises.

Another important feature added to the instrument is the active correction of the beam stability. As explained before, in the femtosecond regime it is of fundamental importance to avoid any time delays or pulse-front tilts, otherwise the extreme short duration of the XUV pulse is compromised. The system of 6 optical elements inevitably introduces some deviations from the nominal optical path length, in the order of few nanometers, and that causes the loss of phase coherence between the XUV pulse and the driving IR field. The main concern comes from possible vibrations introduced by the vacuum turbo-pumps. These vibrations could transmit to the mirrors and the gratings, and could have a detrimental effect on the ultrashort XUV pulse duration.

In order to measure the variations in the optical path length, thus being able to compensate for them, a cross-correlation measurement has been exploited. The idea is to employ a tiny mirror that is fixed to each of the optical element holders, about 20 mm higher than the XUV optical axis, making it affected by the vibrations in the same way as the XUV optics are.

In order to monitor the vibrations on the tiny mirrors, a helium-neon laser is used. The He-Ne beam is divided in two by a beam-splitter; one part of the beam is sent into the vacuum chamber and travels 20 mm higher than the XUV beam, being reflected at each of the 6 optical elements by one tiny mirror; after the last mirror the beam is sent back outside and is spatially recombined with the second part of the He-Ne beam, which traveled in a straight line outside the chambers. The spatial overlapping of the two light-beams creates interference fringes that

are observed with a simple beam-profiler, and that are analyzed to evaluate, and eventually correct, the vibrations.

5.4 Control software

The main activity in which I have been involved in Milan has been the development of the control software for the new double-stage monochromator. The software should consist of a user-friendly graphical user interface that allows for the complete control and management of the monochromator. It should offer a manual control section, from where all the motors of the optical elements can be moved independently; it should also allow for a higher level mode of operation, in which the user is able to select the desired harmonic from a list of pre-saved wavelengths, and the software automatically moves all the required elements in order to focus the desired harmonic onto the image plane.

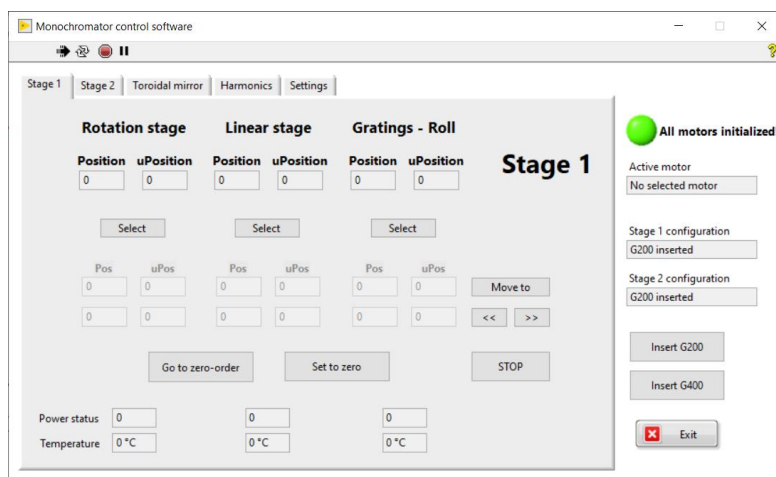


Figure 5.4: Screenshot of the “Stage 1” tab of the graphical user interface developed for the control of the upgraded monochromator.

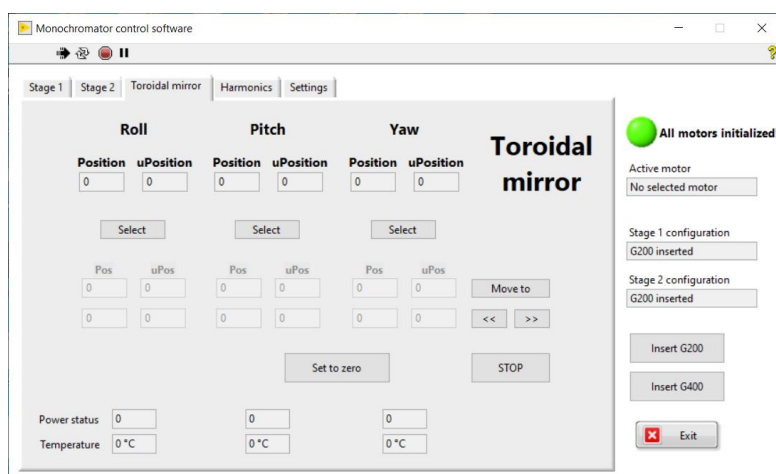


Figure 5.5: Screenshot of the “Toroidal mirror” tab, showing the three independent motor controls.

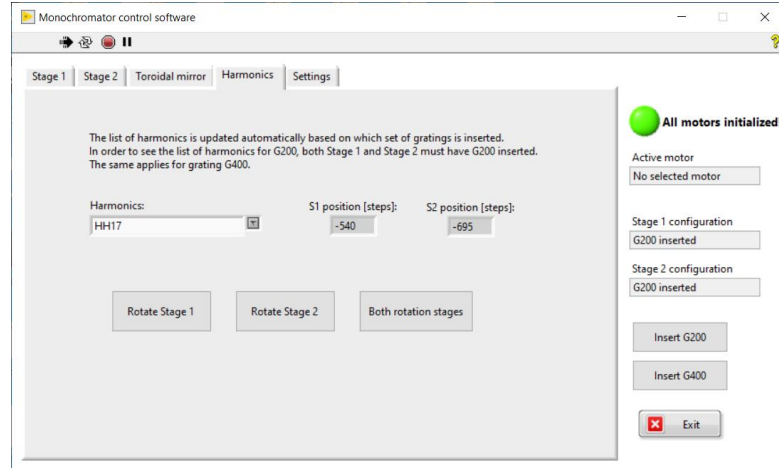


Figure 5.6: Screenshot of the “Harmonics” tab, showing the drop-down menu with the different available harmonics.

As can be seen in Fig. 5.4, the user interface offers different tabs: Stage 1, Stage 2, Toroidal Mirror, Harmonics, and Settings. The first three tabs are, clearly, for the “manual” operation of the motors in the two grating stages and the last refocusing mirror. Inside Stage 1 and 2 the user finds the controls and the indicators of the three possible movements: the grating (scanning) rotation, the linear motion, and the roll. The software shows the actual position of the motors and lets the user send the commands for a relative (incremental) or absolute positioning. All the positions are expressed in terms of *steps*, as the actuators are all driven by stepper motors.

There are certain saved positions, like the zero-order positions, one for each stage, and the positions of the linear stages that correspond to the working positions of the two gratings, G200 and G400.

The “Harmonics” tab offers the possibility of selecting a specific harmonic wavelength and to send the appropriate command to all the motors needed to focus the desired wavelength onto the image plane. A drop-down menu shows all the available harmonics, the list is updated automatically based on which set of gratings is inserted. In order to see the list of harmonics for G200, both Stage 1 and Stage 2 must have G200 inserted. The same applies for grating G400. Once a specific harmonic is selected, the user can choose to move the required motors of both stages or only those of one of the two stages. All the positions (the steps) required for the different motors to select and focus a specific harmonic wavelength are saved into a configuration file (.ini file) which can be opened from the “Settings” tab.

5.5 Efficiency characterization

The upgraded monochromator has been tested by generating High Harmonics and observing the resulting spectra in different working configurations of the two stages. The gas used for the HHG was Argon, with a pressure of 1.3 mbar in the generation cell. The pulse duration was ~ 50 fs with a power of 550 mW. The spectrum of the HHG process is observed with a grating spectrometer that employs

on its focal plane a microchannel plate (MCP) 2D detector. The spectrometer is installed after (down-beam) the monochromator and serves as a diagnostic tool to optimize the harmonic generation process. Indeed, with both stages rotated on their zero-order position, all the generated harmonics are acquired simultaneously by the spectrometer, allowing for a fast optimization of the generation parameters.

We observed the 17th and the 23rd harmonic lines, corresponding to photon energies of 26 eV and 35.2 eV, respectively. In Fig. 5.7 we show the acquired MCP image and the one-dimensional profile obtained by vertically summing the intensity values of the image. The image was taken with both stages on their zero-order position, thus showing all the generated harmonics that reach the MCP. The same spectrum is shown as a function of the photon energy in Fig. 5.8. The mapping between horizontal pixel positions and photon energies has been performed knowing that H17 ($E = 26$ eV) reaches the camera at 1175 pixels, and that every harmonic is an (odd) multiple of the fundamental energy, i.e. the photon energy of the generating IR laser ($\lambda = 811$ nm, $E = 1.53$ eV).

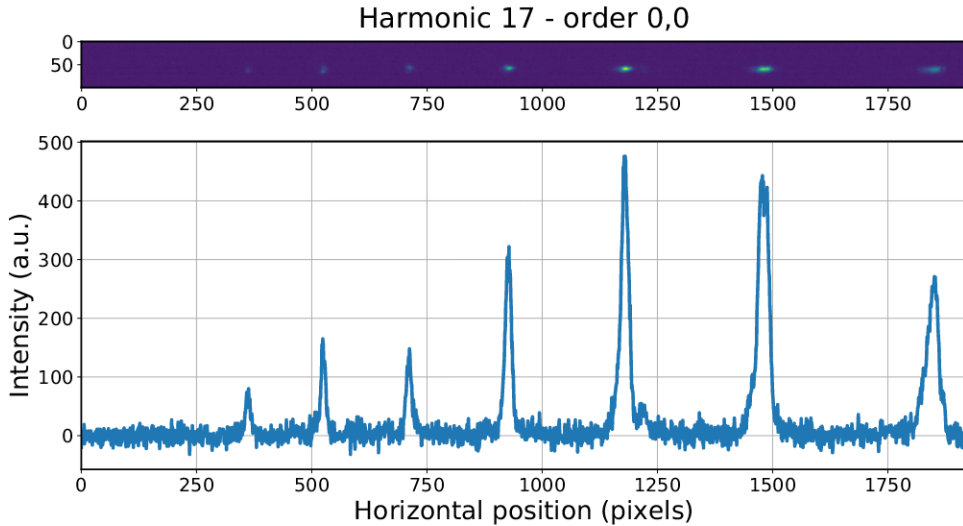


Figure 5.7: MCP image (top) and summed profile (bottom) taken on the zero-order position of both stages. The peak at 1175 pixels is harmonic 17.

In Fig. 5.9 we show the spectrum obtained by rotating the first stage to the first-order position of harmonic 17, with the second stage still at the zero-order position. In Fig. 5.10 both stages are rotated to the first-order position of harmonic 17 and in Fig. 5.11 all three spectra are plotted together.

The same measurements have been carried out for harmonic 23, as shown in Fig. 5.12, 5.13 and 5.14. As can be noticed, at this photon energy there is a significant gain in intensity between the zero-order position and the first-order position, demonstrating that the gratings are *blazed*, i.e. they show a higher efficiency at the first diffracted order with respect to the zero-order case (reflection). The intensity gain is observed only for one harmonic (H23) while the other one (H17) is seen to decrease when moving from the zero-order condition to the first-order condition. This behaviour is due to the fact that the blaze condition is highly energy-dependent. In fact, diffraction grating manufacturers specify not only the blaze angle of their gratings but also the *blaze wavelength* (see Sec. 7 in the Ap-

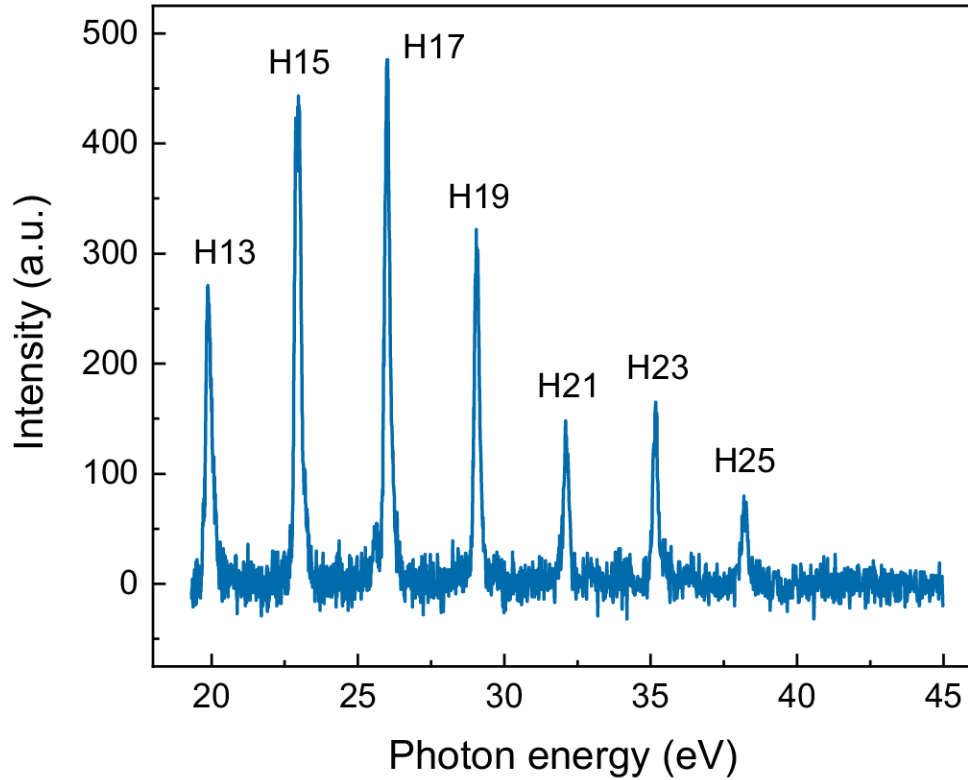


Figure 5.8: Spectral profile taken on the zero-order position of both stages, as a function of photon energy. The spectrum is mirrored compared to Fig. 5.7 because higher harmonics (short wavelengths) reach the left part of the sensor (low pixel values), and vice versa.

pendix for more details). The gratings employed in the time-delay compensated monochromator are blazed for harmonic 23, which corresponds to a wavelength $\lambda = 35.2$ nm.

In the intensity profiles of H23 it is clearly observed that two harmonic lines are actually reaching the spectrometer (at 360 and 530 pixels) instead of only one. This is because the intermediate slit was deliberately left open for convenience. During the normal operation of the instrument the slit is closed just enough to let only one harmonic pass through and reach the experimental chamber.

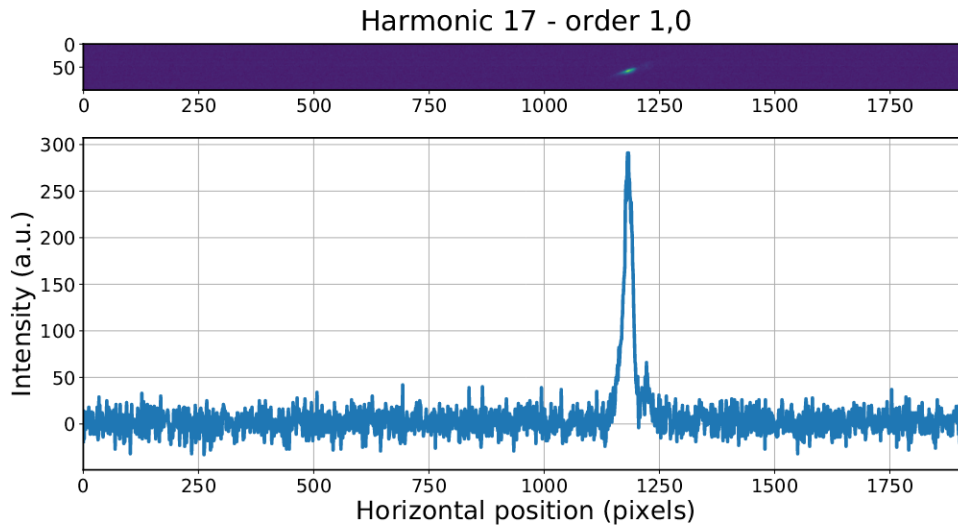


Figure 5.9: MCP image (top) and summed profile (bottom) taken with stage 1 at the first-order position and stage 2 at zero-order position. The peak at 1175 pixels is harmonic 17 ($E = 26$ eV).

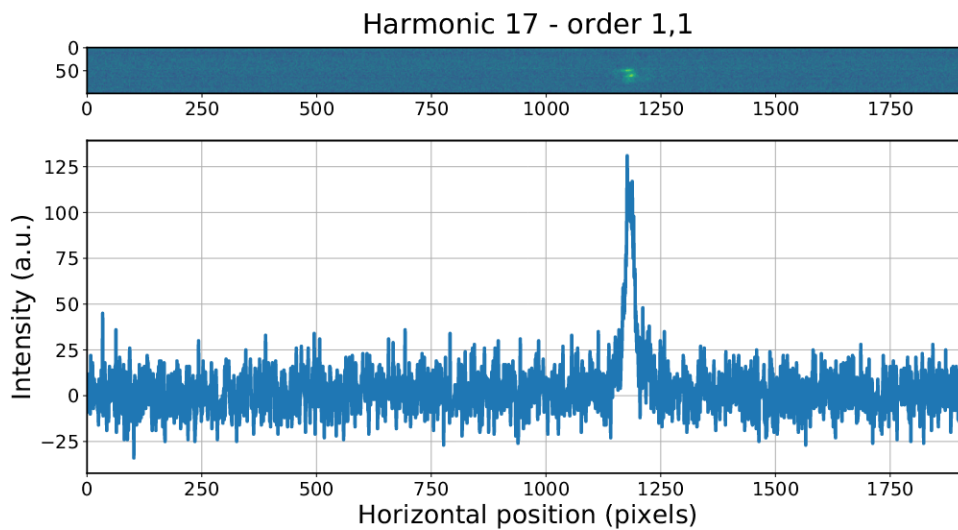


Figure 5.10: MCP image (top) and summed profile (bottom) taken on the first-order position of both stages. The peak at 1175 pixels is harmonic 17 ($E = 26$ eV).

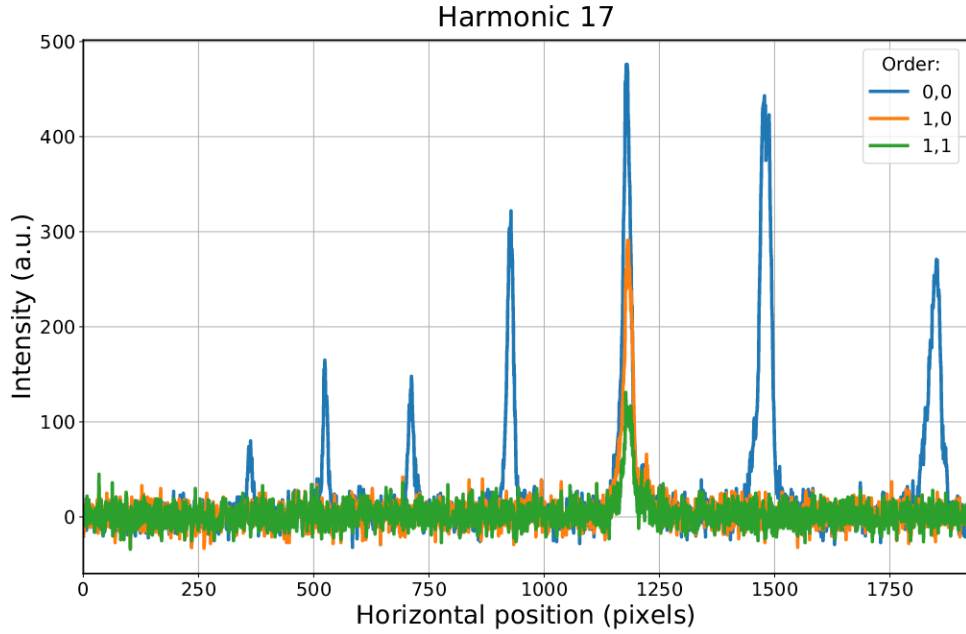


Figure 5.11: Spectral profiles taken in three different configurations. The peak at 1175 pixels is harmonic 17 ($E = 26$ eV). The intensity of H17 decreases when moving from 0,0 to 1,1 condition because the gratings are not blazed for this specific wavelength.

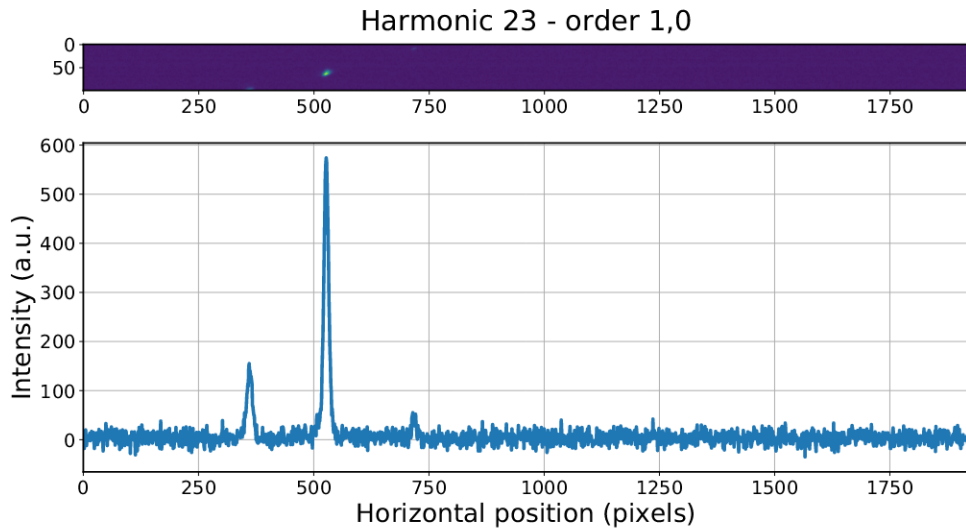


Figure 5.12: MCP image (top) and summed profile (bottom) taken with stage 1 at the first-order position and stage 2 at zero-order position. The peak at 530 pixels is harmonic 23 ($E = 35.2$ eV).

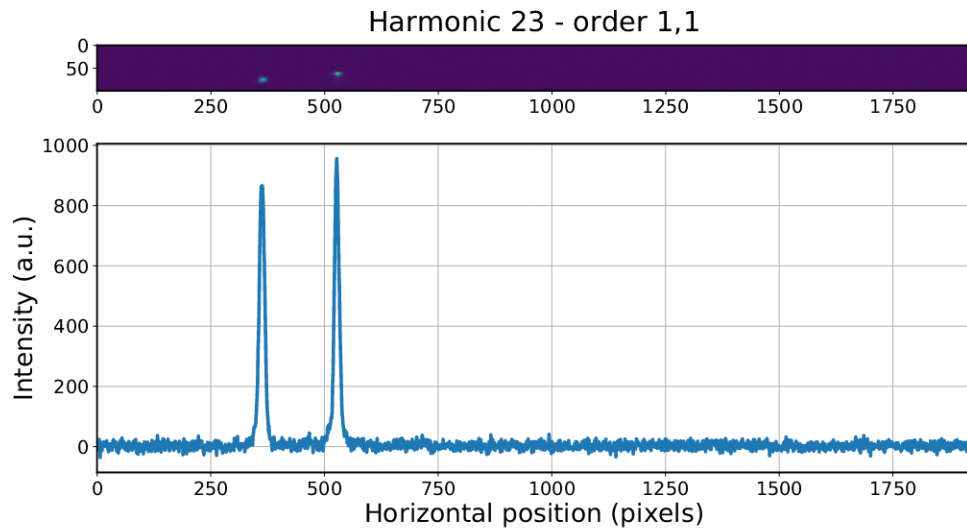


Figure 5.13: MCP image (top) and summed profile (bottom) taken on the first-order position of both stages. The peak at 530 pixels is harmonic 23 ($E = 35.2$ eV).

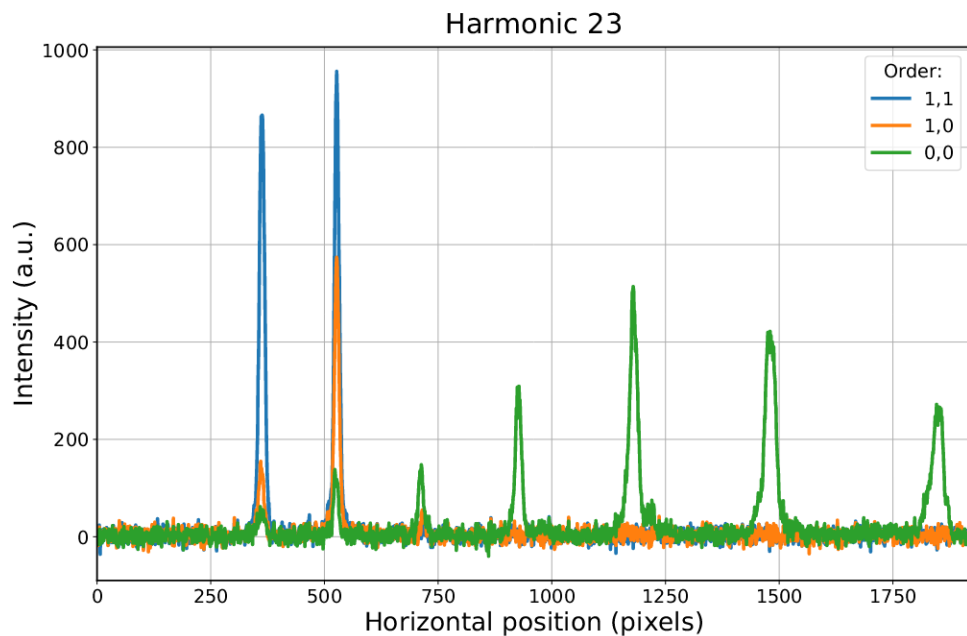


Figure 5.14: Spectral profiles taken in three different configurations. The peak at 530 pixels is harmonic 23 ($E = 35.2$ eV).

5.6 Temporal characterization

After the efficiency characterization we proceeded with the temporal characterization of the ultrashort XUV pulses, in order to evaluate the effectiveness of the time-delay compensation of the monochromator.

The temporal characterization has been achieved by a cross-correlation measurement of the XUV pulse with a synchronized infrared (IR) pulse. The laser pulses (20 fs duration, 811 nm central wavelength, and 1 kHz repetition rate) are split in two parts using a drilled mirror with a 5 mm diameter central hole. The inner part is focused by using a 250 mm focal length mirror into a 3.5 mm thick argon cell with static pressure for HHG. The XUV radiation propagates inside the TDCM, which performs the spectral selection of single harmonics by the intermediate slit. An argon jet is located in the output focal point of the monochromator, as shown in Fig. 5.15. The outer annular part of the IR beam is focused onto the same argon jet, for the cross-correlation measurement. The XUV and IR beams are directed onto the argon jet by using a collinear geometry. The delay between the two pulses is controlled by a piezoelectric translator with a resolution of 10 nm. The photoelectrons generated by single-photon absorption of the XUV pulses are collected by a time-of-flight (TOF) spectrometer, within an acceptance angle of $\pm 2^\circ$ around $\theta = 0^\circ$, where θ is the angle between the TOF axis and the common polarization directions of the IR and XUV fields.

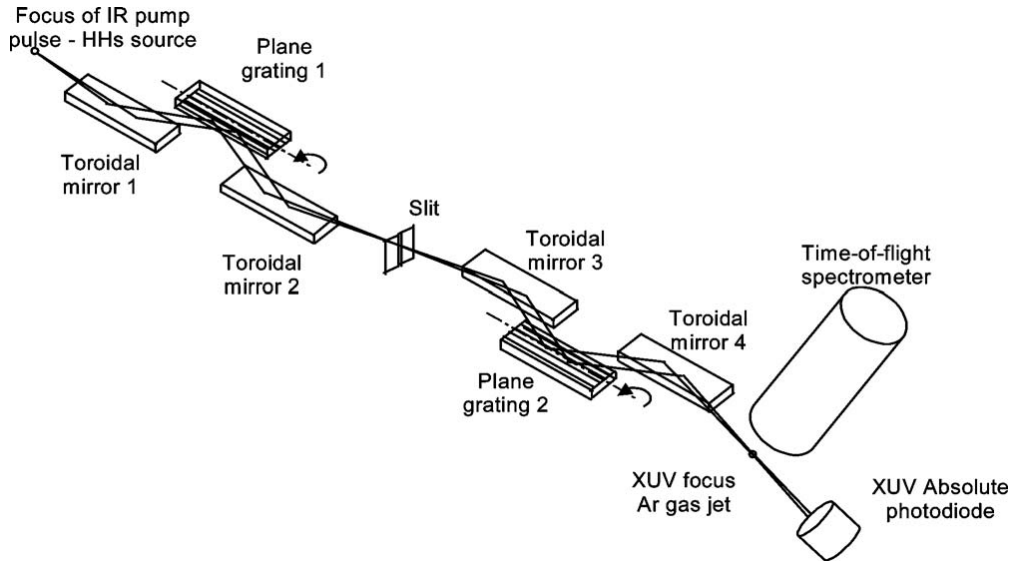


Figure 5.15: Optical setup of the time-delay-compensated monochromator showing the time-of-flight spectrometer at the output of the monochromator.

The harmonic XUV pulse ionizes the gas (argon) in the presence of the IR field. When the two pulses overlap in time and space on a gas jet, sidebands appear in the photoelectron spectrum, spectrally shifted by the IR photon energy, determined by the absorption of one harmonic photon plus the absorption or the emission of one IR photon. The sideband amplitude as a function of the delay, τ , between the XUV and IR pulses provides the cross-correlation signal. In Fig. 5.16 the spectrogram (electron energy vs. delay trace) obtained ionizing Ar with the 23rd harmonic ($E = 35.2$ eV) while perturbing with a delayed IR pulse is shown.

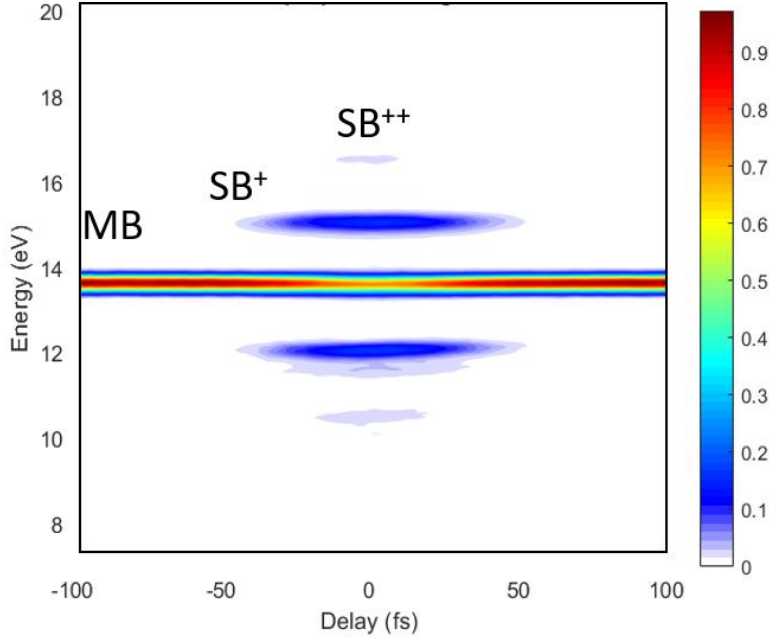


Figure 5.16: Spectrogram obtained by ionizing Ar with H23.

A typical single harmonic spectrogram (SHS) shows a mainband (MB) at 13.7 eV, corresponding to the direct XUV ionization, as given by

$$E_{\text{MB}} = E_{\text{XUV}} - E_{\text{binding}} = 23 E_{\text{IR}} - E_{\text{binding}} = 23 \times 1.53 - 21.5 = 13.7 \text{ eV},$$

where E_{MB} is the kinetic energy of the electrons as measured by the TOF, E_{XUV} is the energy of the XUV photons being used, E_{binding} is the binding energy of the electron measured relative to the chemical potential, and E_{IR} is the energy of the IR photons.

At around zero delay, i.e. when the XUV and IR pulses are spatially and temporally overlapped, sidebands (SB) appear in the spectrogram at energies

$$E_{\text{SB}^m} = E_{\text{MB}} \pm m E_{\text{IR}}$$

with m a positive integer number.

By integrating the first sideband (SB^+) in energy one obtains the sideband amplitude as a function of the delay, as shown in Fig. 5.17.

The duration of the spectrally selected harmonic pulses is retrieved by measuring the duration of the obtained sideband amplitude profile and by knowing the duration of the IR pulse. The measurement principle is described in detail in [64, 65]. As a first approximation, assuming gaussian temporal profiles for both pulses, the duration of the XUV pulse can be retrieved from

$$T_{\text{SB}}^2 = T_{\text{IR}}^2 + T_{\text{XUV}}^2 \quad (5.1)$$

where T_{SB} is the duration (FWHM) of the sideband amplitude, T_{IR} is the duration of the IR pulse, and T_{XUV} is the duration of the XUV pulse.

The duration (19.1 fs) of the IR pulses has been independently measured with a second-harmonic generation (SHG) FROG (Frequency Resolved Optical Gating) technique, a widely used method for measuring the spectral phase of ultrashort laser pulses [66].

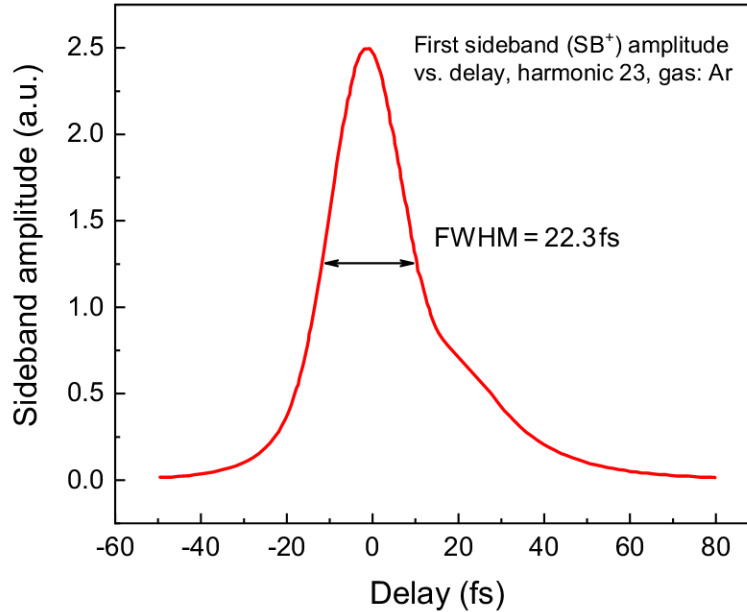


Figure 5.17: Amplitude vs. delay of the first sideband (SB^+) of H23.

The measured duration of the sideband amplitude is 22.3 fs and this gives us a XUV pulse duration of 11.5 fs, which turns out to be in good agreement with numerical simulations based on the non-adiabatic saddle-point method [67], which show that for plateau harmonics (as the 23rd harmonic) $T_{\text{XUV}} \approx T_0/2$, where T_0 is the duration of the generating pulse, while the XUV duration decreases in the cutoff region of the harmonic spectrum. The experimental results clearly demonstrate that spectral selection of the XUV pulses obtained by using the TDCM has been achieved preserving the harmonic pulse duration.

5.7 Conclusions

In this chapter the work carried out for the upgrade of a time-delay compensated monochromator has been presented. The instrument is employed in a HHG beamline in Milan and it is used for the spectral selection of ultrashort high-order laser harmonics in the extreme-ultraviolet region. It adopts two diffraction gratings in the time-delay compensated configuration, in order to compensate for the pulse-front tilt introduced by a single grating and thus to preserve the ultrashort duration of the XUV pulses.

Different improvements have been adopted:

- Interchangeable gratings on both sections, for the low- and high-energy spectral range;
- Independent regulation of the gratings' roll in order to allow a fine optimization of the XUV spot shape;
- Motorized (remoted) control of all the rotational degrees of freedom of the last toroidal mirror;

- Beam-stabilization system with a He-Ne laser beam running parallel to the XUV beam;
- Development of a dedicated software for the complete control of the instrument.

After the upgrade, an efficiency characterization has been carried out. High-order harmonics have been generated in argon and the resulting spectra were observed on a grating spectrometer in different working conditions of the monochromator. Harmonic H23 ($E = 35.2$ eV) shows a significant gain in intensity between the zero-order configuration (both gratings acting like mirrors) and the first-order condition (both gratings set to the first-order position), demonstrating the effectiveness of the off-plane mount with blazed diffraction gratings.

Finally, the instrument has been temporally characterized. By measuring the cross-correlation of the XUV pulses with a synchronized portion of the generating IR pulse, the temporal duration of the XUV pulses has been derived. Pulses as short as 11 fs have been measured at the output of the monochromator, demonstrating that the developed monochromator allows one to preserve the ultrashort XUV pulse duration after spectral filtering.

Chapter 6

Conclusions

In this chapter the main results achieved in the three areas covered in this thesis are summarized.

Design and development of a reflection polarimeter

In Chapter 3 I presented the work carried out for the design and the development of a reflection polarimeter to be used in the XUV spectral region. The working principle of the proposed system is based on the polarization change that incoming radiation undergoes after reflection off a metallic surface. By employing 3 consecutive reflections the polarizing effect is enhanced and, at the same time, the output beam is made collinear with the optical axis, leaving the overall direction unaltered.

The polarimeter was used to successfully align the double slits of the beamline with respect to the wiggler source, as measurements had shown that, when using the grazing incidence monochromator, the beamline was dominated by the bending emission instead of the radiation produced by the wiggler. This problem was the cause for the low degree of linear polarization and the difficulties we had encountered during the alignment process of the mirror-stage. The polarimeter stage has been an incredibly useful tool to analyze the polarization state of the radiation entering the experimental chamber, demonstrating its effectiveness as a diagnostic instrument for XUV beamlines where a fast and reliable measure of the polarization is required.

The polarimeter system was used to efficiently characterize the state of polarization of the CiPo beamline, across a wide range of photon energies, from 10 eV to 100 eV. We used mirrors coated in gold and ruthenium, which have a well-known behaviour in the XUV spectral range and whose refractive indexes are readily available in literature. By fixing the ellipsometric parameter ψ , a fitting process was performed on the acquired intensity curves in order to retrieve the Stokes parameters of the beamline's radiation. The degree of linear (horizontal) polarization is greater than 90% across the whole measured spectral range.

The proposed polarimeter stage was also used to measure the polarimetric response of thin films, in particular graphene (both mono-layer and three-layer) and silicon dioxide. These measurements constitute a sort of ellipsometric experiment and they are of great interest because they enable the study of the optical properties of thin films in the XUV spectral range. The acquired polarimetric curves indicate that the proposed polarimeter is able to effectively measure and discrim-

inate between the different samples, even in the case of mono-atomic layers like the 1-layer-graphene. Furthermore, we showed that by employing a *normalization* procedure of the ellipsometric parameter ψ , with respect to a reference sample (SiO₂ in our case), we are able to isolate the polarimetric response of the sample under investigation from the response of the other mirrors and from the knowledge of the polarization state of the light being used during the experiment. What is obtained is specific information about the sample, without the influence of the other two mirrors and the polarization state of the used light. This property is extremely useful because it enables ellipsometric experiments even in the case of the 2 outer mirrors presenting some optical damage. Future work should be devoted to the development of appropriate fitting models for the polarimetric responses of the analyzed materials, in order to retrieve quantitative knowledge of the optical properties of the samples.

An interesting topic for future work is the development of new kind of polarimeters for single-shot acquisition, i.e. without moving parts. Such “fast” polarimeters are especially useful for pump-probe experiments, where rapid information about the rotation of the polarization is required. The configurations considered by now employ two mirrors in Kirkpatrick-Baez mount and exploit either the difference in reflectance of the two mirrors, or the generated photocurrent, in order to retrieve a quantitative knowledge of the input polarization state.

Design and development of a deformable grating system

In Chapter 4 I have presented a low-cost deformable diffraction grating that can be used to select a specific harmonic line in the XUV spectral region and, at the same time, to focus the radiation on the desired image plane.

A preliminary Finite-Element-Analysis showed that a radius of curvature of 3 m could be reached without breaking the material. Subsequently, a mechanical structure for manually bending test substrates has been realized.

Using a constant deviation-angle configuration, as typically found in monochromators and spectrometers, the system has been tested in the XUV spectral range by using a hollow-cathode lamp with He and Ne characteristic spectral lines. These measurements demonstrate the ability of the grating to bend from a plane condition down to approximately 3 m, effectively dispersing and focusing the radiation onto the image plane. The measured resolution of the instrument is particularly suitable for being employed in a monochromator for the spectral selection of high-harmonics in a HHG beamline.

A wavefront distortion measurement has been carried out in order to evaluate the performance of the bending system in obtaining a cylindrical surface. The measured wavefront slopes were fitted with the Zernike polynomials and the obtained coefficients were plotted as a function of the radius of curvature. Increasing the bending of the grating, both Astigmatism X and Defocus are seen to increase in magnitude and their ratio remains constant, indicating that the surface bends in a pure cylindrical shape. The orthogonal Zernike mode (Astigmatism Y) is very low when the substrate is plane, indicating a probable torsional effect due to the gluing process, and is observed to decrease as the bending proceeds.

Future activities and research should be devoted to the development of a time-delay compensated monochromator made of 3 optical elements instead of 6, by

employing 2 deformable diffraction gratings and 1 toroidal mirror for the focusing effect in the sagittal plane. The system will be installed as part of a HHG beamline, where harmonic selection and the compensation of the pulse-front tilt are crucial tasks for the optimal generation of ultrashort XUV pulses.

Upgrade of a time-delay compensated monochromator

In Chapter 5 the work carried out for the upgrade of a time-delay compensated monochromator has been presented. The instrument is employed in a HHG beamline in Milan and it is used for the spectral selection of ultrashort high-order laser harmonics in the extreme-ultraviolet region. It adopts two diffraction gratings in the time-delay compensated configuration, in order to compensate for the pulse-front tilt introduced by a single grating and thus to preserve the ultrashort duration of the XUV pulses.

In order to evaluate the performance of the system, an efficiency characterization has been carried out. High-order harmonics have been generated in argon and the resulting spectra were observed on a grating spectrometer in different working conditions of the monochromator. Harmonic H23 ($E = 35.2$ eV) shows a significant gain in intensity between the zero-order configuration (both gratings acting like mirrors) and the first-order condition (both gratings set to the first-order position), demonstrating the effectiveness of the off-plane mount with blazed diffraction gratings.

Finally, by measuring the cross-correlation of the XUV pulses with a synchronized portion of the generating IR pulse, the temporal duration of the XUV pulses has been derived. Pulses as short as 11 fs have been measured at the output of the monochromator, demonstrating that the developed monochromator allows one to preserve the ultrashort XUV pulse duration after spectral filtering.

Chapter 7

Publications

List of publications on international journals

- J1) S. Espinoza, F. Samparisi, F. Frassetto, S. Richter, M. Rebarz, O. Finke, M. Albrecht, M. Jurkovic, O. Hort, N. Fabris, A. Zymaková, D.D. Mai, R. Antipenkov, J. Nejd, L. Poletto, J. Andreasson “Characterization of the high harmonics source for the VUV ellipsometer at ELI Beamlines” *Journal of Vacuum Science & Technology B*, Volume 38(2), 024005 (2020), DOI: 10.1116/1.5129674;
- J2) M. Buffolo, M. Pietrobon, C. De Santi, F. Samparisi, M.L. Davenport, J.E. Bowers, G. Meneghesso, E. Zanoni and M. Meneghini “Degradation mechanisms of heterogeneous III-V/Silicon loop-mirror laser diodes for photonic integrated circuits” *Microelectronics Reliability*, Volume 88-90, Pages 855-858, September 2018. DOI: 10.1016/j.microrel.2018.06.058;
- J3) M. Buffolo, F. Samparisi, C. De Santi, D. Jung, J. Norman, J.E. Bowers, R.W. Herrick, G. Meneghesso, E. Zanoni and M. Meneghini “Physical origin of the optical degradation of InAs quantum dot lasers” *IEEE Journal of Quantum Electronics*, Volume 55, Issue 3, Article number 8684922, June 2019. DOI: 10.1109/JQE.2019.2909963;
- J4) M. Buffolo, F. Samparisi, L. Rovere, C. De Santi, D. Jung, J. Norman, J.E. Bowers, R.W. Herrick, G. Meneghesso, E. Zanoni and M. Meneghini “Investigation of current-driven degradation of 1.3 μm quantum-dot lasers epitaxially grown on silicon” *IEEE Photonics Society - Journal of Selected Topics in Quantum Electronics*, vol. 26, no. 2, pp. 1-8, March-April 2020, Art no. 8823858, DOI: 10.1109/JSTQE.2019.2939519;
- J5) F. Samparisi, F. Frassetto, P. Zuppella, L. Poletto, “Ruthenium coated mirrors for reflection polarimeters in the 40–100eV spectral region.” To be submitted to *Optics Express*, OSA;
- J6) F. Samparisi, F. Frassetto, A. Vanzo, P. Zuppella, S. Bonora, L. Poletto, “Deformable diffraction gratings for HHG beamlines.” To be submitted to *Optics Express*, OSA.

List of publications on conference proceedings

- C1) M. Buffolo, F. Samparisi, C. De Santi, D. Jung, J. Norman, J.E. Bowers, R.W. Herrick, G. Meneghesso, E. Zanoni, M. Meneghini, “Demonstration of current-dependent degradation of quantum-dot lasers grown on silicon: role of defect diffusion processes”, Proc. SPIE 11301, Novel In-Plane Semiconductor Lasers XIX, 113010L (24 February 2020), DOI: 10.1117/12.2545901;
- C2) M. Buffolo, F. Samparisi, C. De Santi, D. Jung, J. Norman, J.E. Bowers, R.W. Herrick, G. Meneghesso, E. Zanoni and M. Meneghini “Degradation mechanisms of InAs quantum dot 1.3 μm laser diodes epitaxially grown on silicon” Proceedings of SPIE - The International Society for Optical Engineering, Volume 10939, 2019, Article number 109390P; Novel In-Plane Semiconductor Lasers XVIII 2019, San Francisco, United States, February 4th 2019 to February 7th 2019. DOI: 10.1117/12.2509277;
- C3) F. Frassetto, P. Zuppella, F. Samparisi, N. Fabris, L. Poletto “Transition metal coatings for reflection polarimeters in the 50–100eV region” Proc. SPIE 11038, X-Ray Free-Electron Lasers: Advances in Source Development and Instrumentation V, 110380M, April 24th 2019; SPIE Optics + Optoelectronics 2019, Prague, Czech Republic. DOI: 10.1117/12.2522256;
- C4) N. Fabris, F. Frassetto, P. Miotti, F. Samparisi, C. Spezzani, P. Zuppella, L. Poletto, “Comparison between classical and off-plane diffraction efficiency for the soft x-ray region”, Proc. SPIE 11038, X-Ray Free-Electron Lasers: Advances in Source Development and Instrumentation V, 110380W (24 April 2019), DOI: 10.1117/12.2522609;
- C5) S. Espinoza, F. Samparisi, M. Zahradník, M. Albrecht, O. Finke, R. Antipenkov, O. Hort, M. Rebarz, M. Jurkovič, L. Poletto, J. Nejdil, and J. Andreasson, “XUV Reflection and Ellipsometry Experiments at ELIBeamlines,” in OSA High-brightness Sources and Light-driven Interactions Congress 2020 (EUVXRAY, HILAS, MICS), OSA Technical Digest (Optical Society of America, 2020), paper JW1A.23, DOI: 10.1364/EUVXRAY.2020.JW1A.23.

Appendix

Blazed gratings

Diffraction gratings can, in certain configurations, concentrate a large percentage of the energy incident on them into a specific diffraction order, while the residual power in the other orders (particularly the zeroth) is minimized. This phenomenon has come to be called *blazing*.

A grating that is in a configuration in which it is blazing is said to be in the *blaze condition*. It is important to recognize that it is the characteristics of the grating as well as the conditions under which it is illuminated that contribute to the condition known as blazing. Since this condition can only exactly be achieved for one wavelength, it is specified for which blaze wavelength the grating is optimized (or blazed).

The measure of the light intensity diffracted from a grating is called its *efficiency*. The blaze wavelength is defined as that wavelength, in a given diffraction order m , for which the efficiency curve reaches its maximum.

Like every optical grating, a blazed grating has a constant line spacing d , determining the magnitude of the wavelength splitting caused by the grating. The grating lines possess a triangular, sawtooth-shaped cross section, forming a step structure. The steps are tilted at the so-called blaze angle θ_B with respect to the grating surface. Accordingly, the angle between the step normal and the grating normal is θ_B .

The blaze angle is optimized to maximize efficiency for the wavelength of the used light. Descriptively, this means θ_B is chosen such that the beam diffracted at the grating and the beam reflected at the steps are both deflected into the same direction, as can be represented schematically in Fig. A.1.

The effect of the groove pattern of a grating on the direction of light diffracted by it is governed by the grating equation:

$$d(\sin \alpha + \sin \beta) = m\lambda \quad (\text{A.1})$$

where d is the line spacing, α is the incidence angle, β is the diffraction angle, m is the diffraction order, and λ is the wavelength of the diffracted radiation.

There is a specific geometry, called the Littrow configuration, in which the light of a specific wavelength diffracted from a grating, into a given diffraction order, travels back along the direction of the incident light: in Eq. (A.1) above this requires

$$\alpha = \beta = \theta_B$$

For the Littrow configuration, the grating equation simplifies to

$$2d \sin \theta_B = m\lambda \quad (\text{A.2})$$

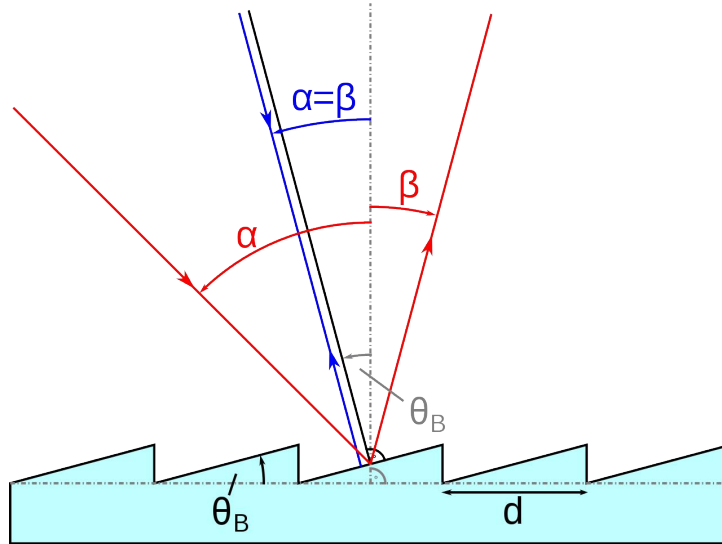


Figure A.1: Diffraction at a blazed grating. The general case is shown with red rays, the Littrow configuration is shown with blue rays.

By solving for θ_B , the blaze angle can be calculated for arbitrary combinations of diffraction order, wavelength and line spacing:

$$\theta_B = \arcsin \frac{m\lambda}{2d} \quad (\text{A.3})$$

Bibliography

- [1] D.J. Griffiths. *Introduction to Electrodynamics*. Pearson Education, 2014. ISBN: 9780321972101.
- [2] J.D. Jackson. *Classical Electrodynamics*. New York: John Wiley & Sons, 1999, p. 832.
- [3] Andrew Zangwill. *Modern electrodynamics*. Cambridge University Press, 2013.
- [4] Julius Adams Stratton. “Plane Waves in Unbounded, Isotropic Media”. In: *Electromagnetic Theory*. John Wiley & Sons, Ltd, 2015. Chap. V, pp. 268–348.
- [5] T. Koryu Ishii. *Handbook of Microwave Technology*. San Diego: Academic Press, 1995.
- [6] Mark A. Sletten and David J. Mc Laughlin. “Radar Polarimetry”. In: *Encyclopedia of RF and Microwave Engineering*. John Wiley & Sons, 2005.
- [7] S. Chandrasekhar. *Radiative transfer*. New York: Dover Publications, 1960.
- [8] Sergey N. Savenkov. “Jones and Mueller matrices: structure, symmetry relations and information content”. In: *Light Scattering Reviews 4: Single Light Scattering and Radiative Transfer*. Ed. by Alexander A. Kokhanovsky. Berlin, Heidelberg: Springer Berlin Heidelberg, 2009, pp. 71–119.
- [9] N. V. Edwards. “Status and Prospects For VUV Ellipsometry (Applied to High K and Low K Materials)”. In: *AIP Conference Proceedings* 683.1 (2003), pp. 723–737.
- [10] Shirly Espinoza et al. “Characterization of the high harmonics source for the VUV ellipsometer at ELI Beamlines”. In: *Journal of Vacuum Science & Technology B* 38.2 (2020), p. 024005.
- [11] G. Sansone et al. “Isolated single-cycle attosecond pulses”. In: *Science* 314.5798 (2006), pp. 443–446.
- [12] I.J. Sola et al. “Controlling attosecond electron dynamics by phase-stabilized polarization gating”. In: *Nature Physics* 2.5 (2006), pp. 319–322.
- [13] F. Calegari et al. “Ultrafast electron dynamics in phenylalanine initiated by attosecond pulses”. In: *Science* 346.6207 (2014), pp. 336–339.
- [14] J. Itatani et al. “Tomographic imaging of molecular orbitals”. In: *Nature* 432.7019 (2004), pp. 867–871.
- [15] A. Fleischer et al. “Spin angular momentum and tunable polarization in high-harmonic generation”. In: *Nature Photonics* 8.7 (2014), pp. 543–549.

- [16] T. Fan et al. “Bright circularly polarized soft X-ray high harmonics for X-ray magnetic circular dichroism”. In: *Proceedings of the National Academy of Sciences of the United States of America* 112.46 (2015), pp. 14206–14211.
- [17] R. Locher et al. “Versatile attosecond beamline in a two-foci configuration for simultaneous time-resolved measurements”. In: *Review of Scientific Instruments* 85.1 (2014).
- [18] D.D. Hickstein et al. “Non-collinear generation of angularly isolated circularly polarized high harmonics”. In: *Nature Photonics* 9.11 (2015), pp. 743–750.
- [19] P.C. Dubois and J. van Zyl. “Measuring Soil Moisture with Imaging Radars”. In: *IEEE Transactions on Geoscience and Remote Sensing* 33.4 (1995), pp. 915–926.
- [20] D.M. Winker, J. Pelon, and M.P. McCormick. “The CALIPSO mission: Spaceborne lidar for observation of aerosols and clouds”. In: vol. 4893. 2003, pp. 1–11.
- [21] S.R. Cloude and K.P. Papathanassiou. “Three-stage inversion process for polarimetric SAR interferometry”. In: *IEE Proceedings: Radar, Sonar and Navigation* 150.3 (2003), pp. 125–134.
- [22] E. Malus. *Mémoires de physique et de chimie de la Société d’Arcueil*. Vol. 2. Paris, 1809, pp. 143–254. This is reproduced in [25].
- [23] D. Brewster et al. *Treatise on Optics*. London, 1831.
- [24] W. Spottiswoode. *Polarisation of Light*. Nature series. London: Macmillan & Co., 1874, p. 2.
- [25] E. Mach. *The Principles of Physical Optics*. New York: Dover Publications, 1926.
- [26] W. Nicol. “On a method of so far increasing the divergency of the two rays in calcareous-spar.” In: *Edinb. New Phil. J.* 6 (1828), p. 83.
- [27] A.H. Compton and S.K. Allison. *X-rays in theory and experiment*. New York: D. Van Nostrand Company, Inc., 1935.
- [28] J.C. Slater and N.H. Frank. *Electromagnetism*. New York: McGraw-Hill, 1947.
- [29] L.D. Landau and E.M. Lifchitz. *Electrodynamics of Continuous Media*. New York: Addison-Wesley, 1960.
- [30] E.M. Gullikson. “Optical Properties of Materials”. In: *Vacuum Ultraviolet Spectroscopy*. Ed. by J.A.R. Samson and D.L. Ederer. New York: Academic Press, 1998. Chap. 13.
- [31] David Attwood. *Soft X-Rays and Extreme Ultraviolet Radiation: Principles and Applications*. Cambridge: Cambridge University Press, 1999.
- [32] L.G. Parratt. “Surface Studies of Solids by Total Reflection of X-Rays”. In: *Phys. Rev.* 95 (2 1954), pp. 359–369.
- [33] Jaeglé, P. et al. “Space-dependent shift of spectral lines in laser-produced plasmas”. In: *J. Physique Lett.* 40.21 (1979), pp. 551–554.

- [34] K. Rabinovitch, L. R. Canfield, and R. P. Madden. “A Method for Measuring Polarization in the Vacuum Ultraviolet”. In: *Appl. Opt.* 4.8 (1965), pp. 1005–1010.
- [35] T. Koide et al. “Elliptical-polarization analyses of synchrotron radiation in the 5–80-eV region with a reflection polarimeter”. In: *Nuclear Instruments and Methods in Physics Research Section A: Accelerators, Spectrometers, Detectors and Associated Equipment* 308.3 (1991), pp. 635–644.
- [36] Tsuneharu Koide, Tetsuo Shidara, and Masatada Yuri. “Polarization analyses of elliptically-polarized vacuum-ultraviolet undulator radiation”. In: *Nuclear Instruments and Methods in Physics Research Section A: Accelerators, Spectrometers, Detectors and Associated Equipment* 336.1 (1993), pp. 368–372.
- [37] Laurent Nahon and Christian Alcaraz. “SU5: a calibrated variable-polarization synchrotron radiation beam line in the vacuum-ultraviolet range”. In: *Appl. Opt.* 43.5 (2004), pp. 1024–1037.
- [38] Christian Alcaraz et al. “First polarization measurements of OPHELIE: a versatile polarization VUV undulator at Super-ACO”. In: *X-Ray Optics Design, Performance, and Applications*. Ed. by Ali M. Khounsary et al. Vol. 3773. International Society for Optics and Photonics. SPIE, 1999, pp. 250–261.
- [39] Franz Schäfers et al. “Soft-x-ray polarimeter with multilayer optics: complete analysis of the polarization state of light”. In: *Appl. Opt.* 38.19 (1999), pp. 4074–4088.
- [40] Josef Humlíček. “1 - Polarized Light and Ellipsometry”. In: *Handbook of Ellipsometry*. Ed. by Harland G. Tompkins and Eugene A. Irene. Norwich, NY: William Andrew Publishing, 2005, pp. 3–91. ISBN: 978-0-8155-1499-2.
- [41] J. Hollenshead and L. Klebanoff. “Modeling radiation-induced carbon contamination of extreme ultraviolet optics”. In: *Journal of Vacuum Science and Technology B: Microelectronics and Nanometer Structures* 24.1 (2006), pp. 64–82.
- [42] G.S. Was et al. “Resolution of the carbon contamination problem in ion irradiation experiments”. In: *Nuclear Instruments and Methods in Physics Research, Section B: Beam Interactions with Materials and Atoms* 412 (2017), pp. 58–65.
- [43] Nicolo’ Comini et al. “Factors influencing surface carbon contamination in ambient-pressure x-ray photoelectron spectroscopy experiments”. In: *Journal of Vacuum Science & Technology A* 39.4 (2021), p. 043203.
- [44] Igor S Tilinin, Aleksander Jablonski, and WSM Werner. “Quantitative surface analysis by Auger and x-ray photoelectron spectroscopy”. In: *Progress in surface science* 52.4 (1996), pp. 193–335.
- [45] J.G. Chen. “NEXAFS investigations of transition metal oxides, nitrides, carbides, sulfides and other interstitial compounds”. In: *Surface Science Reports* 30.1-3 (1997), pp. 1–152.

- [46] Jean-Jacques Ferme. “New improvements in bendable mirrors”. In: *Materials, Manufacturing, and Measurement for Synchrotron Radiation Mirrors*. Ed. by Peter Z. Takacs and Thomas W. Tonnessen. Vol. 3152. International Society for Optics and Photonics. SPIE, 1997, pp. 103–111.
- [47] C. Truesdell. “Timoshenko’s History of Strength of Materials (1953)”. In: *An Idiot’s Fugitive Essays on Science: Methods, Criticism, Training, Circumstances*. New York, NY: Springer New York, 1984, pp. 251–253.
- [48] A.C. Ugural and S.K. Fenster. *Advanced Strength and Applied Elasticity*. Prentice Hall PTR, 2003. ISBN: 9780130473929.
- [49] Maurizio Sacchi et al. “Ultrahigh-vacuum soft x-ray reflectometer”. In: *Review of Scientific Instruments* 74.5 (2003), pp. 2791–2795.
- [50] Nicola Fabris et al. “Comparison between classical and off-plane diffraction efficiency for the soft x-ray region”. In: *X-Ray Free-Electron Lasers: Advances in Source Development and Instrumentation V*. Vol. 11038. SPIE, Apr. 24, 2019.
- [51] James C. Wyant and Katherine Creath. “Basic Wavefront Aberration Theory for Optical Metrology”. In: *Applied Optics and Optical Engineering, Volume XI*. Ed. by Robert R. Shannon and James C. Wyant. Vol. 11. Jan. 1992, p. 2.
- [52] G. H. C. New and J. F. Ward. “Optical Third-Harmonic Generation in Gases”. In: *Phys. Rev. Lett.* 19 (10 1967), pp. 556–559.
- [53] C. Pellegrini. “The history of X-ray free-electron lasers”. In: *The European Physical Journal H* 37 (5 2012), pp. 659–708.
- [54] P. M. Paul et al. “Observation of a Train of Attosecond Pulses from High Harmonic Generation”. In: *Science* 292.5522 (2001), pp. 1689–1692.
- [55] M Hentschel et al. “Attosecond metrology”. In: *Nature* 414.6863 (2001), pp. 509–513.
- [56] Tenio Popmintchev et al. “Bright Coherent Ultrahigh Harmonics in the keV X-ray Regime from Mid-Infrared Femtosecond Lasers”. In: *Science* 336.6086 (2012), pp. 1287–1291.
- [57] P. B. Corkum. “Plasma perspective on strong field multiphoton ionization”. In: *Phys. Rev. Lett.* 71 (13 1993), pp. 1994–1997.
- [58] K. J. Schafer et al. “Above threshold ionization beyond the high harmonic cutoff”. In: *Phys. Rev. Lett.* 70 (11 1993), pp. 1599–1602.
- [59] M. Lewenstein et al. “Theory of high-harmonic generation by low-frequency laser fields”. In: *Phys. Rev. A* 49 (3 1994), pp. 2117–2132.
- [60] G. Farkas and C. Toth. “Proposal for attosecond light pulse generation using laser induced multiple-harmonic conversion processes in rare gases”. In: *Physics Letters A* 168.5 (1992), pp. 447–450.
- [61] G. Lambert et al. “Injection of harmonics generated in gas in a free-electron laser providing intense and coherent extreme-ultraviolet light”. In: *Nature Physics* 4 (4 2008), pp. 296–300.

- [62] D. Gauthier et al. “Single-shot Femtosecond X-Ray Holography Using Extended References”. In: *Phys. Rev. Lett.* 105 (9 2010), p. 093901.
- [63] Masatoshi Hatayama et al. “Wide-range narrowband multilayer mirror for selecting a single-order harmonic in the photon energy range of 40–70 eV”. In: *Opt. Express* 24.13 (2016), pp. 14546–14551.
- [64] T. E. Glover et al. “Observation of Laser Assisted Photoelectric Effect and Femtosecond High Order Harmonic Radiation”. In: *Phys. Rev. Lett.* 76 (14 Apr. 1996), pp. 2468–2471.
- [65] E. S. Toma et al. “Ponderomotive streaking of the ionization potential as a method for measuring pulse durations in the XUV domain with fs resolution”. In: *Phys. Rev. A* 62 (6 Oct. 2000), p. 061801.
- [66] Rick Trebino et al. “Measuring ultrashort laser pulses in the time-frequency domain using frequency-resolved optical gating”. In: *Review of Scientific Instruments* 68.9 (1997), pp. 3277–3295.
- [67] G. Sansone et al. “Nonadiabatic quantum path analysis of high-order harmonic generation: Role of the carrier-envelope phase on short and long paths”. In: *Phys. Rev. A* 70 (1 July 2004), p. 013411.